Quantum simulation of electron transport in disordered two-dimensional transition metal dichalcogenides

Jejune Park

Université Grenoble Alpes

THÈSE

Pour obtenir le grade de

DOCTEUR DE L'UNIVERSITÉ GRENOBLE ALPES

Spécialité : NANO ELECTRONIQUE ET NANO TECHNOLOGIES

Arrêté ministériel : 25 mai 2016

Présentée par

JEJUNE PARK

Thèse dirigée par **Mireille MOUIS**, Directeur de Recherche
et codirigée par **François TRIOZON**, Ingénieur-Chercheur, Université Grenoble Alpes
et **Alessandro CRESTI**

préparée au sein du **Laboratoire Institut de Microélectronique, Electromagnétisme et Photonique - Laboratoire d'hyperfréquences et de caractérisation**
dans **l'École Doctorale Electronique, Electrotechnique, Automatique, Traitement du Signal (EEATS)**

Simulation quantique du transport électronique dans les dichalcogénures de métaux de transition bidimensionnels désordonnés

Quantum simulation of electron transport in disordered two-dimensional transition metal dichalcogenides

Thèse soutenue publiquement le **19 juin 2020**,
devant le jury composé de :

Madame Mireille MOUIS
DR, CNRS, IMEP-LaHC, Directeur de thèse
Monsieur Philippe DOLLFUS
Directeur de recherche, CNRS, Centre de Nanosciences et de Nanotechnologies - C2N, Rapporteur
Monsieur Stephan ROCHE
Professeur, Catalan Institute of Nanoscience and Nanotechnology (ICN2), Rapporteur
Madame Laurence MAGAUD
Directeur de recherche, CNRS, Institut Néel, Présidente
Monsieur Jean-Christophe CHARLIER
Professeur, Université catholique de Louvain (UC Louvain), Examinateur
Madame Blanca BIEL
Professeur associé, Universidad de Granada, Examinateur

Abstract

The discovery of graphene in 2004 has inspired a great interest in two-dimensional (2D) materials. In recent years, semiconducting 2D materials, in particular, are in the limelight for their potential use in electronics and optoelectronics. From the perspective of metal-oxide-semiconductor field-effect transistors, their atomic thickness allows an enhanced electrostatic control and their self-passivated surface reduces the potential presence of charge traps. Most importantly, the presence of a bandgap, contrary to graphene, facilitates a high on/off ratio in logic devices. Among these semiconducting materials, transition metal dichalcogenides (TMDs), with their large variety of band alignments and bandgaps, have attracted great attention for their possible use in transistors, both as monolayer materials or combined in van der Waals heterostructures. For such applications, the TMD quality is a priority, since the presence of defects might significantly affect electron transport thus leading to performance degradation.

The present thesis reports on the impact of various defects, which are often observed in experimental samples, on the transport properties of TMDs. The study is based on quantum transport simulations, which combine an atomistic tight-binding description of the system and the Green's function formalism.

The first part of the thesis briefly introduces 2D materials, including their properties, synthesis, and applications. The basics of the simulation approach are also detailed. In particular, a thorough review of model Hamiltonians for TMDs, with a specific focus on tight-binding models, is presented. Moreover, the Green's function formalism, which is the methodology adopted for the quantum transport simulations performed in the present thesis, is briefly reviewed.

In the second part of the thesis, two types of typical TMD defects are simulated, and the results physically interpreted. The first study concerns edge roughness in MoS_2 ribbons, which play an important role in the miniaturization of TMD-based transistors. The second study focuses on twin grain boundaries, which are often present in polycrystalline MoS_2 obtained by large-scaling synthesis approaches, as chemical vapor deposition or molecular beam epitaxy. The role of spin-orbit coupling, which is significantly large in TMDs, is also taken into account. The results of these studies are quantitatively analyzed in terms of quasi-ballistic, diffusive, and localized transport regimes.

The main outcome of this thesis is a better understanding and prediction of the impact of defects on the transport properties of TMDs, with possible applications in the design of performant TMD-based devices.

Résumé

La découverte du graphène en 2004 a suscité un grand intérêt pour les matériaux bidimensionnels (2D). En particulier, ces dernières années, les matériaux 2D semi-conducteurs sont à l'honneur pour leur utilisation potentielle en électronique et optoélectronique. Du point de vue des transistors à effet de champ, leur épaisseur atomique permet un contrôle électrostatique amélioré et leur surface auto-passivée réduit le risque potentiel de pièges de charge. De façon plus importante encore, contrairement au graphène qui est semi-métallique, la présence de la bande interdite dans les dichalcogénures de métaux de transition (TMDs) permet un rapport entre courants à l'état passant et à l'état bloqué élevé dans les dispositifs logiques. Parmi ces matériaux semi-conducteurs, les TMDs, avec leur grande variété de bandes interdites et d'alignements de bandes, ont attiré une attention particulière pour leur possible utilisation dans les transistors, à la fois comme matériaux monocouches ou combinés dans des hétérostructures van der Waals. Pour de telles applications, la qualité des TMDs est une priorité, car la présence de défauts peut affecter de manière significative le transport d'électrons, conduisant ainsi à une dégradation des performances.

La présente thèse rend compte de l'impact de divers défauts, qui sont souvent observés dans des échantillons expérimentaux, sur les propriétés de transport des TMDs. L'étude est basée sur des simulations de transport quantique, qui combinent une description atomistique de type liaisons fortes du système et le formalisme de la fonction de Green.

La première partie de la thèse présente brièvement les matériaux 2D, y compris leurs propriétés, leur synthèse et leurs applications. Les bases de la méthode de simulation sont également détaillées. En particulier, une revue exhaustive des modèles hamiltoniens pour les TMDs, avec un accent particulier sur les méthodes des liaisons fortes, est présentée. De plus, le formalisme de la fonction de Green, qui est la méthodologie adoptée pour les simulations de transport quantique effectuées dans la présente thèse, est brièvement passé en revue.

Dans la deuxième partie de la thèse, deux types de défauts typiques des TMDs sont simulés et les résultats physiquement interprétés. La première étude concerne la rugosité des bords des rubans MoS_2, qui jouent un rôle important dans la miniaturisation des transistors à base de TMDs. La deuxième étude se concentre sur les joints de grains de type mirror-twin, qui sont souvent présents dans le MoS_2 polycristallin obtenu par des approches de synthèse à grande échelle, comme le dépôt chimique en phase vapeur ou l'épitaxie par faisceau moléculaire. Le rôle du couplage spin-orbite, qui est important dans les TMDs, est également pris en compte. Les résultats de ces études sont analysés quantitativement en termes de régimes de transport quasi balistique, diffusif et localisé.

Les principaux résultats de cette thèse sont une meilleure compréhension et prédiction de l'impact des défauts sur les propriétés de transport des TMDs, avec une application possible dans la conception de dispositifs performants basés sur les TMDs.

Contents

Contents i

Acronyms 1

1 Introduction to transition metal dichalcogenides and goals of the PhD 3
- 1.1 History of 2D materials . . . 3
- 1.2 General properties of TMDs . . . 4
  - 1.2.1 Structural properties . . . 4
  - 1.2.2 Electronic and transport properties . . . 6
- 1.3 Synthesis of TMDs . . . 8
  - 1.3.1 Mechanical and chemical exfoliation . . . 9
  - 1.3.2 Chemical vapor deposition . . . 9
  - 1.3.3 Molecular beam epitaxy . . . 10
- 1.4 Disorders in TMDs . . . 10
  - 1.4.1 Point defects . . . 11
  - 1.4.2 Line defects and grain boundaries . . . 13
  - 1.4.3 Edges and edge roughness . . . 14
- 1.5 Possible applications of TMDs in nanoelectronics . . . 15
  - 1.5.1 Electronics . . . 16
  - 1.5.2 Optoelectronics . . . 17
- 1.6 Goal and structure of the thesis . . . 18

2 Model Hamiltonian for 2D TMDs 21
- 2.1 TB model . . . 21
  - 2.1.1 Brief introduction . . . 22
  - 2.1.2 TB model for MoS_2 . . . 26
  - 2.1.3 Spin-orbit coupling . . . 30
- 2.2 k·p theory . . . 32
  - 2.2.1 A brief introduction . . . 33
  - 2.2.2 k· p model for TMDs . . . 34
- 2.3 DFT based Hamiltonian . . . 37
- 2.4 Summary . . . 39

3 Quantum transport model 41

3.1 Basics of the second quantization formalism 41
3.1.1 Second quantization 41
3.1.2 Fock space and creation/annihilation operators 43
3.1.3 More about creation/annihilation and field operators . 44
3.1.4 Operators in the second quantization formalism 44
3.2 Green's function formalism 46
3.2.1 Particle density and current operators 46
3.2.2 Schrödinger and Heisenberg pictures 47
3.2.3 Definition of Green's functions 49
3.2.4 Numerical evaluation of Green's functions 51
3.2.5 Formulas for the density of states and the charge current 59
3.3 Transport regimes 62
3.4 Summary 65

4 Structure and implementation of the numerical code 67
4.1 General structure of the codes 67
4.2 Implementation of TB Hamiltonians 69

5 Transport in rough MoS_2 ribbons 71
5.1 Simulation model 72
5.1.1 Model of edge roughness 72
5.1.2 Model structure 73
5.2 Results and discussion 74
5.2.1 Electronic properties 75
5.2.2 Localized transport regime of edge states 76
5.2.3 Diffusive transport regime of bulk states 77
5.2.4 Scaling of mean free path 78
5.2.5 Different behavior of zigzag and armchair ribbons . . . 80
5.2.6 Effect of spin-orbit coupling 82
5.3 Summary 84

6 Transport along and across disordered mirror twin grain boundaries in MoS_2 85
6.1 Simulation model 86
6.1.1 Calibration of the TB model 87
6.1.2 Model structure 91
6.2 Results and discussion 92
6.2.1 Electronic properties of MTBs 93
6.2.2 Transport along MTBs 95
6.2.3 Transport across MTBs 103
6.3 Summary 106

7 Conclusions and perspectives 109

Bibliography 113

List of publications and conferences **133**

Acknowledgements **135**

Acronyms

1D one-dimensional

2D two-dimensional

a-MoS_2 armchair MoS_2 ribbon

BZ Brillouin zone

CB conduction band

CVD chemical vapor deposition

DFT density functional theory

EQE extrinsic quantum efficiency

FET field-effect transistor

LDoS local density of states

MBE molecular beam epitaxy

MLWF maximally localized Wannier function

MTB mirror twin grain boundary

NN nearest-neighbor

PECVD plasma-enhanced chemical vapor deposition

SK Slater-Koster

SOC spin-orbit coupling

SS subthreshold swing

STEM scanning transmission electron microscope

STS scanning tunneling spectroscopy

TB tight-binding

TMD transition metal dichalcogenide

TNN third nearest-neighbor

TW trigonal warping

VB valence band

vdW van der Waals

z-MoS_2 zigzag MoS_2 ribbon

Chapter 1

Introduction to transition metal dichalcogenides and goals of the PhD

1.1 History of 2D materials

The discovery of graphene by Geim and Novoselov [1] and its great variety of properties have opened the new era of two-dimensional (2D) materials in many research fields ranging from theoretical condensed matter physics to material science and nanoelectronic applications. Graphene has attracted tremendous interest as demonstrated by the number of studies [2], [3] to investigate and exploit its exceptional properties starting from the simple Dirac equation for massless fermions [4], passing by applications in nanoelectronics [5] and spintronics [6], [7], and up to unconventional superconductivity in magic-angle graphene superlattices [8]. Few years after its discovery, a plethora of new two-dimensional materials such as transition metal dichalcogenides (TMDs), hexagonal boron nitride, black phosphorus, silicene and germanene, have been predicted and in part successfully fabricated with a great variety of electronic properties [9]. Among them, semiconducting materials have turned out to be very promising for applications in electronics and optoelectronics [10], [11]. In the perspective of metal-oxide semiconductor field-effect transistors (FETs), 2D materials benefit from inert (self-passivated) surfaces, which reduce the incidence of traps at the interface with the oxide, and of a few-atom thinness, which permits an enhanced electrostatic control. Above all, the advantage of semiconducting 2D materials, compared to semi-metallic graphene [5], is the presence of a band gap, which allows a much higher on/off current ratio in logic FETs. The most thoroughly investigated 2D semiconducting materials beyond graphene are the TMDs [12]. They are promising for their use in nanoelectronics, especially for the realization of FETs [11], including the design of tunnel FETs with lateral [10] and vertical [13] architectures. Some years

after the first demonstration of a working MoS_2-based transistor [14], Watcher et al. [15] fabricated a complete microprocessor based on this material, thus demonstrating the true potential of TMDs for electronics.

1.2 General properties of TMDs

In this Section, I briefly summarize the general properties of TMDs. Subsection 1.2.1 introduces the structural properties of TMDs in terms of their different phases. In Subsec. 1.2.2, I outline their electronic and transport properties.

1.2.1 Structural properties

The chemical formula of TMDs is MX_2, where M is a transition metal atom (i.e. and atom with a partially filled *d* sub-shell) and X is a chalcogen atom (i.e. an element of group XVI, except oxygen, in general M=S, Se or Te). We will focus on TMDs where the transition metal belongs to group VI, and in particular X=Mo or W. A TMD monolayer consists of a layer of atoms M sandwiched between two layers of atom X, and can exist in different structural phases. Each phase corresponds to a different coordination sphere for the transition metal atoms. The most common structural phases are 2H and 1T, which are characterized by a trigonal prismatic and an octahedral coordination of the transition metal atoms, respectively. These structural phases can be

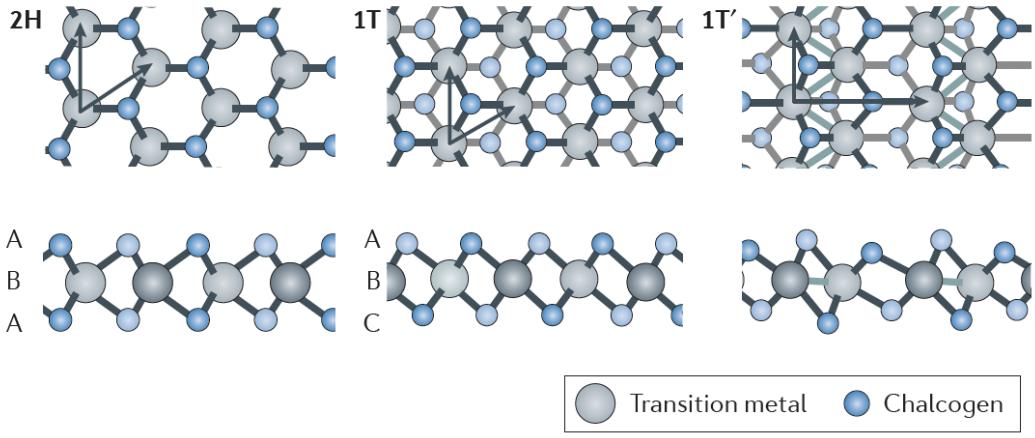

Figure 1.1: Atomic structure of single layers of TMDs in their trigonal prismatic (2H), distorted octahedral (1T) and dimerized (1T') phases. Lattice vectors and stacking of each atomic plane are indicated as arrows and in alphabetical order, respectively. Reprint from Ref. [16]. Copyright (2017) Springer Science and Business Media.

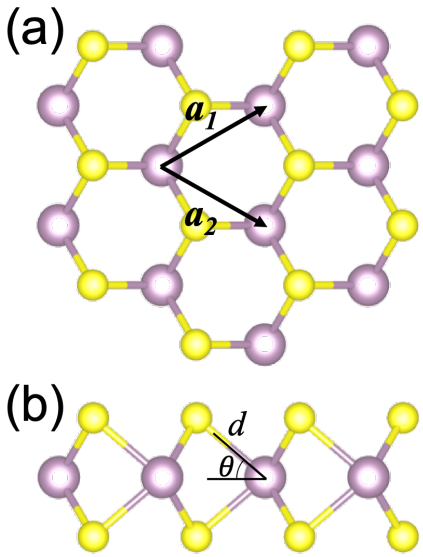

Figure 1.2: MoS_2 lattice structure. (a) Top view and (b) side view of the structure. The two primitive lattice vectors, $\boldsymbol{a_1}$ and $\boldsymbol{a_2}$, are indicated in (a). d and θ, indicated in (b), are the distance between the neighboring Mo and S atoms and the angle between the bonding of Mo-S and the Mo layer, respectively. Purple and yellow colors indicate Mo and S atoms, respectively.

classified in terms of different stacking orders of the three atomic layers. The 2H phase corresponds to an ABA stacking, and the 1T phase to an ABC stacking of the chalcogen-metal-chalcogen atomic layers, see Figure 1.1. When a distortion on the structure is induced, this could lead to the formation of metal-metal bonds and thus to the dimerization of the 1T phase, which is known as the 1T' phase. Such a weak lattice distortion embodies distinctive electronic properties, such as a topological phase [17].

Depending on the specific chalcogen and transition metal atoms, either the 2H or the 1T phase is the most stable one. The TMD electronic properties can be radically different depending on their phase. For example, the 2H phase of molybdenum disulfide (MoS_2) is semiconducting, while its 1T phase is metallic [18]–[20]. The phase transition in TMDs would thus allow the engineering of the electronic properties on the same material. In MoS_2, a phase transition can be obtained, for example, by Li and K intercalation [18], [21].

The common TMDs successfully fabricated and investigated in electronics are semiconducting TMDs from group VI in the 2H phase (in particular MoS_2, $MoSe_2$, WS_2 and WSe_2), which show sizable direct band gaps. Recently, few years after the first realization of a working MoS_2 transistor [14], transistors based on TMD van der Waals heterostructures [22], [23] were fabricated

and a complete microprocessor [15] based on these material was successfully fabricated. In this aspect, MoS_2 in the 2H phase is one of the representative semiconducting TMDs and has been widely investigated. MoS_2 shows a honeycomb structure, which consists of Mo and S atoms forming an S-Mo-S sandwich in a triangular prismatic structure, see Figure 1.2.

Monolayer MoS_2 in 2H phase has rhombic structure with the basis of two sulfur atoms (top and bottom layers) and one molybdenum atom, see Figure 1.2. The two primitive lattice vectors are defined as

$$\boldsymbol{a_1} = \Big(\frac{\sqrt{3}a}{2}, \frac{a}{2}, 0\Big) \quad \text{and} \quad \boldsymbol{a_2} = \Big(\frac{\sqrt{3}a}{2}, -\frac{a}{2}, 0\Big) \ , \tag{1.1}$$

where the lattice parameter is a=0.316 nm, as observed experimentally [24] and in agreement with density functional theory (DFT) calculations [25]–[28]. The distance between the Mo layer and the S layers placed above and below the Mo layer, see Figure 1.2(b), is 0.156 nm [29]. These parameters result in a distance between neighboring Mo and S atoms d=0.240 nm, and an angle between Mo-S bonding and the Mo plane θ=40.6° [29].

1.2.2 Electronic and transport properties

As the structure of MoS_2 is hexagonal, its Brillouin zone (BZ) is also hexagonal. From to the Bravais lattice vectors in eq. (1.1), the reciprocal lattice vectors are defined as

$$\boldsymbol{b_1} = \frac{4\pi}{\sqrt{3}a}\Big(\frac{1}{2}, \frac{\sqrt{3}}{2}, 0\Big) \quad \text{and} \quad \boldsymbol{b_2} = \frac{4\pi}{\sqrt{3}a}\Big(\frac{1}{2}, -\frac{\sqrt{3}}{2}, 0\Big) \ , \tag{1.2}$$

as indicated in Figure 1.3. The important k-points in the hexagonal BZ are the highly symmetric K/K' points (at the corner of the BZ), the M point (in the middle of the BZ edges), the Γ point (at the center of the BZ) and the Q points along the line between Γ and K or K' points. Monolayer MoS_2 has a finite

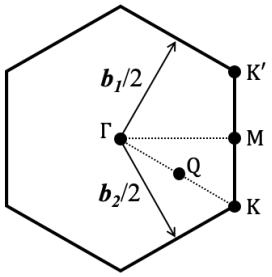

Figure 1.3: BZ of MoS_2. Γ, M, Q, K, and K' are the highly symmetric k-points, of which path indicated in dashed line is investigated for electronic properties.

and direct band gap at the K/K' points, which is promising for applications in logic electronics. A value of the band gap of about 1.9 eV is obtained by photoluminescence experiments [30], [31]. However, this value is expected to be underestimated as a consequence of significant excitonic binding energy, and indeed corresponds to the optical gap. Scanning tunneling spectroscopy (STS) found the band gap for MoS_2 of about 2.15 eV [32]. On the other hand, theoretical studies by DFT calculations with typical functionals of the local density approximation [33] and the generalized gradient approximation [34] underestimate the band gap of MoS_2 as 1.81 eV and 1.68 eV, respectively. In order to overcome this issue, more advanced techniques have been adopted to obtain the accurate band gap and dispersion. The use of the HSE06 hybrid functional gives the best agreement with the STS results [29], [35], while GW calculations show an overestimated band gap of 2.84 eV [36]. In this aspect, a model calibrated with the DFT-HSE06 band structure is the most appropriate to describe the electronic properties of MoS_2, see more details in Sec. 2.1.2.

Apart from the band gap, the electronic structure of MoS_2 shows other interesting properties at the highly symmetric k-points in BZ, see the black lines in Figure 1.4. At the K/K' points, where the direct band gap is located, the structure is electron-hole asymmetric. The band dispersion of the valence band is characterized by the trigonal warping (TW), while that of the conduction band is nearly isotropic. This effect is undoubtedly significant for understanding the behavior of the of hole carriers in MoS_2 and related phenomena, as investigated in Ref. [37] where this effect is exploited to induce a valley polarization with potential barriers. The Q points play an important role for the transport properties, since the difference between this local mini-

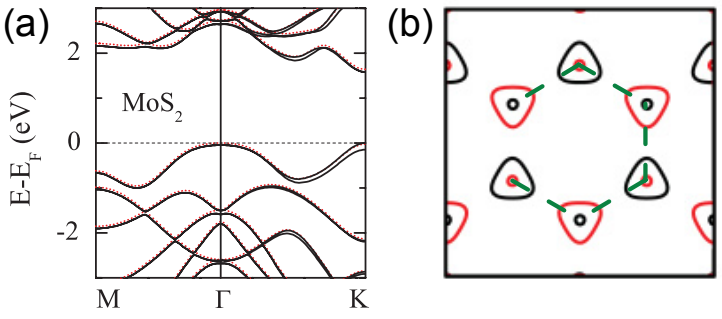

Figure 1.4: Electronic structures of monolayer MoS_2 by DFT calculations of Ref. [25]. (a) Band structure with (black line) and without (dotted red line) spin-orbit interaction. The monolayer MoS_2 has a direct band gap at K point. (b) Energy contour of spin-split hole pocket pairs for a binding energy of 0.8 eV. Electron spin orientations and BZ, which is consistent with Figure 1.3, are indicated by black and red colors, and dashed green line, respectively. Reprint from Ref. [25]. Copyright (2011) American Physical Society.

mum and the global minimum of the conduction band at Γ is only 0.3 eV [27], [29]. At the Γ point, on the other hand, the valence band is close to the top of the valence band, which is at the K/K' points. From DFT calculations, the energy difference between them turns out to be only 0.15 eV [29], and thus the electrons at the Γ point are expected to contribute to electron transport as those at the K/K' points. Note that these values of the energy differences were numerically obtained without considering the effect of spin-orbit coupling (SOC) in the model.

Indeed, SOC plays a very important role in MoS_2 and in TMDs in general. The broken spatial inversion symmetry in TMDs, see Figure 1.2, induces a strong SOC, which lifts the spin degeneracy. In particular, a large spin-splitting of about 0.2 eV occurs for the valence band at the K/K' points, see Figure 1.4(a). Note that the spin splitting at the (nonequivalent) K and K' valleys is opposite because of the time-reversal symmetry, which implies that electrons with opposite spin and at opposite k-points have the same energy, i.e. $E^{\uparrow}(\boldsymbol{k}) = E^{\downarrow}(-\boldsymbol{k})$, see Figure 1.4(b). These intriguing features open the door to new functionalities of these materials for spintronics or valleytronics [38].

Within the variety of TMDs, semiconducting TMDs have band gaps ranging from 1.2 to 2.0 eV with effective masses from 0.45 to 0.65 m_e, which are predicted by DFT calculations [39]. Moreover, the theoretically obtained carrier mobility ranges from 350 $cm^2/(Vs)$ for MoS_2 to 2500 $cm^2/(Vs)$ for $MoTe_2$ [40]. The experimental mobilities, however, are much lower due to the low quality of the materials themselves and the interface with contacts. Typically, the observed mobility is 3-160 $cm^2/(Vs)$ for MoS_2 [41], [42] and 50 $cm^2/(Vs)$ for WS_2 [43]. In this aspect, the impact of various disorders found in experiments, which are discussed in Sec. 1.4, is the main focus of the present thesis.

1.3 Synthesis of TMDs

The development of efficient synthesis techniques, particularly for large-scale production, is a primary task towards the realization of 2D material-based applications. In general, they can be classified into top-down and bottom-up approaches. The former implies that 2D materials are extracted from their bulk crystal by sizing it down, with the techniques introduced in Subsec. 1.3.1. The latter approach consists in directly growing the layers of 2D materials on a substrate. Two representative techniques, chemical vapor deposition and molecular beam epitaxy, are discussed in Subsec. 1.3.2 and Subsec. 1.3.3, respectively.

1.3.1 Mechanical and chemical exfoliation

Mechanical exfoliation, which is also well known as the "scotch-tape" method, was the very first technique to extract a few layers from bulk 2D materials, and earned Andre Geim and Konstantin Novoselov the Nobel Prize in Physics 2010 for the discovery of graphene in 2004 [1]. Thanks to the weakness of the van der Waals (vdW) coupling between the layers of 2D materials, a mechanical force can easily detach few layers or even a single layer from the bulk material. Indeed, its simplicity allows this technique to exfoliate many other materials beyond graphene [4], [44], as h-BN [45], [46] and TMDs [44], [45]. Furthermore, the quality of the exfoliated materials is usually high and depends on that of the starting materials [47]. This technique is thus useful for preparing few high-quality samples of 2D materials, mainly for laboratory investigations. However, it is not suitable for large scale production.

Another method widely used to obtain single or multi-layers from bulk materials is chemical exfoliation. After dissolving the target material in a solvent, which results in a mixture of dispersed layers, single or few-layer 2D materials can be isolated by sonication [48], [49]. The concentration of single- or few-layers products depends on the solvent used for this process [50]. Due to the slow evaporation, however, it is very challenging to fully remove the solvent from the 2D materials after exfoliation. As a consequence, the resulting quality is considerably lower than that obtained with mechanical exfoliation. This causes a huge problem for TMDs, since it may be responsible for a structural phase change, which affects their electronic properties. In this aspect, it is reported that a post-annealing process can restore the semiconducting properties of MoS_2 by changing the structural phase from 1T to 2H [51]. Compared to mechanical exfoliation, this technique is cheaper, scalable, and, in particular, has great potential for application in flexible electronics, since devices can be printed by using 2D inks [52], [53].

1.3.2 Chemical vapor deposition

One of the most widely used techniques to deposit thin films is chemical vapor deposition (CVD). This technique is very versatile, as it can provide either crystalline or amorphous films from precursors in different phases (gas, liquid, solid). Furthermore, there exist different types of CVD, such as plasma-enhanced CVD (PECVD) or cold/hot-wall CVD, which can be used for specific materials. Compared with other techniques, CVD allows us to obtain a high surface uniformity with relatively easy control of the thickness of the deposited materials [54]–[56].

Due to its extreme versatility and its ability to deposit large surfaces, CVD is the most prominently used deposition technique for large scale production of 2D materials. However, CVD TMDs may present several kinds of defects,

which are expected to significantly impact the electronic and transport properties, with possible degradation of performance of the devices based on them. One of the most common defects found in CVD TMDs is the polycrystallinity, which is inherent in the synthesis process [54], [57]. The grain boundaries at the interfaces between crystalline grains have been reported to strongly localize electrons [58], with consequent carrier mobility degradation [59], [60]. In addition, other intrinsic defects such as vacancies [56], which also result in the decrease of carrier mobility [61], have been found in CVD TMDs. Lowering their density is thus one of the most important issues in CVD growth. More details about these defects are reviewed in Sec. 1.4.

1.3.3 Molecular beam epitaxy

Molecular beam epitaxy (MBE) is another technique of the bottom-up approach performed in the ultra-high vacuum (10^{-8} to 10^{-12} Torr). It enables the precise control of the deposition of the number of layers with high quality. Using this technique, the successful growth of numerous TMDs such as $MoSe_2$ [62], WSe_2 [63], $MoTe_2$ [64], and WTe_2 [65] has been reported.

Thanks to the accurate control of the layer chemical compositions and the relatively low growth temperature, this technique turns out to be very promising for the synthesis of vdW heterostructures [64]. Indeed, the strong covalent intralayer coupling of 2D materials and weak vdW interlayer coupling allows the deposition of 2D materials one on top of the other, regardless of the extent of the lattice mismatch. Notably, vdW heterostructures of TMDs, as $MoTe_2/MoS_2$ [64], and TMDs with graphene, as $MoSe_2$/graphene [66], were successfully synthesized thus indicating that this technique allows one to effectively combine different 2D materials to obtain specific properties, such as tuned band alignments, and metallic contacts on semiconductors.

1.4 Disorders in TMDs

The quality of TMD materials is one of the most critical factors for their use in electronic devices. Despite the progress of the various synthesis techniques, as discussed in Sec. 1.3, TMDs suffer from various defects such as vacancies, polycrystallinity, and impurities. Even mechanically exfoliated TMDs, contrary to exfoliated graphene, shows defects such as, in particular, chalcogen vacancies [67]. Understanding the role of these defects in the degradation of the transport properties of TMDs is thus very important in view of their applications. In this section, several defects commonly found in experiments, as point defects, grain boundaries and edge roughness, are briefly reviewed.

1.4.1 Point defects

It has been reported that point defects inevitably form in TMDs during the synthesis process [56], [68]. On the one hand, they may degrade the transport properties, on the other hand they may provide new functionalities which are not present in the pristine case, such as local magnetic moments induced by antisites [69]. With respect to electronic and optoelectronic applications, however, lowering the density of point defects is crucial, as evident, for example, from the enhancement of photoluminescence [70] and carrier mobility [61] reported by reducing the density of sulfur vacancies in MoS_2. In this subsection, I introduce various types of point defects experimentally observed and their electronic properties.

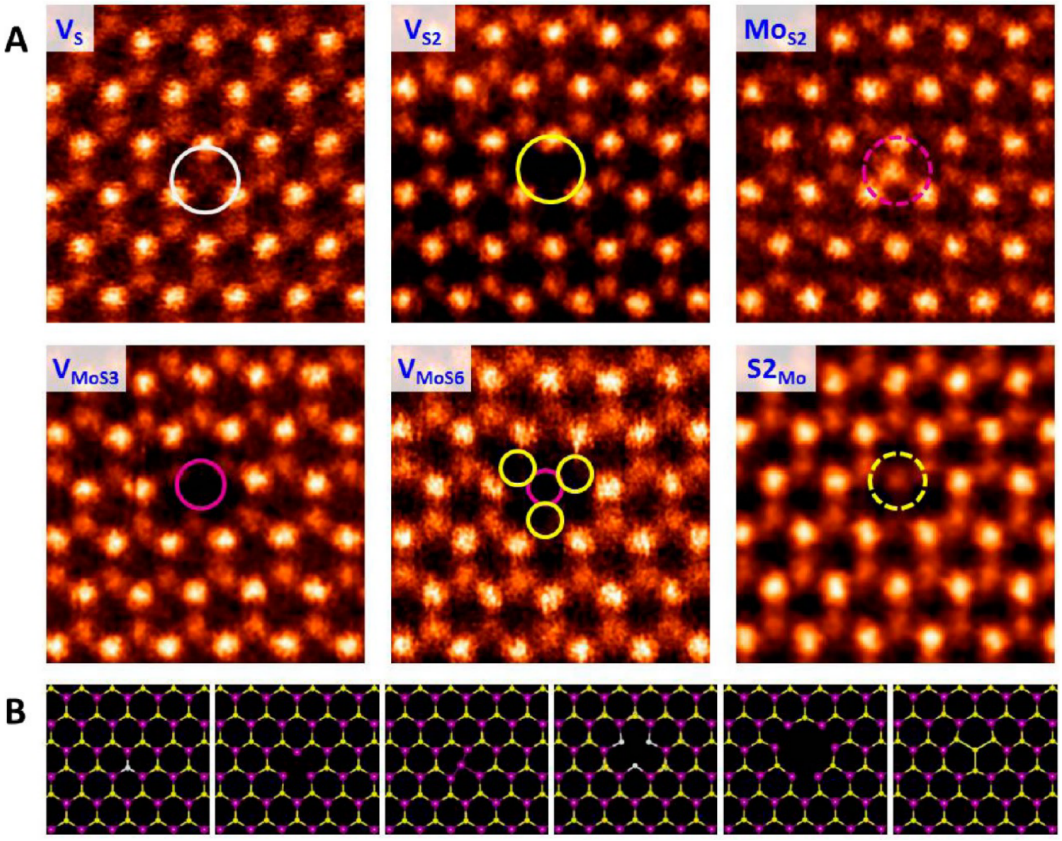

Figure 1.5: Intrinsic point defects found in CVD-grown monolayer MoS_2. (A) STEM images of various point defects: single sulfur vacancy (V_S), disulfur vacancy (V_{S2}), antisite defect of a Mo substituting a S_2 (Mo_{S2}), vacancy of Mo and nearby three sulfur atoms (V_{MoS3}), vacancy of Mo and nearby three disulfur pairs (V_{MoS6}), and antisite defect of a S_2 substituting a Mo $S2_{Mo}$. (B) Relaxed structures, calculated by DFT, of the six types of point defects in (A). Reprinted from [56]. Copyright (2013) American Chemical Society.

Figure 1.5(a) shows the scanning transmission electron microscope (STEM) images of point defects in CVD-grown monolayer MoS_2 [56]. We can observe several types of point defects, all showing a 3-fold symmetry except for the Mo_{S2} defect, which corresponds to an antisite defect of a Mo substituting a S. An important aspect to consider is the structural stability of these defects, which is related to the defect formation energies and can indicate the most probable defect among those observed in experiments. The single sulfur vacancy (V_S) turns out to have the lowest formation energy, while the other types have twice or much larger formation energies. This indicates that V_S is the most frequent and common point defect type, which is consistent with experimental observations of frequent and randomly distributed V_S [56]. For this reason, among the possible point defects, only single sulfur vacancies are considered in the present thesis.

Figure 1.6 shows the band structures of MoS_2 with a single sulfur vacancy, obtained by DFT calculations and by a minimal tight-binding (TB) model, where the orbital of the missing S atom were simply removed from the Hamiltonian. In both cases, we observe non-dispersive bands within the gap, which indicates the localized nature of the states around the V_S defect. Note that that both DFT and TB approaches produce similar results in terms of the gap states of the sulfur vacancy but at different energy levels. This suggests that the minimal TB model can reproduce, though only roughly, the impact of the sulfur vacancies on the electronic structure. We will thus use this model for the quantum transport simulations of rather large systems with randomly distributed vacancies, see Chapter 6. The DFT calculations for the study of point defects were performed by Dr. François Triozon.

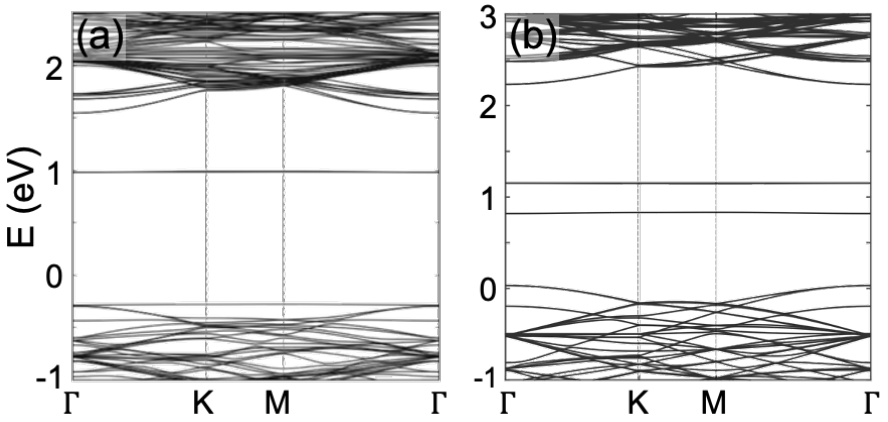

Figure 1.6: Band structures of the system of 6×6 supercell of MoS_2 with a single sulfur vacancy V_S, obtained by (a) DFT calculations and (b) a minimal TB model based on the parameterization of Ref. [29].

1.4.2 Line defects and grain boundaries

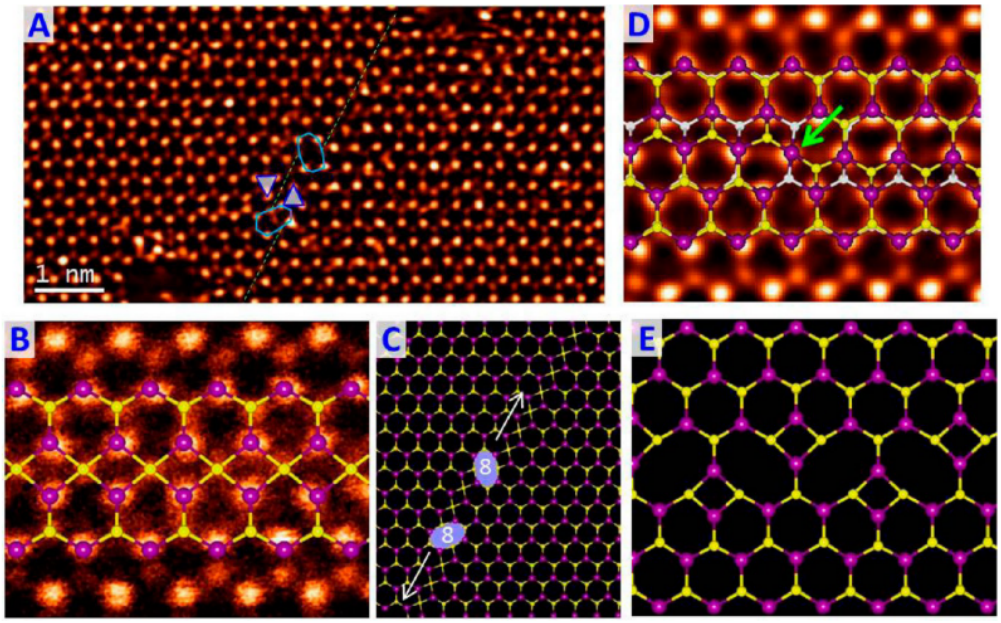

Figure 1.7: Atomic structure of MTBs in CVD-grown MoS_2. (A) STEM image of a 4|4P grain boundary. The green dash line displays the position of the 4|4P grain boundary, and the grain boundary steps are linked by octagons as indicated. The blue triangles illustrate the orientation of the two grains with 60° rotation angle. (B) STEM image of the 4|4P structures with the structural model overlaid. (C) Schematic structure of the grain boundary and kinks as shown in (A). (D) STEM image and overlaid structural model of a 4|4E type grain boundary, and the grain boundary steps are linked by 4-fold coordinated Mo atoms as highlighted. (E) Relaxed structure for 4|8 MTB, representing a 4|4P MTB with the highest kink density. Reprinted from [56]. Copyright (2013) American Chemical Society.

As discussed in Subsec. 1.3.2, CVD [54]–[56] has emerged as a very efficient growth technique for large-scale fabrication of TMDs, and it is promising for industrial production. However, CVD TMDs may present several kinds of defects, and in particular polycrystallinity, which is inherent in the synthesis process. The grain boundaries at the interfaces between crystalline grains have been reported to strongly localize electrons [58], with consequent carrier mobility degradation [59], [60]. Therefore, understanding the impact of grain boundaries on the transport properties of TMDs is of central importance.

Among the huge variety of grains boundaries with different geometries, the mirror twin grain boundaries (MTBs) are commonly observed in experiments [56], [71], [72]. An MTB is an inversion grain boundary that forms at the interface between two grains with 60° rotation angle, see Fig. 1.7. Interestingly, DFT calculations [56], [72], [73] reveal that a periodic MTB shows

dispersive and metallic states within the bulk gap of the 2D semiconducting TMDs, while most of the tilt grain boundaries induce strongly localized states [60]. Such a metallic nature has also been experimentally demonstrated by STS [66]. With regard to FET applications, metallic MTBs along the transistor channel may result in a detrimental leakage current flowing through the TMD gap. On the other hand, metallic MTB networks could drive new opportunities for the realization of suited metallic contacts for semiconducting TMDs, as experimentally demonstrated [64]. In the literature, however, electron transport in the presence of MTBs has been barely investigated theoretically, with existing studies mainly focusing on transport across periodic and defect-free grain boundaries [72], [74], [75]. The interplay between MTB states and disorder is one of the main subjects in the present thesis and will be discussed in Chapter 6.

1.4.3 Edges and edge roughness

An important aspect of microelectronics is the progressive miniaturization of the transistors [76]–[78], which enables the reduction of the power consumption, the increase of the switching speed and the large scale integration. Indeed, it is known that, in standard bulk semiconductor-based transistors, miniaturization is associated with performance degradation due to the so-called short-channel effects. The further lateral confinement of the transistor channel, in the case for example of nanowire transistors or FinFETs, exacerbates the problem of roughness at the interface between semiconductor and oxide, thus affecting the charge mobility [79], [80].

We can expect analogous problems for devices based on 2D materials [82], when using nanoribbons [83] as channel for ultrascaled devices. TMD ribbons of very different widths can be fabricated by electrochemical/chemical methods [84], electron irradiation [85], encapsulation in carbon nanotubes [86], electron beam and plasma dry etching [87] or morphological phase transition joint with MBE [81]. The last two techniques are more applicable for mass production from an industrial point of view. A first problem with TMD nanoribbons is the predicted [88]–[90] and experimentally observed [32], [91], [92] presence of metallic edge states within the band gap of the pristine 2D material, also called *bulk band gap*. As for the case of dispersive grain boundary states discussed above, this could be detrimental for transistors, which would be unable to properly switch off. Another serious problem is that, experimentally, nanoribbons usually suffer from edge roughness, see Fig. 1.8. Typical width variations for a 10 nm wide ribbon are in the order of 1 nm, in the optimal conditions of Ref. [81].

Due to the reduced dimensionality of the ribbons, their electronic structure strongly depends on their width. Therefore, as observed for graphene, [93] the transport properties of ultra-narrow TMD ribbons are expected to be

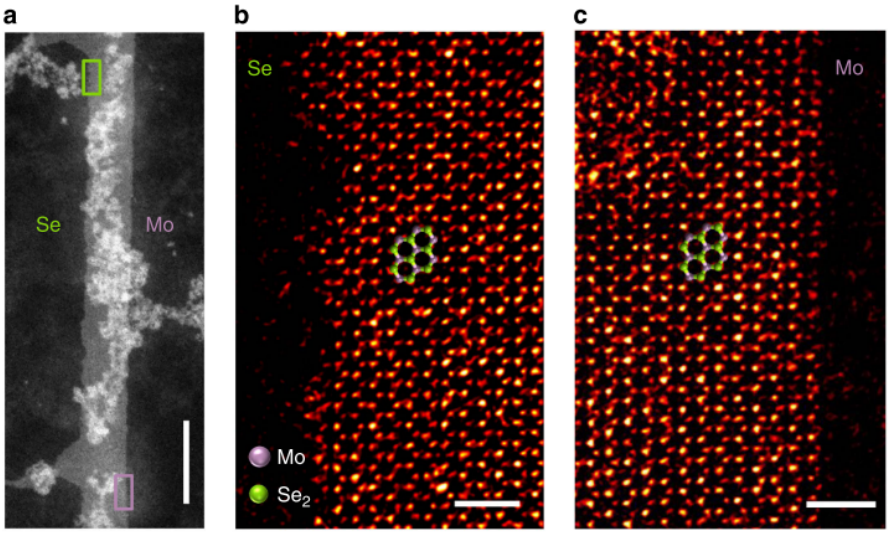

Figure 1.8: Atomistic properties of $MoSe_2$ nanoribbons fabricated by MBE. (a) Large-scale TEM image of a nanoribbon. Yhe scale bar (at the lower right corner) is 20 nm long. Atomic-resolution images in the highlighted green and purple rectangles are shown in (b) and (c), respectively. Note that the edge of (b) and (c) correspond to Se-terminated and Mo-terminated edge, respectively. Scale bars at the bottom in panels (b,c) are 1 nm long. Reprinted from [81]. Copyright (2017) Springer Nature.

significantly affected by roughness. This aspect is subject of study of the present thesis and will be detailed in Chapter 5.

1.5 Possible applications of TMDs in nanoelectronics

After the discovery of graphene, countless studies on 2D materials and their potential applications based on their electrical properties have been reported. Beyond the electronic [10], [11], [13], [94] and optoelectronic [95], [96] applications, including transistors, phototransistors and detectors, 2D materials have been attracting attention for a plethora of original possible applications including, for example, spintronics [97], valleytronics [98], sensors [99] and many others. Furthermore, with a wide variety of different 2D materials, ranging over metallic, semiconducting and insulating materials, limitless combinations of vdW stacking of different layered 2D materials can be synthesized. In this section, I provide a non-comprehensive overview of some possible applications of TMDs focused in the fields of electronics and optoelectronics.

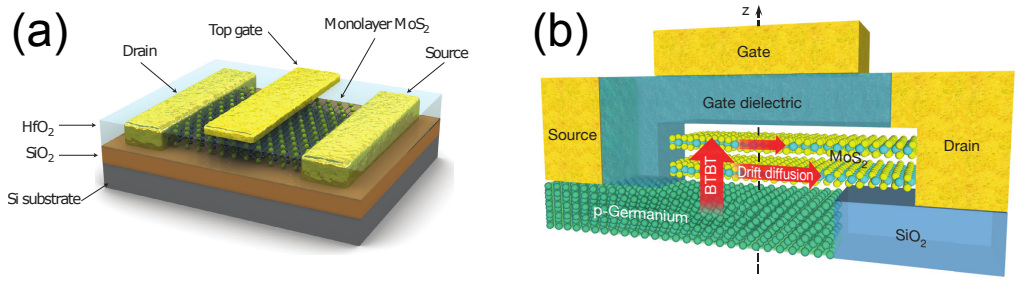

Figure 1.9: Schematics of TMD-based FETs. (a) Conventional FET based on a monolayer MoS_2. Reprinted from [14]. Copyright (2011) Springer Science and Business Media. (b) Tunnel FET, consisting of a channel of Mo_2 and a source of p-type Ge. Reprinted from [103]. Copyright (2015) Springer Science and Business Media.

1.5.1 Electronics

TMDs have attracted much attention for their possible use in electronic applications, particularly FETs, with a great potential for flexible and transparent devices. In particular, semiconducting TMDs with their variety of band alignments and band gaps have been considered for the realization of logic devices. One of the firstly demonstrated TMD-based FETs, a WSe_2-based FET in 2004 [100], showed high p-type mobility ($\sim$500 $cm^2/V{\cdot}s$) with rather low current on/off ratio ($\sim 10^4$), which is inadequate for applications in logic devices. After several years, however, monolayer WSe_2-based FETs [101] successfully demonstrated higher on/off ratio ($\sim 10^6$) thanks to the use of high-κ gate dielectrics. Monolayer MoS_2-based FETs [14] with high electron mobility ($\sim$200 $cm^2/V{\cdot}s$) and on/off ratio ($\sim 10^8$) were also reported, see Fig. 1.9(a). Moreover, TMD-based transistors show the possibility for flexible devices, sustaining a bending strain of 1.5% in MoS_2 FETs [102].

Beyond the typical MOSFETs, tunnel FETs with lateral [10] and vertical [13] structures, as well as energy filtering steep-slope transistors [104] were reported. The 2D-material-based tunnel FETs, which are operated with the band-to-band-tunneling and thus can yield subthreshold swing (SS) below the thermionic limit of $\sim$60 mV/dec at room temperature, are especially suitable for low-power electronics. Indeed, an SS lower than the thermal limit was experimentally observed in bilayer MoS_2 with 3.9 mV/dec [103], see the structure in Fig. 1.9(b). Furthermore, the vdW stacking of different materials [22], [23] opens unprecedented possibilities for the realization of original and complex architectures. All-2D heterostructure tunnel-FETs based on WS_2 layer sandwiched between graphene layers [105] or the vertical junction between $SnSe_2$ and WSe_2 [106] were demonstrated with a sub-thermionic SS, which represent a significant advance towards completely 2D electronics.

Another emerging application domain for 2D TMDs in electronics is that of non-volatile memories [94]. At present, several technologies exist for memories: flash memories based on the charging of a floating gate electrode, resistive memories based on the formation of conductive filaments in an insulating medium, memories based on the polarization of ferroelectric materials, or based on the thermal induction of a phase transition from insulator to conductor. TMDs are useful for enhancing these technologies. For example, graphene can be used as a floating gate and molybdenum disulfide as a dielectric in flash memories [107]. 2D materials can also be employed for new technologies, maybe hardly compatible with Si technology but suitable for flexible, low-cost, printed electronics. Among them, we find resistive memories based on islands of conductive molybdenum disulfide, which act as trapping centers for charges, in a graphene oxide film [108], phase change memories where TMDs are predicted to change phase under doping, strain or heating [109], [110], or even all-2D tunneling memories [111], where graphene acts a floating gate separated by insulating boron nitride from molybdenum disulfide, which acts as transistor channel.

1.5.2 Optoelectronics

The direct band gap, which allows a high light absorption and efficient electron–hole pair generation, observed in several monolayer TMDs has attracted interest for their use in optoelectronics. One of the first demonstrated photodetectors based on MoS_2 [112] achieved an extremely high photoresponsivity of 880 $A \cdot W^{-1}$, which is higher than that of commercial Si photodetectors, and a photoresponse in the 400–680 nm range. Furthermore, the possibility of tuning the band gap depending on the number of layers in the system allows one to vary of the detection range [113]. In addition to MoS_2, other TMDs, including $MoSe_2$ [114], WS_2 [115], and WSe_2 [116], have been used for the phototransistors.

Moreover, thanks to the vdW stacking of different 2D materials, vertically stacked structures have been investigated. Britnell *et al.* [117] demonstrated a photoactive region of semiconducting WS_2 layers sandwiched between graphene electrodes to generate and dissociate the photoexcited electron-hole pairs, thus achieving a photoresponsivity of 0.1 $A \cdot W^{-1}$ and an extrinsic quantum efficient (EQE) of 30%. MoS_2-based devices [118], as shown in Fig. 1.10(a), were also reported and showed that a monolayer yielded higher photoresponsivity comapred to a multilayer. Beyond the single type of TMDs, the n-MoS_2/p-WSe_2 heterostructures of a photoactive part [119] were reported to have the recombination of the majority carriers generated on each layer by the tunneling, see Fig. 1.10(b). This suggests a great potential of TMDs to combine with different 2D materials towards the complete optoelectronic devices based on 2D materials.

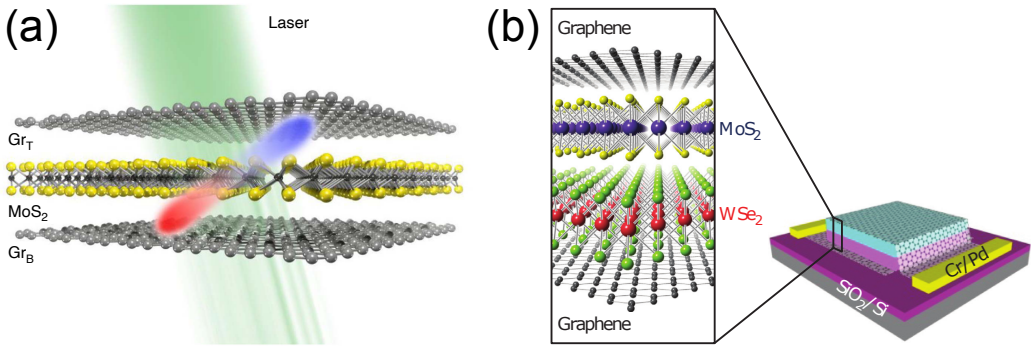

Figure 1.10: Schematic diagrams of the photodetectors based on the vdW stacking of graphene/TMDs/graphene. (a) The photoactive layer of MoS_2. Reprinted from [118]. Copyright (2016) Springer Science and Business Media. (b) The heterostructured photoactive layers of MoS_2/WSe_2. Reprinted from [119]. Copyright (2014) Springer Science and Business Media.

The rich exciton physics observed in TMDs also offers many perspectives for optoelectronic applications [96]. In particular, semiconducting TMDs with a direct band gap have a great potential for light emitters due to the high exciton binding energy (two orders of magnitude larger than in GaAs) and the wide range in the wavelength. For example, monolayer TMDs sandwiched between insulating hBN layers, which act as a barrier, and metallic electrodes of graphene layers, demonstrated efficient light emission with EQE up to 8.4% [120]. An emitter based on a lateral structure of p-n junction based on WSe_2 was also reported, but with a low efficiency of 0.1% [121].

1.6 Goal and structure of the thesis

Among various kinds of 2D materials, the present thesis focuses on semiconducting TMDs since, as discussed in the previous section, they have shown great potential in many fields ranging over electronics and optoelectronics, thanks to their unique properties and the huge range of band alignments and band gaps [122] they offer. Even though researchers have fabricated, deeply analyzed, and applied TMDs in various devices, several issues still remain. For example, and very importantly, the experimental carrier mobility is found to be one order of magnitude smaller than theoretically predicted [123]. This significant difference may come from the joint effect of intrinsic defects of TMDs, contact resistance with electrodes [124], [125], and substrate effect [126]. Above all things, the quality of the materials themselves is the most critical factor to control in view of performing electronic devices based on the TMDs. Indeed, despite the progress of various synthesis techniques, TMDs suffer from their intrinsic defects such as vacancies, roughness, grain

boundaries, etc., as illustrated in Subsec. 1.4. In this respect, understanding the impact of various intrinsic disorders on the transport properties of TMDs becomes crucial for their use in electronics and optoelectronics.

One of the most broadly investigated TMDs both theoretically and experimentally, is monolayer MoS_2 in the 2H phase. It shares common and similar electronic properties with other TMDs from group VI, as the direct band gap at K/K' valleys, and the presence of other valleys at Q and Γ point in the conduction and valence bands, respectively [127].

For all these reasons, in this thesis I focus on MoS_2 as a representative TMD material to numerically investigate the impact of various disorders on the transport properties.

For this study, quantum transport simulations were performed based on a **TB model** and the **Green's function formalism**. The specific TB model, which allows the atomistic description of the disorders investigated in the present thesis, was chosen after the careful consideration of different models, see the details in Chapter 2, and in certain cases calibrated on DFT results. The Green's function formalism for the simulation of quantum transport is briefly reviewed in Chapter 3. Some details of the **numerical codes**, and in particular those I contributed to during my PhD, are reported in Chapter 4.

As the first result of the thesis, Chapter 5 reports on the effect of **edge roughness** in TMD nanoribbons. This study highlights the double role of edge disorder in reducing the charge mobility and, at the same time, in suppressing the edge conductivity. These aspects are crucial in view of the use of TMD nanoribbons in ultra-scaled transistors, where both charge mobility and leakage currents are determinant.

The second focus of this thesis is on the impact of **MTB grain boundaries** and its interplay with short-range or long-range disorder, which is detailed in Chapter 6. This study gives an idea of how conductive grain boundaries in polycrystalline samples can degrade the transport properties and, when present in transistor channels, the device performance. Interesting blocking effects due to spin-valley locking and their robustness against disorder are also highlighted.

Overall, I expect that the present thesis can contribute to the understanding of the impact of various defects on the transport properties of TMDs, and to the progress towards the realization and the design of TMD-based devices.

Chapter 2

Model Hamiltonian for 2D TMDs

2.1 TB model

Both DFT calculations and TB models have been broadly used for the study of TMDs. DFT allows an accurate description of the system but requires high computational efforts for systems with a few hundred atoms. In contrast, though less accurate, TB models have much lower computational cost and are highly flexible for the investigation of large systems with low geometric symmetry and with various defects. In the last few years, several TB models for TMDs have been proposed in the literature. TB models can be classified into two groups depending on the way their parameters are defined: one based on the structural symmetries [128]–[130] and the other based on Slater-Koster (SK) two-center approximation [29], [131]–[133]. The former takes into account the symmetries of the 2D TMD lattices to accurately reproduce the DFT results with a small orbital basis. However, it requires a large number of parameters to be fitted. Furthermore, such models are no longer valid when the bulk symmetries they are based on are broken, as for instance in the presence of geometrical defects. The TB models based on the SK description, on the other hand, can be adapted (up to a certain extent) to describe systems with lower symmetry. To identify the most appropriate model for the description of the disordered systems of TMDs, including geometrical distortions, a comprehensive analysis of TB models are reported in this section.

In Subsec. 2.1.1, I introduce a general TB model and its different parameterizations. In Subsec. 2.1.2, I discuss different TB models of 2D TMDs, reported in literature, and their advantages and disadvantages in terms of the electronic structures. Then, I identify the most appropriate TB model for the description of disordered TMD systems, as those considered during my PhD. Finally, Subsec. 2.1.3 details the origin of SOC, its importance in TMDs, and

its consequences for the electronic properties.

2.1.1 Brief introduction

In condensed matter physics, TB is one of the most largely used methods to describe the electronic structure of systems. This approach, which was firstly proposed by Bloch [134], is based on the use of a linear combinations of atomic orbitals, which constitute a basis of spatially-localized states. Even though this simple model is based on an incomplete atomic orbital basis and (usually) a first-neighbor coupling between them, it allows a fine description of any system regardless of whether it is metallic or semiconducting, and usually over a rather large energy window.

Let us consider, for the sake of illustration, the simple case of a one-dimensional (1D) periodic crystal with a single atom *per* unit cell. The wave function of atomic orbital μ is indicated by $\phi_\mu(\boldsymbol{r})$ and the periodicity of the system is defined by the translation vector $\boldsymbol{t}$. Then, the Bloch sum for the atomic orbital μ, which satisfies Bloch theorem, is defined by

$$\Phi_\mu(\boldsymbol{k},\boldsymbol{r}) = \frac{1}{\sqrt{N}} \sum_{\boldsymbol{t}} e^{i\boldsymbol{k}\cdot\boldsymbol{r}} \phi_\mu(\boldsymbol{r}-\boldsymbol{t}) \ , \tag{2.1}$$

where N is the (large) number of cells in the crystal and the factor $1/\sqrt{N}$ is for the normalization of the Bloch sum. In terms of the Bloch sums, a generic electronic wave function can be written as

$$\psi(\boldsymbol{k},\boldsymbol{r}) = \sum_{\mu} c_\mu(\boldsymbol{k}) \Phi_\mu(\boldsymbol{k},\boldsymbol{r}) \ , \tag{2.2}$$

where $\{c_\mu(\boldsymbol{k})\}$ are the coefficients of the Bloch sums. For this wave function $\psi(\boldsymbol{k},\boldsymbol{r})$ to be an eigenfunction of the system, we solve the Schrödinger equation

$$H\psi(\boldsymbol{k},\boldsymbol{r}) = \Big(\frac{\boldsymbol{p}^2}{2m_\mathrm{e}} + V(\boldsymbol{r})\Big)\psi(\boldsymbol{k},\boldsymbol{r}) = E\psi(\boldsymbol{k},\boldsymbol{r}) \ , \tag{2.3}$$

where $V(\boldsymbol{r})$ denotes a periodic potential, which shows the translational invariance $V(\boldsymbol{r}) = V(\boldsymbol{r}-\boldsymbol{t})$, $\boldsymbol{p}$ is the momentum operator and m_e is the electron mass.

By inserting eq. (2.2) into eq. (2.3) and multiplying by the conjugate transpose of the Bloch sums, we obtain the determinantal compatibility condition for eigenvectors and eigenvalues

$$\Big\| A_{\mu,\nu}(\boldsymbol{k}) - E B_{\mu,\nu}(\boldsymbol{k}) \Big\| = 0 \ , \tag{2.4}$$

where

$$A_{\mu,\nu}(\boldsymbol{k}) = \langle \phi_\mu(\boldsymbol{k},\boldsymbol{r}) | \, H \, | \phi_\nu(\boldsymbol{k},\boldsymbol{r}) \rangle \ , \tag{2.5}$$

$$B_{\mu,\nu}(\boldsymbol{k}) = \langle \phi_\mu(\boldsymbol{k},\boldsymbol{r}) | \phi_\nu(\boldsymbol{k},\boldsymbol{r}) \rangle \ . \tag{2.6}$$

By assuming that the overlap between atomic orbitals is negligible (which is not always the case and may depend on the specific choice of the orbital-like basis), the basis set turns out to be orthonormal, i.e. eq. 2.6 becomes a simple delta function $\delta_{\mu\nu}$. As for $A_{\mu,\nu}(\boldsymbol{k})$ in eq. 2.5, we get

$$A_{\mu,\nu}(\boldsymbol{k}) = \frac{1}{N}\sum_{\boldsymbol{t_a},\boldsymbol{t_b}} e^{i\boldsymbol{k}\cdot(\boldsymbol{t_a}-\boldsymbol{t_b})} \langle\phi_\mu(\boldsymbol{r}-\boldsymbol{t_b})|\, H\, |\phi_\nu(\boldsymbol{r}-\boldsymbol{t_a})\rangle \tag{2.7}$$

$$= \sum_{\boldsymbol{t_a}} e^{i\boldsymbol{k}\cdot\boldsymbol{t_a}} \langle\phi_\mu(\boldsymbol{r})|\, H\, |\phi_\nu(\boldsymbol{r}-\boldsymbol{t_a})\rangle \ , \tag{2.8}$$

where the last equality follows from the translational invariance.

The (one-body) Hamiltonian of a crystal can be expressed as

$$H = \frac{\boldsymbol{p}^2}{2m_\mathrm{e}} + \sum_{\boldsymbol{t_a}} V_a(\boldsymbol{r}-\boldsymbol{t_a}) \ , \tag{2.9}$$

where the potential is the sum of atomic potentials $V_a(\boldsymbol{r})$ centered on each atom. We split the sum in two terms, one for $\boldsymbol{t_a}=0$ and the other for $\boldsymbol{t_a}\neq 0$, thus obtaining from eq. 2.7

$$A_{\mu,\nu}(\boldsymbol{k}) = \sum_{\boldsymbol{t_a}} e^{i\boldsymbol{k}\cdot\boldsymbol{t_a}} \int \phi^*_\mu(\boldsymbol{r})\Big[\frac{\boldsymbol{p}^2}{2m_\mathrm{e}} + V_a(\boldsymbol{r}) + \sum_{\boldsymbol{t'_a}\neq 0} V_a(\boldsymbol{r}-\boldsymbol{t'_a})\Big]\phi_\nu(\boldsymbol{r}-\boldsymbol{t_a})\, d\boldsymbol{r}$$

$$= E_\mu\delta_{\mu\nu} + \sum_{\boldsymbol{t_a}} e^{i\boldsymbol{k}\cdot\boldsymbol{t_a}} \int \phi^*_\mu(\boldsymbol{r}) \sum_{\boldsymbol{t'_a}\neq 0} V_a(\boldsymbol{r}-\boldsymbol{t'_a})\phi_\nu(\boldsymbol{r}-\boldsymbol{t_a})\, d\boldsymbol{r} \ , \tag{2.10}$$

where E_μ is eigenvalue of atomic orbital μ for the isolated atom. The first term of eq. 2.10 is diagonal and the main concern for the second term is that the summation of the potentials includes the coupling of atomic orbitals over the whole crystal. This could be a tremendously demanding problem, and thus we need to limit the coupling between atomic orbitals in a proper way. Thanks to the nature of localized atomic orbitals, we can limit such a coupling to the nearest neighbor atoms, for example. By the two-center approximation, which consists in considering the integrals in eq. 2.10 non-vanishing only when the atomic potential and one of the two orbitals are centered on the same atom, we can write $A_{\mu,\nu}(\boldsymbol{k})$ as

$$A_{\mu,\nu}(\boldsymbol{k}) = E_\mu\delta_{\mu\nu} + \sum_{\boldsymbol{t_\ell}} e^{i\boldsymbol{k}\cdot\boldsymbol{t_\ell}} \int \phi^*_\mu(\boldsymbol{r}) V_a(\boldsymbol{r}-\boldsymbol{t_\ell})\phi_\nu(\boldsymbol{r}-\boldsymbol{t_\ell}) d\boldsymbol{r} \ , \tag{2.11}$$

where the sum over t_ℓ is limited to the translation vector to the nearest-neighbor cells. The limitation of the number of couplings reduces the number of integrals to consider.

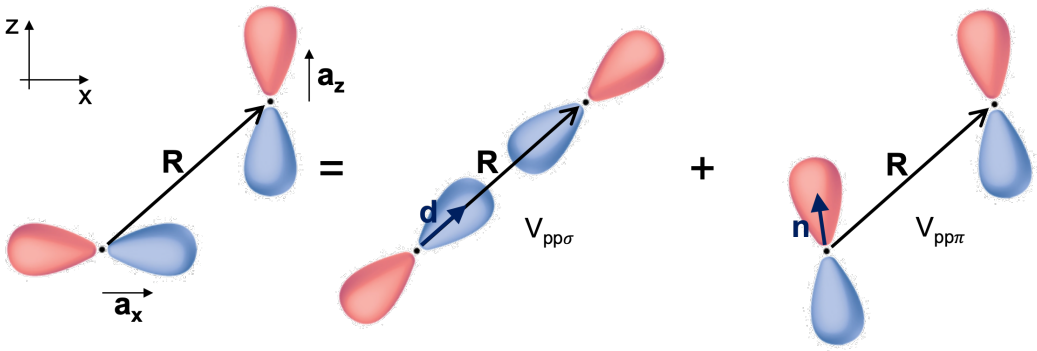

Figure 2.1: SK two-center integral between p_x and p_z atomic orbitals. $\boldsymbol{a_x}$ and $\boldsymbol{a_z}$ are defined as the unit vectors along the axes of the p_x and p_z orbitals, respectively. $\boldsymbol{R}$ indicates the relative position vector. The integral can be expressed by the weighted sum of two parameters, $V_{pp\sigma}$ and $V_{pp\pi}$, see eq. (2.12). $\boldsymbol{d}$ is a unit vector of $\boldsymbol{R}$ and $\boldsymbol{n}$ is a unit vector normal to $\boldsymbol{R}$ in the plane of $\boldsymbol{d}$ and $\boldsymbol{a_z}$.

The energy integrals of eq. 2.10 are unknown, because the atomic potentials are unknown, and can be estimated in two ways. The first one is to fit them directly by comparison with DFT bands and density of states. However, this would entail a huge number of parameters to fit for a large atomic orbital basis, and thus it is not appropriate for our purpose. The other method is the SK parameterization [135], [136], which assumes that the atomic potentials are spherically symmetric and considers the angular symmetry of the orbitals. The two-center integrals can be calculated with a little number of parameters and in terms of the direction cosine (l, m, n) of the relative position vectors between couples of atoms $\boldsymbol{R} = \boldsymbol{R_\nu} - \boldsymbol{R_\mu}$ the two orbitals belong to.

In the case of a system of p atomic orbitals, the energy integrals can be obtained with only two parameters, $V_{pp\sigma}$ and $V_{pp\pi}$, where indices σ and π indicate the perpendicular or parallel orientation of the two p orbitals. As an example of the calculation for SK two-center integrals, Figure 2.1 shows the energy integral between p_x and p_z atomic orbitals. The energy integral E_{p_x,p_z} can be expressed by the sum of two components $V_{pp\sigma}$ and $V_{pp\pi}$, which corresponds to the σ and π bonds with respect to the axis of the vector R, respectively. As calculating each contribution by an inner product with the corresponding unit vector, we obtain

$$E_{p_x,p_z} = (\boldsymbol{a_x} \cdot \boldsymbol{d})(\boldsymbol{a_z} \cdot \boldsymbol{d})V_{pp\sigma} + (\boldsymbol{a_x} \cdot \boldsymbol{n})(\boldsymbol{a_z} \cdot \boldsymbol{n})V_{pp\pi}. \tag{2.12}$$

Since $\boldsymbol{d}$ and $\boldsymbol{n}$ are defined in terms of the direction cosines of $\boldsymbol{R}$, we get

$$E_{p_x,p_z} = lnV_{pp\sigma} - lnV_{pp\pi}. \tag{2.13}$$

Table 2.1 shows the other examples of the SK two-center integrals.

Table 2.1: SK two-center energy integrals $E_{\mu,\nu} = \int \phi_\mu^*(\boldsymbol{r}) V_a(\boldsymbol{r}-\boldsymbol{R}) \phi_\nu(\boldsymbol{r}-\boldsymbol{R}) d\boldsymbol{r}$ between two atomic orbitals ϕ_μ and ϕ_ν. l, m, and n are the direction cosines of the relative distance vector $\boldsymbol{R}$ of the two atoms.

$E_{s,s}$	$V_{ss\sigma}$
E_{s,p_x}	$lV_{sp\sigma}$
E_{p_x,p_x}	$l^2 V_{pp\sigma} + (1-l^2) V_{pp\pi}$
E_{p_x,p_y}	$lmV_{pp\sigma} - lmV_{pp\pi}$
E_{p_x,p_z}	$lnV_{pp\sigma} - lnV_{pp\pi}$
$E_{s,d_{xy}}$	$\sqrt{3}lmV_{sd\sigma}$
$E_{s,d_{x^2-y^2}}$	$\frac{\sqrt{3}}{2}(l^2-m^2)V_{sd\sigma}$
$E_{s,d_{3z^2-r^2}}$	$(n^2 - \frac{1}{2}(l^2+m^2))V_{sd\sigma}$
$E_{p_x,d_{xy}}$	$\sqrt{3}l^2 mV_{pd\sigma} + m(1-2l^2)V_{pd\pi}$
$E_{p_x,d_{yz}}$	$\sqrt{3}lmnV_{pd\sigma} - 2lmnV_{pd\pi}$
$E_{p_x,d_{xz}}$	$\sqrt{3}l^2 nV_{pd\sigma} + n(1-2l^2)V_{pd\pi}$
$E_{p_x,d_{x^2-y^2}}$	$\frac{\sqrt{3}}{2}l(l^2-m^2)V_{pd\sigma} + l(1-l^2+m^2)V_{pd\pi}$
$E_{p_y,d_{x^2-y^2}}$	$\frac{\sqrt{3}}{2}m(l^2-m^2)V_{pd\sigma} - m(1+l^2-m^2)V_{pd\pi}$
$E_{p_z,d_{x^2-y^2}}$	$\frac{\sqrt{3}}{2}n(l^2-m^2)V_{pd\sigma} - n(l^2-m^2)V_{pd\pi}$
$E_{p_x,d_{3z^2-r^2}}$	$l(n^2 - \frac{1}{2}(l^2+m^2)V_{pd\sigma} - \sqrt{3}ln^2 V_{pd\pi}$
$E_{p_y,d_{3z^2-r^2}}$	$m(n^2 - \frac{1}{2}(l^2+m^2)V_{pd\sigma} - \sqrt{3}mn^2 V_{pd\pi}$
$E_{p_z,d_{3z^2-r^2}}$	$n(n^2 - \frac{1}{2}(l^2+m^2)V_{pd\sigma} + \sqrt{3}n(l^2+m^2)V_{pd\pi}$

2.1.2 TB model for MoS_2

In a periodic TMD crystal, the atomic positions are denoted by $\boldsymbol{R} = \boldsymbol{R}_i + \boldsymbol{R}_\alpha$, where $\boldsymbol{R}_i$ is the Bravais lattice vector corresponding to the cell μ, and $\boldsymbol{R}_\alpha$ is the basis vector that identifies the atom (α = Mo, S^t, and S^b with t and b indicating the top and bottom layers in the specific case of MoS_2) within the unit cell as shown in Fig. 1.2. With these three atoms *per* unit cell, the Bloch sum of eq.2.1 is expressed as

$$\Phi_{\alpha,\mu}(\boldsymbol{k},\boldsymbol{r}) = \frac{1}{\sqrt{N}} \sum_{\boldsymbol{R_i}} e^{i\boldsymbol{k}\cdot(\boldsymbol{R_i}+\boldsymbol{R_\alpha})} \phi_{\alpha,\mu}(\boldsymbol{r}-\boldsymbol{R_i}-\boldsymbol{R_\alpha}) \ , \tag{2.14}$$

where $\phi_{\alpha,\mu}(\boldsymbol{r})$ is the wave function of the μ orbital of the α atom. The atomic orbital index μ runs over five d orbitals (d_{z^2}, d_{xy}, $d_{x^2-y^2}$, d_{zx}, d_{yz}) for α=Mo, three p orbitals (p_x^t, p_y^t, p_z^t) for α=S^t, and three p orbitals (p_x^b, p_y^b, p_z^b) for α=S^b. This choice, which is valid for the specific TB model we select, takes into account the main orbitals that, according to DFT calculations, contribute to the states with energy close to the charge neutrality point. However, different TB models may consider a basis with a smaller number of orbitals or linear combinations between them, as mentioned below. Note that we consider an orthonormal set of orbitals as in Subsec. 2.1.1, i.e.

$$\int d\boldsymbol{r}\ \phi_{\alpha,\mu}(\boldsymbol{r}-\boldsymbol{R_i}-\boldsymbol{R_\alpha})\ \phi^*_{\beta,\nu}(\boldsymbol{r}-\boldsymbol{R_j}-\boldsymbol{R_\beta}) \ = \ \delta_{ij}\ \delta_{\alpha\beta}\ \delta_{\mu\nu} \ . \tag{2.15}$$

Starting from this basis set of the eleven atomic orbitals *per* unit cell, the matrix elements of the k-dependent Hamiltonian for the periodic system are expressed as

$$\langle \Phi_{\alpha,\mu}(\boldsymbol{k},\boldsymbol{r})|H|\Phi_{\beta,\nu}(\boldsymbol{k},\boldsymbol{r})\rangle = \sum_{\boldsymbol{R_i}} e^{i\boldsymbol{k}\cdot(\boldsymbol{R_i}+\boldsymbol{R_\beta}-\boldsymbol{R_\alpha})} t_{\alpha\mu,\beta\nu}(\boldsymbol{R_i}+\boldsymbol{R_\beta}-\boldsymbol{R_\alpha}) + \epsilon_{\alpha\mu}\delta_{\alpha\mu,\beta\nu} \ , \tag{2.16}$$

where $\epsilon_{\alpha\mu}$ denotes the on-site energy of the μ orbital of the α atom, and $t_{\alpha\mu,\beta\nu}$ is the hopping energy integral of eq. 2.10 between the μ orbital of the α atom and the ν orbital of the β atom. For TMDs, the literature offer two possible ways of obtaining these hopping energies: within the frame of the structural symmetries [128]–[130] or by SK description [29], [131]–[133]. Different models may consider a different number of orbitals, as mentioned above, which of course gives rise to Hamiltonian matrices with different size.

Before introducing and comparing the different TB models, I would like to discuss the role of the mirror inversion symmetry with respect to the central layer of Mo atoms in the pristine structure. This symmetry allows a unitary transformation from the p orbitals of S^t and S^b to their symmetric and antisymmetric combinations with respect to the transformation $z \to -z$. The transformed atomic orbital bases are listed on the right column in Table 2.2. The Hamiltonian expressed on the transformed basis can be divided into two

Table 2.2: Atomic orbitals in TB model and transformed ones under xy mirror reflection symmetry (M1). t and b denotes the top- and bottom-layer sulfur atoms. E and O indicate the parity of the basis functions with respect to the mirror symmetry.

Index	Basis function	Basis function (M1)
1	d_{z^2}	(E)
2	d_{xy}	(E)
3	$d_{x^2-y^2}$	(E)
4	d_{zx}	(O)
5	d_{yz}	(O)
6	p_x^t	$p_x^e = \frac{1}{\sqrt{2}}(p_x^t + p_x^b)$ (E)
7	p_x^b	$p_x^o = \frac{1}{\sqrt{2}}(p_x^t - p_x^b)$ (O)
8	p_y^t	$p_y^e = \frac{1}{\sqrt{2}}(p_y^t + p_z^b)$ (E)
9	p_y^b	$p_y^o = \frac{1}{\sqrt{2}}(p_y^t - p_y^b)$ (O)
10	p_z^t	$p_z^e = \frac{1}{\sqrt{2}}(p_z^t - p_z^b)$ (E)
11	p_z^b	$p_z^o = \frac{1}{\sqrt{2}}(p_z^t + p_z^b)$ (O)

uncoupled blocks with respect to the mirror symmetry, corresponding to even basis functions, H_E, and odd basis functions, H_O, as given by

$$H_{TB} = \begin{pmatrix} H_E & 0 \\ 0 & H_O \end{pmatrix} . \tag{2.17}$$

The H_E and H_O matrices are given by

$$H_{E/O} = \begin{pmatrix} E_{Mo}^{E/O} + H_{Mo-Mo}^{E/O} & H_{Mo-S}^{E/O} \\ H_{S-Mo}^{E/O} & E_S^{E/O} + H_{S-S}^{E/O} \end{pmatrix} , \tag{2.18}$$

where $E_{Mo}^{E/O}$ and $E_S^{E/O}$ denote the on-site energy matrices for Mo and S, respectively, $H_{Mo-Mo}^{E/O}$ and $H_{S-S}^{E/O}$ are the hopping energy matrices between atomic orbitals within the same types of atom, and $H_{Mo-S}^{E/O}$ is the hopping matrix between the different types of atom, namely Mo and S atoms. With this classification, the eigenvalues of each block, i.e. the energy bands, can be calculated separately. This reduces the computational cost dramatically, and that is why most of the available TB models make use of the transformed basis of Table 2.2.

Dias *et al.* [137] analyzed the electronic structures obtained by different TB models and compared them to those obtained by DFT calculations, see Fig. 2.2. Figures 2.2(a) and (b) show the band structure of monolayer MoS_2 obtained by the 3-band model with only three d orbitals (indices 1, 2, 3 in Table 2.2), which considers the nearest-neighbor (NN) Mo-Mo hopping energies and up to the third nearest-neighbor (TNN) Mo-Mo hopping energies,

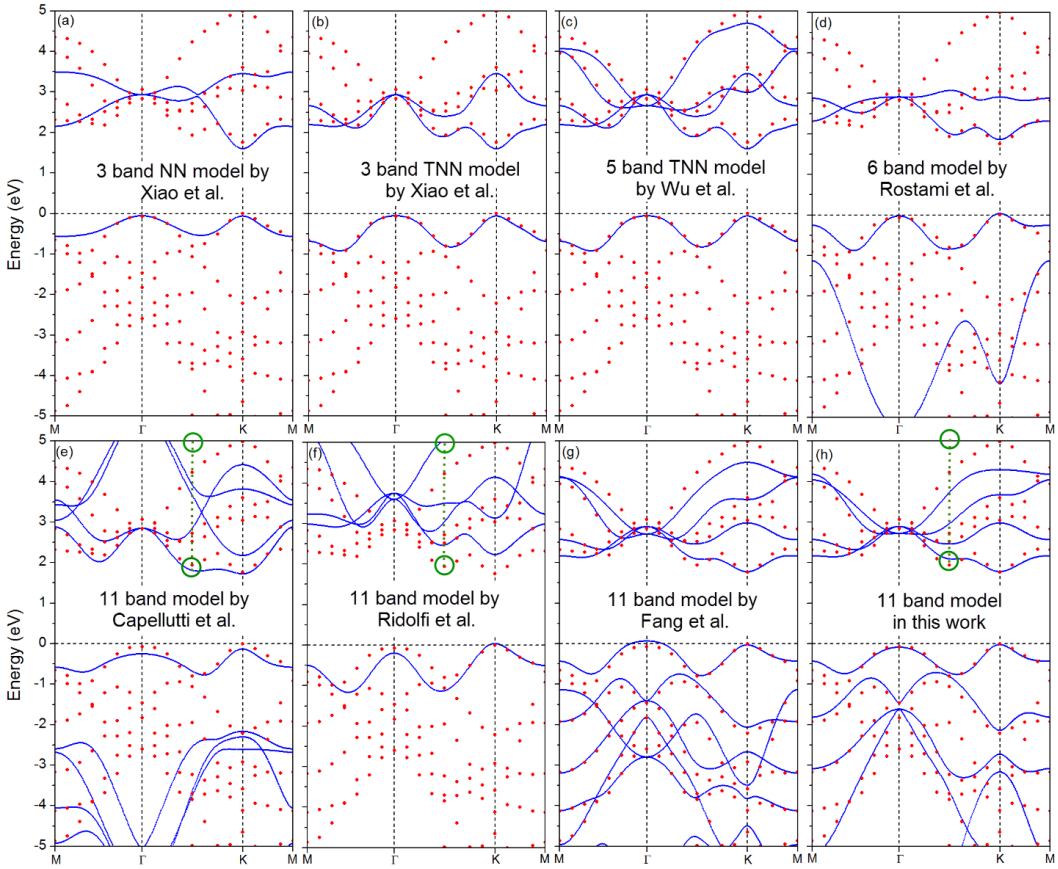

Figure 2.2: Band structures of monolayer MoS_2 along the path M-Γ-K-M, obtained by DFT calculation (red dots) with GGA-PBE pseudopotential and by TB models (blue curves). (a) 3-band NN model with 8 parameters by Xiao *et al.* [129], (b) 3-band TNN model with 19 parameters by Xiao *et al.* [129], (c) 5-band model with 28 parameters by Wu *et al.* [128], (d) 6-band model with 11 parameters by Rostami *et al.* [133], (e) 11-band model with 12 parameters by Capellutti *et al.* [132], (f) 11-band model with 12 parameters by Ridolfi *et al.* [29], (g) 11-band model with 36 parameters by Fang *et al.* [130], and (h) 11-band model with 31 parameters by Dias *et al.* [137]. In (e), (f), and (h), where the 11-band TB calculations are all based on the SK method, the dotted green line bridging two green circles represents the location of Q point in momentum space. Reprinted from [137]. Copyright (2018) American Physical Society.

respectively. The latter shows well-reproduced bands over the whole BZ, including at K, Γ, and even Q points, while the former is accurate only in the vicinity of K and Γ points. The model taking into account the TNN hopping energies, however, requires a much larger number of 19 parameters compared to the 8 parameters for the former model. The band structure obtained by the 5-band model of Wu *et al.* [128] shows a better fitting with the DFT result on the conduction band over approximately 2 eV, see Fig. 2.2(c). All the models

above only take into account d orbitals. Therefore, they cannot be used to describe systems with defects concerning the S atoms, as vacancies. The model proposed by Fang *et al.* [130], on the contrary, considers all the orbitals in Table 2.2, which includes p orbitals for S and d orbitals for Mo. The band structure calculated with this model shows a good agreement with DFT over the whole BZ and over a large energy window, see Fig. 2.2(g). Even though these models based on the structural symmetries provide a rather accurate description, they are difficult to extend to systems with low symmetry, such as nanoribbons, or in the presence of certain types of disorder such as vacancies.

TB models based on the SK parametrization are more flexible and adaptable, since they are not based on the symmetry of the bulk system, but on the relative positions between the atomic orbitals. Moreover, they require a smaller number of the parameters to be fitted compared to that based on the structural symmetries. Rostami *et al.* [133] use the 6-band model with the even basis set (indices 1-3, 6, 8, and 10 of the transformed basis in Table 2.2). The DFT band structure is well reproduced in the vicinity of the K and Γ points, see Fig. 2.2(d). Furthermore, it gives reliable effective masses for both electrons and holes at the K point. However, a weakness of this model, which uses only the even basis, appears when the odd-parity bands take importance as, for instance, for the edge states in nanoribbons [138]. The 11-band model proposed by Capellutti *et al.* [132] is based on the complete set of the d orbitals for Mo and of the p orbitals for S with only 12 parameters. The corresponding band structure in Fig. 2.2(e), however, turns out to be inaccurate except for the K valleys. This behavior is expected to result from taking into account only NN Mo-Mo, S-S, and Mo-S hopping energies in the model. Ridolfi *et al.* [29] consider the same basis and coupling range, but the fitting was performed with the data obtained by the hybrid HSE06 exchange-correlation functional, which gives a reliable band gap, see Fig. 2.2(f). The band structure shows a better dispersion including Γ and Q points, however it is limited to a small energy window around the band edges. Note that the mismatch of the conduction bands with the DFT result is consequence of the different GGA-PBE functional adopted for the DFT calculations. While the previous two models with 11-band Hamiltonian reproduce the DFT band structure only within a window of $\sim$1 eV from the edges, the recent work proposed by Dias *et al.* [137] reproduces the band structure over the whole energy window in Fig. 2.2(h). This accuracy in the band structure is due to the consideration of next-NN hopping parameters of both Mo-Mo and S-S atoms into the model. With such a model, however, it is difficult to describe systems with broken mirror reflection symmetry, as for sulfur vacancies or rippled structures, since the TB parameterization is performed by using the transformed basis of Table 2.1 constructed under the mirror symmetry. Therefore, the model proposed by Ridolfi *et al.* [29] can be the most appropriate for our purpose, in the sense that it is based on the SK description and allows us to reasonably describe the disordered system with atomic vacancies or geometric

distortion. Note that the energy window where the model is accurate is only ∼1 eV from the edges of the valence and conduction bands according to the band structure of 2D MoS_2, see Fig. 2.2(f).

2.1.3 Spin-orbit coupling

As discussed in Subsec. 1.2.2, the effect of SOC is significantly important in TMDs. More precisely, it induces a large and opposite spin-splitting of the valence band in the K and K' valleys [139]. Before discussing the SOC Hamiltonian for TMDs, we briefly illustrate the origin of SOC by using a semi-classical model according to the derivation of ref. [140]. More formally, SOC follows from a low-energy approximation of the relativistic Dirac equation, but we prefer here to provide a more intuitive, though not rigorous, derivation.

Let us consider the case of an electron in orbit around the atomic nucleus. In the electron's reference frame, the nucleus is moving around the electron, see Fig. 2.3(a). This moving positive charge induces a magnetic field, which interacts with the spin magnetic moment of the electron and tends to align it along the magnetic field. We can write the Hamiltonian related to the torque as

$$H = -\boldsymbol{\mu} \cdot \boldsymbol{B} \ , \tag{2.19}$$

where $\boldsymbol{B}$ is the magnetic field induced by the moving positive charge and $\boldsymbol{\mu}$ is the dipole moment of the electron. Let us focus on the simple case of the hydrogen atom, where the positive charge of the nucleus is that of a single proton. In the reference frame of the electron, the proton moving around the electron produces a current I, which flows along a ring with radius r. According to the Biot-Savart law, this current induces a magnetic field

$$B = \frac{\mu_0 I}{2r} \ . \tag{2.20}$$

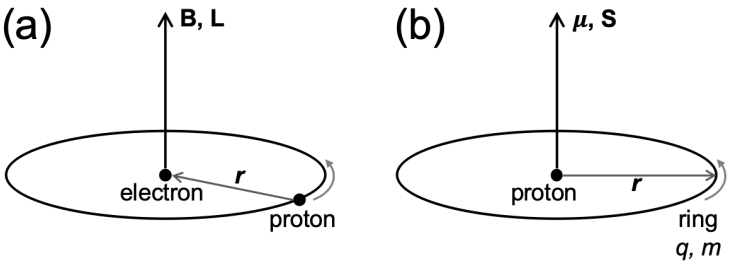

Figure 2.3: Schematic structure of a hydrogen atom for the SOC. (a) A positive charge, which corresponds to the proton, is orbiting the electron in the rest frame of the electron. (b) A ring of charge, which corresponds to the electron, rotates about its axis.

The current is expressed as $I = e/T$, where $e > 0$ is the proton charge and T is the period of the orbit. In the rest frame of the nucleus, the orbital angular momentum of the electron, which is along the same direction as the magnetic field $\boldsymbol{B}$, is $L = rm(2\pi r/T)$. Then, the magnetic field can be expressed in terms of L as

$$\boldsymbol{B} = \frac{\mu_0}{4\pi}\frac{e}{mr^3}\boldsymbol{L} \ . \tag{2.21}$$

We derive the magnetic dipole moment of the electron orbiting with radius r and period T. The current of the ring is defined as q/T where q is the electron charge, see Fig. 2.3(b). The magnetic dipole moment of this ring is the product of the current by the area of the ring

$$\mu = \frac{q\pi r^2}{T} \ . \tag{2.22}$$

And the angular momentum S of a ring with the mass m is calculated by the multiplication of the moment of inertia and the angular velocity as

$$S = \frac{2\pi m r^2}{T} \ . \tag{2.23}$$

The magnetic dipole moment and the angular momentum are aligned and thus we can derive the relation between them

$$\boldsymbol{\mu} = \Big(\frac{q}{2m}\Big)\boldsymbol{S} \ . \tag{2.24}$$

However, this is the result in the classical electrodynamics. According to the Dirac's relativistic theory of the electron, the magnetic moment of the electron turns out to be twice the classical value, so

$$\boldsymbol{\mu_e} = -\frac{e}{m}\boldsymbol{S} \ . \tag{2.25}$$

Using eqs. 2.21 and 2.25, the resulting Hamiltonian of eq. 2.19 can be expressed as

$$H = \frac{\mu_0}{4\pi}\frac{e^2}{m^2r^3}\boldsymbol{L}\cdot\boldsymbol{S} \ . \tag{2.26}$$

By considering the rest frame of the electron, however, we have to take into account that this it not an inertial reference frame. As the electron accelerates around the nucleus in the rest frame of the nucleus, the positive charge does around the electron in the rest frame of the electron. The Thomas precession is a kinematic correction of this error by a factor of $\frac{1}{2}$, as a result, the Hamiltonian for SOC is defined as

$$H = \frac{\mu_0}{8\pi}\frac{e^2}{m^2r^3}\boldsymbol{L}\cdot\boldsymbol{S} \ . \tag{2.27}$$

We can now analyze the effect of SOC in TMDs. The SOC Hamiltonian can be established in terms of a pure intra-atomic SOC [131], [138], which is given by

$$H_{SOC} = \sum_{\alpha} \frac{\lambda_\alpha}{\hbar} \boldsymbol{L_\alpha} \cdot \boldsymbol{S_\alpha} \ , \tag{2.28}$$

where λ_α is the intra-atomic SOC constant for each atom (α=Mo, S), $\boldsymbol{L}$ is the atomic orbital angular momentum operator and $\boldsymbol{S}$ is the electron spin operator. This SOC Hamiltonian is consistent with the result of the simple model for the hydrogen, whose Hamiltonian of eq. (2.27) contains exclusively the term $\boldsymbol{L} \cdot \boldsymbol{S}$.

For the intra-atomic SOC constant λ_α, we used 75 meV for Mo and 52 meV for S [131], which well reproduce the band spin-splitting at the K and K' points, see Fig. 2.4. Using these values in the TB formulation results in a spin-splitting of 151 meV at the K point of 2D MoS_2, which is in good agreement with the experimental value of 145 ± 4 meV [141].

2.2 k·p theory

The k·p methodology is a widely used theoretical approach in order to explore 2D TMD semiconductors [127], [142]–[144]. This approach exploits the symmetries of the system and provides an accurate energy dispersion of the valence band (VB) and the conduction band (CB) in the vicinity of special k-points, for example K/K', in terms of a relatively small number of parameters

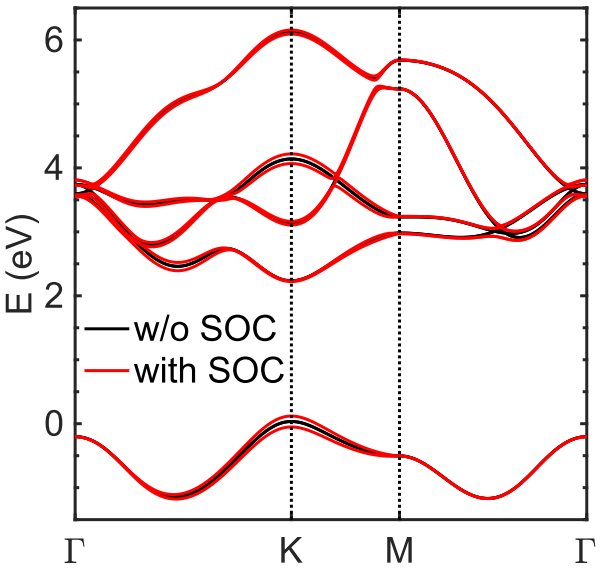

Figure 2.4: Comparison of the band structures in the absence (black lines) and in the presence (red lines) of SOC by using the TB parameterization of Ref. [29].

as compared to the TB method. The number of these parameters is determined by the symmetry of the system and their values are fitted with the DFT energy dispersion in the vicinity of the selected high symmetry points.

There are many k·p models for TMDs, which allow the investigation of the electronic, optical and transport properties in an energy window around the band gap. One of the simplest models is derived by adding a mass term to the Dirac equation for graphene, which has a similar hexagonal lattice. More advanced models are also available, which provide a more detailed description of TMDs, including effects such as TW of the energy dispersion of the VB and the asymmetry between electron and hole bands. In this section, a brief introduction of the k·p model is provided and some models for TMDs are illustrated.

While we do not make use of k·p Hamiltonians in our transport simulations, because they lack the necessary atomistic accuracy, they are helpful to illustrate the physics of the band structure of TMDs, and in particular the role of SOC in the splitting of the VB.

2.2.1 A brief introduction

For a simple illustration of the k·p theory, let us consider the Schrödinger equation eq. (2.3) for a periodic one-electron system. We consider a Bloch function for ψ in the form

$$\psi_{n,\boldsymbol{k}}(\boldsymbol{r}) = e^{i\boldsymbol{k}\cdot\boldsymbol{r}} u_{n,\boldsymbol{k}}(\boldsymbol{r}), \tag{2.29}$$

where n is the band index, $\boldsymbol{k}$ is the electron wave number and $u_{n,\boldsymbol{k}}(\boldsymbol{r})$ has the periodicity of the crystal lattice, i.e. $u_{n,\boldsymbol{k}}(\boldsymbol{r}+\boldsymbol{t}) = u_{n,\boldsymbol{k}}(\boldsymbol{r})$, where $\boldsymbol{t}$ is a translation vector of the lattice. By combining eq. (2.3) and eq. (2.29), we obtain

$$H\psi_{n,\boldsymbol{k}}(\boldsymbol{r}) \;=\; \Big(\frac{\boldsymbol{p}^2}{2m_e} + V\Big) e^{i\boldsymbol{k}\cdot\boldsymbol{r}} u_{n,\boldsymbol{k}}(\boldsymbol{r}) \;=\; E_n(\boldsymbol{k})\; \psi_{n,\boldsymbol{k}}(\boldsymbol{r})\;. \tag{2.30}$$

In real space, the momentum operator $\boldsymbol{p}$ is expressed as $-i\hbar\nabla$. Then, we rewrite eq. (2.30) as

$$\begin{aligned} H\psi_{n,\boldsymbol{k}}(\boldsymbol{r}) &= \frac{\boldsymbol{p}}{2m_e} \cdot \left[\hbar\boldsymbol{k} e^{i\boldsymbol{k}\cdot\boldsymbol{r}} u_{n,\boldsymbol{k}}(\boldsymbol{r}) + e^{i\boldsymbol{k}\cdot\boldsymbol{r}} \boldsymbol{p}\cdot u_{n,\boldsymbol{k}}(\boldsymbol{r})\right] + V(\boldsymbol{r}) e^{i\boldsymbol{k}\cdot\boldsymbol{r}} u_{n,\boldsymbol{k}}(\boldsymbol{r}) \\ &= \frac{1}{2m_e}\left[\hbar^2 k^2 e^{i\boldsymbol{k}\cdot\boldsymbol{r}} u_{n,\boldsymbol{k}}(\boldsymbol{r}) + 2\hbar e^{i\boldsymbol{k}\cdot\boldsymbol{r}} (\boldsymbol{k}\cdot\boldsymbol{p}) u_{n,\boldsymbol{k}}(\boldsymbol{r}) + e^{i\boldsymbol{k}\cdot\boldsymbol{r}} p^2 u_{n,\boldsymbol{k}}(\boldsymbol{r})\right] + V(\boldsymbol{r}) e^{i\boldsymbol{k}\cdot\boldsymbol{r}} u_{n,\boldsymbol{k}}(x) \\ &= E_n(\boldsymbol{k})\; e^{i\boldsymbol{k}\cdot\boldsymbol{r}}\; u_{n,\boldsymbol{k}}(\boldsymbol{r})\;. \end{aligned} \tag{2.31}$$

Here, we define the Hamiltonian as the sum of two terms as

$$H \;=\; H_0 \;+\; H_k\;, \tag{2.32}$$

where H_0 is the unperturbed Hamiltonian for the free electron, which is independent of k and is given by

$$H_0 \equiv \frac{\boldsymbol{p}^2}{2m_e} + V(\boldsymbol{r}) \ , \tag{2.33}$$

and H_k is the k-dependent Hamiltonian term expressed by

$$H_k \equiv \frac{\hbar}{m_e} \boldsymbol{k} \cdot \boldsymbol{p} + \frac{\hbar^2 \boldsymbol{k}^2}{2m_e} \ . \tag{2.34}$$

When k is in the vicinity of 0, H_k is close to zero and can thus be considered as a perturbation. Note that a similar perturbation method can be performed around any k-point of interest, even if it is not 0. The k·p theory is based on this k-dependent Hamiltonian and the perturbation theory, which is valid in vicinity of the chosen k-point in the BZ.

2.2.2 k· p model for TMDs

Since many of the interesting properties of TMDs, such as the spin and valley physics, mainly appear in the vicinity of the K/K' points, as shown in Subsec. 1.2.2, most k·p models have been proposed to describe TMDs around these points. One of the simplest models is the 2-band Hamiltonian firstly proposed by Xiao *et al.* [145], which considers one CB and one VB. This model takes into account both the valley and the spin degrees of freedom to detail the opposite spin-splitting at the inequivalent valleys K/K', which is particularly important for the VB. The k·p Hamiltonian of this model is based on that of massive Dirac fermions, which indicates that MoS_2 can be described by the Hamiltonian of a monolayer graphene with a staggered sublattice potential

$$H_D = \hbar v_0 (\tau k_x \hat{\sigma_x} + k_y \hat{\sigma_y}) + \frac{\Delta}{2} \hat{\sigma_z} \ , \tag{2.35}$$

where τ is the valley index 1(-1) for the K(K') valley, σ_α (α= x, y, z) denotes the Pauli matrices and operates on the CB/VB index, Δ is the band gap of MoS_2, and v_0 corresponds to the Fermi velocity.

Unlike graphene, however, SOC plays an important role in MoS_2, as mentioned in Subsec. 1.2.2. In particular, a large spin-splitting occurs at the edges of the VB, while it is relatively small for the CB. By taking into account only the spin-splitting of the VB, the SOC Hamiltonian [145] can be expressed as

$$H_{SOC} = \lambda \tau \frac{1 - \hat{\sigma}_z}{2} \hat{s}_z \ , \tag{2.36}$$

where 2λ is the SOC-induced spin-splitting energy on the top of the VB, and $\hat{s}_z$ is the Pauli matrix for spin. This simple SOC Hamiltonian explicitly describes the opposite spin-splitting at K/K' valleys.

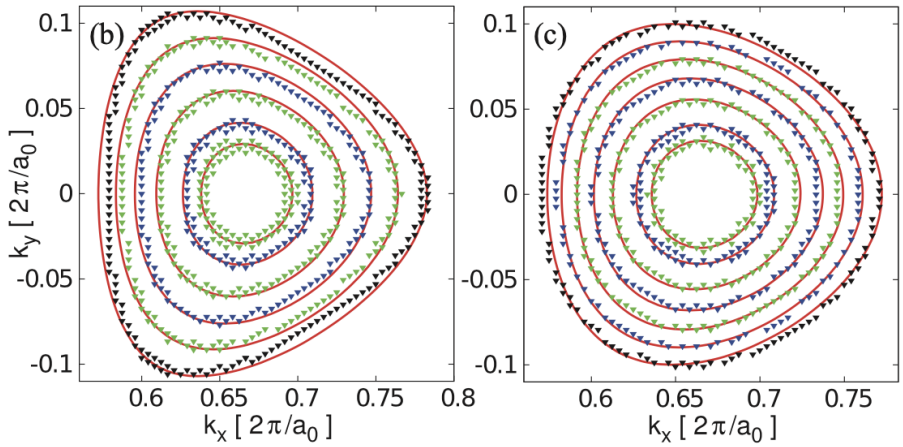

Figure 2.5: Isoenergy contours of VB and CB by DFT calculations (symbols) and k·p model (continuous lines) in the vicinity of K point. Reprinted from Ref. [146]. Copyright (2013) American Physical Society.

However, this model does not encompass some important features such as the TW effect of the energy dispersion and electron-hole asymmetry [85], [146], which results in different electron and hole effective masses. Compared to graphene, where the TW effect is observed starting from ∼1 eV from the band edges, for MoS_2 the effect is already observed at ∼80 meV from the band edges, particularly at the VB, see Fig. 2.5. To go beyond the simple model and capture these properties, several other k·p models have been proposed. One of the most complete k·p models is proposed by Kormányos *et al.* [127]. The effective Hamiltonian is derived from a seven-band model by systematically eliminating all degrees of freedom except those corresponding to the VB and the CB, by using the Löwdin partitioning. The model makes use of the spinful basis $\left|\Psi^{vb,cb}, s\right\rangle = \left|\Psi^{vb,cb}\right\rangle \bigotimes |s\rangle$, where $\left|\Psi^{vb,cb}\right\rangle$ is the spinless Bloch wave function for the VB or the CB, and s denotes the spin degree of freedom.

The low-energy effective-Hamiltonian $H_{eff}^{\tau,s}$ is expressed by

$$H_{eff}^{\tau,s} = H_0 + H_{k\cdot p}^{\tau,s} + H_{SOC}^{\tau,s} \ , \tag{2.37}$$

where H_0 is the free-electron term, $H_{k\cdot p}^{\tau,s}$ corresponds the k·p Hamiltonian, and $H_{SOC}^{\tau,s}$ denotes the SOC Hamiltonian. The Hamiltonian for the free-electron is defined as

$$H_0 = \frac{\hbar^2 \boldsymbol{q}^2}{2m_e} \mathbb{1} \ , \tag{2.38}$$

where $\mathbb{1}$ is a unit matrix in the electron-hole space, m_e is the free electron mass, and $\boldsymbol{q} = (q_x, q_y)$ is the wave vector measured from the K/K' valleys in momentum space.

The SOC Hamiltonian takes into account the spin-splitting of both the VB and the CB, in contrast to the SOC Hamiltonian of eq. (2.36), which only considers the spin-splitting of the VB. This SOC Hamiltonian is expressed by

$$H_{SOC}^{\tau,s} = \begin{pmatrix} \tau\Delta_{vb}\hat{s_z} & 0 \\ 0 & \tau\Delta_{cb}\hat{s_z} \end{pmatrix} , \tag{2.39}$$

where Δ_{vb} and Δ_{cb} denote the strength of the spin-splitting at VB and CB, respectively, and the index τ=1(-1) denotes the valley K(-K). In TMDs, the spin-splitting at the CB is much lower than that at the VB. For MoS_2, $2\Delta_{cb}$ and $2\Delta_{vb}$ are 3 meV and 148 meV, respectively.

Finally, the k·p Hamiltonian $H_{k\cdot p}^{\tau,s}$ is composed of four terms

$$H_{k\cdot p}^{\tau,s} = H_D^{\tau,s} + H_{as}^{\tau,s} + H_{3w}^{\tau,s} + H_{cub}^{\tau,s} . \tag{2.40}$$

$H_D^{\tau,s}$ is the massive Dirac fermion model introduced in eq. (2.35). If considered alone, this term would result in electron-hole symmetry and isotropic energy dispersion. To overcome these problems, the k·p Hamiltonian includes two extra terms. $H_{as}^{\tau,s}$ is proposed for the description of the electron-hole asymmetry, expressed by

$$H_{as}^{\tau,s} = \begin{pmatrix} \alpha_{\tau,s}\mathrm{q}^2 & 0 \\ 0 & \beta_{\tau,s}\mathrm{q}^2 \end{pmatrix} , \tag{2.41}$$

where $\alpha_{\tau,s}$ and $\beta_{\tau,s}$ are the parameters for holes and electrons, respectively. The electron-hole symmetry is broken when $\alpha_{\tau,s} \neq \beta_{\tau,s}$. For the TW effect, $H_{3w}^{\tau,s}$ is introduced, which is given by

$$H_{3w}^{\tau,s} = \begin{pmatrix} 0 & \kappa_{\tau,s}(q_+^\tau)^2 \\ \kappa_{\tau,s}^*(q_-^\tau)^2 & 0 \end{pmatrix} , \tag{2.42}$$

where $q_\pm$ is defined as $q_\pm = q_x \pm i\tau q_y$. These off-diagonal terms are quadratic in $q_\pm$ and lead to the TW of the energy dispersion as shown in Fig. 2.5. For a better description, two additional terms are considered in eq. (2.40). The Hamiltonian $H_{cub,1}^{\tau,s}$ is off-diagonal and cubic in $q_\pm$. It plays an important role to obtain a better fitting with DFT results away from the K/K' points. The term $H_{cub,2}^{\tau,s}$ is diagonal and cubic in $q_\pm$, which allows the model to reproduce the non-parabolicity of the bands.

This efficient methodology is widely adopted for the study of optoelectronic properties of TMDs, e.g., the Zeeman effect of intralayer excitons in few-layer TMDs [147], valley polarization of excitons and trions [148], and spin and valley Hall conductivity in the presence of dopants in monolayer TMDs [149].

Despite the nicer picture provided and its physical clarity, this methodology has several limitations. One of the drawbacks is the validity region in the momentum space around the selected k-points, usually the K/K' valleys. While this limitation may be not too severe for the study of optoelectronic

properties, this is not the case for transport properties, since other k-points correspond to states with energy close to the VB and CB edges. For example, the energies at the Γ and Q valleys are practically found to be located at just a few tens or hundreds of meV from the edges of VB and CB, respectively, see Fig. 2.2.

The other aspect, which is difficult to take into account with the k·p theory, is the presence of atomistic defects [74], [138], [150]. Depending on their nature, these defects may induce gap states or activate intervalley scattering, which results in a strong alteration of electron transport. Therefore, the k·p theory is inappropriate for describing disordered systems, which is one of the main objectives of the present study.

2.3 DFT based Hamiltonian

DFT-based Hamiltonians obtained from the projection onto a reduced basis set of maximally localized Wannier functions (MLWFs) have been proposed as a more sophisticated method for an accurate description of TMD materials [130], [139], [151], [152]. We have seen that the accuracy of the electronic structures obtained by various TB models is considerably sensitive to the number of atomic orbitals taken into account for the basis set and to the inclusion of longer-range hopping terms, see Subsec. 2.1.2. At the same time, the k·p theory only provides an accurate description in narrow energy windows and around specific regions of the BZ, as shown in Subsec. 2.2.2. On the contrary, the basis set of MLWFs, which is obtained by a systematic procedure, can give more accurate Hamiltonian, able to reproduce the DFT results over the whole BZ and a larger energy range.

The technique based on Wannier functions was firstly introduced by Gregory Wannier [153], and it consists in a change of basis from the Bloch basis in the momentum space, which is related to eigenstates of the Kohn-Sham Bloch Hamiltonian of DFT calculations, into the localized Wannier basis set in the real space. In the case of an isolated energy band with index n, where *isolated* means that, in the energy range of interest, there are no degeneracy points, such a change of basis is performed by the unitary transformation

$$w_{n,\boldsymbol{R}}(\boldsymbol{r}) = \frac{V}{8\pi^3}\int_{BZ} e^{-i\boldsymbol{k}\cdot\boldsymbol{R}}\psi_{n,\boldsymbol{k}}d\boldsymbol{k}, \tag{2.43}$$

where $\psi_{n,\boldsymbol{k}}$ is the Bloch eigenstates of band n, $w_{n,\boldsymbol{R}}(\boldsymbol{r})$ is the Wannier function corresponding to the primitive cell with lattice vector $\boldsymbol{R}$, and V indicates the volume of the unit cell. This technique [153]–[155] has been extended to bands with degeneracy points, still with the aim of providing a convenient basis of localized functions to conveniently describe the selected bands in a given energy region. Recently, this approach has become popular thanks to

the development of general and efficient algorithms to derive well-localized Wannier functions in the framework of DFT calculations [156]–[159].

The spatially-localized feature of the MLWFs is analogous to that of localized molecular orbitals, and it brings information about the angular momentum and the nature of the chemical bonding (which is lacking from the Bloch picture), thus allowing us to obtain a deeper understanding of chemical coordination and bonding characteristics [160]. Besides this aspect, the MLWFs have been used as an accurate basis for a variety of theoretical studies, and in particular for the construction of effective Hamiltonians, which are useful for the simulation of transport properties [161], strongly-correlated electrons [162], and photonic lattices [163]. As concerns electron transport, the Wannierization process is particularly convenient because (i) it reduces the size of the Hamiltonian, since the number of MLWFs to consider is determined by the energy range of interest, (ii) the localized nature of the Wannier functions limit the Hamiltonian coupling terms to spatially close MLWFs, which makes the slicing process possible and convenient, see Sec. 3.2.

Compared to other 2D materials such as graphene and boron nitride, electronic structure of TMD materials is more complex due to the contribution of d orbitals of the transition metal and p orbitals of the chalcogen atoms, as mentioned in Subsec. 2.1.2. Because of this intricacy, calibrating TB models on the band structures from DFT calculations is challenging and not a standardized procedure. As a consequence, many different TB parameterizations have been proposed in the literature for TMDs, see Subsec. 2.1.2. The

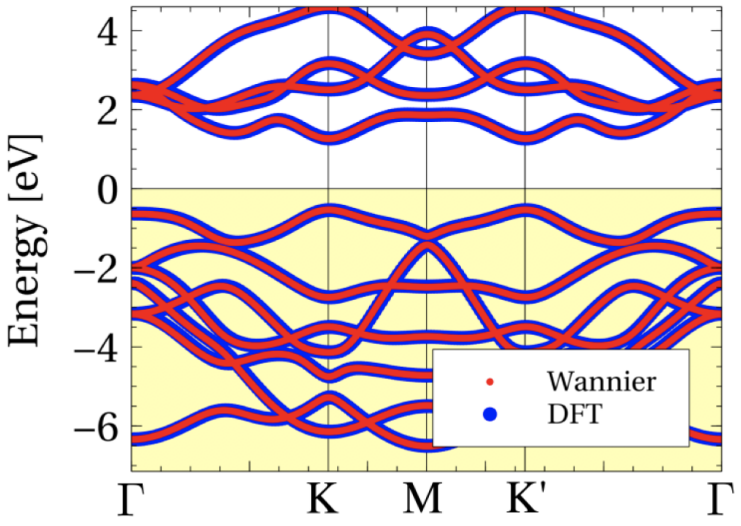

Figure 2.6: Band structure of MoS_2 obtained by DFT calculations (blue dots) and by the Wannier Hamiltonian (red dots). The yellow shadowed region indicates the energy region below the Fermi level. Reprinted from [151]. Copyright (2016) IOP Publishing.

Wannier procedure, on the contrary, is a systematic procedure for which, once the bands to consider and the energy region of interest are defined, the final MLWFs are obtained iteratively from the minimization of the spatial spread of the functions. However, this procedure requires a first guess for the Wannier orbitals, which impacts the success of the minimization. On the basis of our previous analysis, for MoS_2 it is reasonable to consider an initial guess of p orbitals for the S atoms and d orbitals for the Mo. This leads to an 11-band DFT based TB-like Hamiltonian [151], which well reproduce the DFT band structure, see Fig. 2.6, over a larger energy range compared to the other models.

There are several reasons why we do not make use of MLWFs in the present study. First, compared to the TB basis, Wannier functions may be not as much localized, which, in the Hamiltonian, entails a longer-range coupling and then a heavier computational burden for the transport calculation. Also, the Hamiltonian is very specific to the corresponding system simulated by DFT. This means that the results will significantly vary for different geometries or in the presence of defects, thus requiring DFT calculations for different configurations. In other words, the method is not as general and adaptable as a SK parametrization is. Finally, and in relation with the previous point, depending on the size of the system to simulate, the DFT calculations and the following Wannier procedure might be extremely time-consuming.

2.4 Summary

This Chapter is devoted to introduce different models to describe TMDs in terms of the Hamiltonian, which is a primary task for the present thesis. I introduced three different models and reviewed the resulting electronic properties. In particular, the TB model can be classified into two different approaches, the framework of the structural symmetries or the SK description. Although the former may show a nicer electronic structure over a larger energy window, it is difficult to consider a disordered system in the presence of the symmetry breaking. On the other hand, the latter can describe a system regardless of the structural symmetries with atomic defects, of which study is the most important part of the thesis. Moreover, k·p and DFT-based Hamiltonians and their limitations are also discussed. k·p model is valid only around the selected k-points and has a difficulty to take into account atomistic defects. The framework of the DFT-based Hamiltonians uses the basis of Wannier functions that may not require a longer-range coupling, which can results in a heavier computational effort. For all these reasons, the TB model, particularly in the SK description, was used in all this thesis work.

Chapter 3

Quantum transport model

This Chapter summarizes the quantum formalism adopted to simulate electron transport. After introducing the system description and namely the TB Hamiltonian in Chapter 2, we focus here on the Green's function approach for quantum transport. First, in Sec. 3.1, I outline the second quantization formalism, which turns out to be very convenient for the definition of the charge and current operators, whose expectation values are obtained in terms of the Green's functions, as illustrated in Sec. 3.2. I will also discuss some numerical techniques to efficiently calculate the Green's functions of large systems, and in particular the decimation-renormalization technique implemented in the codes. I will finally discuss, in Sec. 3.3, the different quantum transport regimes of disordered conductors. Their properties and statistical analysis will be useful for the study of transport in disordered MoS_2 performed in Chapters 5 and 6.

3.1 Basics of the second quantization formalism

In this section, I briefly illustrate the second quantization formalism, which is useful for the better understanding of the main topic in this chapter: Green's function formalism. What follows is just a summary of the most important aspects and results, with no detailed derivations, which can be found in textbooks [164], [165]. Here we mainly follow Ref. [165].

3.1.1 Second quantization

When considering transport phenomena or many-body interactions, it is convenient to consider a Hilbert space able to describe systems with an undefined number of particles. In the case of many distinguishable particles, a generic states of N particles can be written in term of direct product of single-particle

states in an extended Hilbert states as

$$|n_1\rangle\,|n_2\rangle\ldots|n_N\rangle\ , \tag{3.1}$$

where $|n_i\rangle$ is the single-particle state that describes the particle i. In the case of N identical particles (as electrons or phonons, for example), we use the different notation

$$|n_1 n_2 n_3 \ldots n_N\rangle \tag{3.2}$$

to indicate that one particle is in the state $|n_1\rangle$, one in the state $|n_2\rangle$ and so on. The state in eq. (3.1) must represent the same physical state under the permutation of the particles, since the particles are identical. This means that a permutation just entails a phase factor that depends on the permutation itself. In the case of two identical particles, as an important example, we have

$$|n_2, n_1\rangle = e^{i\alpha_{1\leftrightarrow 2}}\,|n_1, n_2\rangle\ , \tag{3.3}$$

where we considered the inversion $1 \leftrightarrow 2$ and $e^{i\alpha_{1\leftrightarrow 2}}$ is the phase factor. If we apply again the same inversion, we have the identity, for which the phase factor must be 1[1]. This implies that $e^{i\alpha_{1\leftrightarrow 2}} = \pm 1$. Therefore, the state can be either symmetric (for bosons) or antisymmetric (for fermions) under inversion of two particles. Since a generic permutation P can be written as the product of inversions of couples of particles, we have in general

$$\left|n_{P(1)} n_{P(2)} \ldots n_{P(N)}\right\rangle \ = \ (\pm 1)^{\sigma_P}\,|n_1 n_2 \ldots n_N\rangle \tag{3.4}$$

where σ_P is the signature of the permutation, which is even or odd depending on the even or odd number of inversions necessary to obtain the permutation. Note that the above relation implies the Pauli exclusion principle for fermions. In fact, if two fermions are in the same state, their inversion simply gives the same state with a minus sign, which entails that the states is 0, i.e. two fermions cannot occupy the same state.

It is straightforward to show that, if we require the normalization

$$\langle n_1 n_2 \ldots n_N | n_1 n_2 \ldots n_N\rangle \ = \ 1 \tag{3.5}$$

for N particles in different states (i.e. $|n_1\rangle \neq |n_2\rangle \neq \ldots |n_N\rangle$), then

$$\langle n'_1 n'_2 \ldots n'_N | n_1 n_2 \ldots n_N\rangle \ = \ \sum_P (\pm 1)^{\sigma_P} \prod_{i=1}^{N} \delta_{n'_i n_{P(i)}}\ . \tag{3.6}$$

According to the above results, we can express an N-particle state in terms of product of single-particle states, i.e. with the notation of eq. (3.1) as

$$|n_1, n_2 \ldots n_N\rangle = \frac{1}{\sqrt{N!}} \sum_P (\pm)^{\sigma_P} \left|n_{P(1)}\right\rangle \left|n_{P(2)}\right\rangle \ldots \left|n_{P(N)}\right\rangle\ . \tag{3.7}$$

The $N!$-term appearing in the normalization factor corresponds to the fact that there are $N!$ possible permutations for N identical particles.

[1] In reality, this argument is not completely correct, and indeed it can be demonstrated that in 2 dimensions different values can be observed [166]. However, this point is beyond the scope of my presentation.

3.1.2 Fock space and creation/annihilation operators

If we indicate the Hilbert space of N identical particles as $\mathcal{H}_N$, then we can define a larger Hilbert space, called Fock space $\mathcal{F}$, of all the possible states with any particle number as the direct sum of all these spaces, i.e.

$$\mathcal{F} \equiv \mathcal{H}_0 \oplus \mathcal{H}_1 \oplus \mathcal{H}_2 \oplus \dots , \tag{3.8}$$

where $\mathcal{H}_0$ only contains the empty (vacuum) state $|0\rangle$. The second quantization introduces the creation $c_\alpha^\dagger$ operator as a function between Hilbert spaces that operates as follows

$$c_\alpha^\dagger : \mathcal{H}_{n-1} \to \mathcal{H}_n \quad : \quad c_{n_N}^\dagger \, |n_1 n_2 \dots n_{N-1}\rangle \equiv |n_1 n_2 \dots n_{N-1} n_N\rangle . \tag{3.9}$$

Therefore, $c_\alpha^\dagger$ adds a particle in the state α to the state it operates on. This allows us to write

$$|n_1 n_2 \dots n_{N-1} n_N\rangle = c_{n_N}^\dagger \, c_{n_{N-1}}^\dagger \dots \, c_{n_1}^\dagger \, |0\rangle . \tag{3.10}$$

It follows immediately that

$$\begin{aligned} c_\alpha^\dagger c_\beta^\dagger \, |n_1 n_2 \dots n_N\rangle &= |n_1 n_2 \dots n_N \beta \alpha\rangle = (\pm) \, |n_1 n_2 \dots n_N \alpha \beta\rangle \\ &= \pm c_\beta^\dagger c_\alpha^\dagger \, |n_1 n_2 \dots n_N\rangle \to [c_\alpha^\dagger, c_\beta^\dagger]_\mp = 0 , \end{aligned} \tag{3.11}$$

where $[*,*]_-$ and $[*,*]_+$ indicate the commutator and the anticommutator, respectively. The adjoint of $c_\alpha^\dagger$ is the annihilation operator c_α, which removes a particle in the state α

$$c_\alpha : \mathcal{H}_n \to \mathcal{H}_{n-1} : c_{n_N} \, |n_1 n_2 \dots n_{N-1} n_N\rangle \equiv |n_1 n_2 \dots n_{N-1}\rangle \text{ and } [c_\alpha, c_\beta]_\mp = 0. \tag{3.12}$$

Note that applying the annihilation operator to empty states $c_\alpha \, |0\rangle$ is the zero and not the vacuum state $|0\rangle$. A slightly longer derivation, see Ref. [165], allows us to obtain the important third commutation/anticommutation rule

$$[c_\alpha, c_\beta^\dagger]_\mp = \delta_{\alpha,\beta} . \tag{3.13}$$

By means of the commutation/anticommutation rules, we can also demonstrate that the operator $\hat{n}_\alpha \equiv c_\alpha^\dagger c_\alpha$ provides the number of particles in the state $|\alpha\rangle$. Consequently, the operator that counts the total number of particles $\hat{N}$ can be written as

$$\hat{N} = \sum_\alpha c_\alpha^\dagger c_\alpha . \tag{3.14}$$

The above equations are valid for both bosons and fermions.

3.1.3 More about creation/annihilation and field operators

Let us consider the set of the creation and annihilation operators $\{c_\alpha^\dagger\}$ and $\{c_\alpha\}$ associated with an orthonormal basis $\{|\alpha\rangle\}$. The operators $\{d_\beta^\dagger\}$ and $\{d_\beta\}$ associated with a different orthonormal basis $\{|\beta\rangle\}$ can be simply obtained by

$$|\beta\rangle \;=\; \sum_\alpha |\alpha\rangle\,\langle\alpha|\beta\rangle \quad\rightarrow\quad d_\beta^\dagger \;=\; \sum_\alpha \langle\alpha|\beta\rangle\, c_\alpha^\dagger \quad \text{and} \quad d_\beta \;=\; \sum_\alpha \langle\beta|\alpha\rangle\, d_\alpha \;. \tag{3.15}$$

It is straightforward to demonstrate that, thanks to the orthonormality of the basis, the commutation/annihilation rules are preserved:

$$[d_\alpha, d_\beta]_\mp \;=\; [d_\alpha^\dagger, d_\beta^\dagger]_\mp \;=\; 0 \quad \text{and} \quad [d_\alpha, d_\beta^\dagger]_\mp \;=\; \delta_{\alpha,\beta} \;. \tag{3.16}$$

Let us now consider the basis $\{|\boldsymbol{r}\rangle\}$ of the eigenstates of the position operator $\hat{\boldsymbol{r}}$. According to the above equations, we define the field operators $\hat{\psi}^\dagger(\boldsymbol{r})$ and $\hat{\psi}(\boldsymbol{r})$ corresponding to the creation and the annihilation of a particle in the state $|\boldsymbol{r}\rangle$, i.e. at position $\boldsymbol{r}$, as

$$\hat{\psi}^\dagger(\boldsymbol{r}) \;=\; \sum_\alpha c_\alpha^\dagger u_\alpha^*(\boldsymbol{r}) \qquad \text{and} \qquad \hat{\psi}(\boldsymbol{r}) \;=\; \sum_\alpha c_\alpha u_\alpha(\boldsymbol{r}) \;, \tag{3.17}$$

where $u_\alpha(\boldsymbol{r}) \;=\; \langle\boldsymbol{r}|\alpha\rangle$, i.e. $\{u_\alpha(\boldsymbol{r})\}$ are the real-space wave functions associated to a general orthonormal basis $\{|\alpha\rangle\}$. According to these relations, we can define a state of N identical particles at position $\{\mathbf{r_n}\}$ as

$$|\boldsymbol{r}_1, \boldsymbol{r}_2, \;\ldots\; \boldsymbol{r}_N\rangle \;=\; \hat{\psi}^\dagger(\boldsymbol{r}_1)\hat{\psi}^\dagger(\boldsymbol{r}_1)\hat{\psi}^\dagger(\boldsymbol{r}_2)\cdots\hat{\psi}^\dagger(\boldsymbol{r}_N)\,|0\rangle \;. \tag{3.18}$$

One can easily verify that the commutation/anticommutation rules for the field operators are

$$[\hat{\psi}(\boldsymbol{r}), \hat{\psi}(\boldsymbol{r'})]_\mp \;=\; [\hat{\psi}^\dagger(\boldsymbol{r}), \hat{\psi}(\boldsymbol{r'})^\dagger]_\mp = 0 \;\text{ and }\; [\hat{\psi}(\boldsymbol{r}), \hat{\psi}(\boldsymbol{r'})^\dagger]_\mp = \delta(\boldsymbol{r}-\boldsymbol{r'}) \tag{3.19}$$

In addition, we can write the operator of the total number of particles as

$$\hat{N} \;=\; \int d\boldsymbol{r}\; \hat{n}(\boldsymbol{r}) \;, \tag{3.20}$$

where $\hat{n}(\boldsymbol{r}) = \hat{\psi}^\dagger(\boldsymbol{r})\hat{\psi}(\boldsymbol{r})$ is the spatial-density-of-particle operator.

3.1.4 Operators in the second quantization formalism

Let us examine how operators, among which notably the Hamiltonian, are represented and work in the Fock space. For the purpose of this thesis, we limit here to one-body operators, which independently act on each particle

of the systems. For example, an operator acting on a system of N identical particles can be expressed by

$$\hat{O} \;=\; \sum_{i=1}^{N} \hat{o}_i \;, \tag{3.21}$$

where $\hat{o}_i$ acts as the single-particle operator $\hat{o}$ on the ith state of many-particle state and leaves the others unvaried, i.e.

$$\hat{o}_i \;=\; \hat{1}_1 \otimes \hat{1}_2 \otimes \ldots \hat{1}_{i-1} \otimes \hat{o} \otimes \hat{1}_{i+1} \otimes \ldots \hat{1}_N \;. \tag{3.22}$$

When this operator is applied to a state, we simply get

$$\hat{O}\,|n_1, n_2 \ldots n_N\rangle \;=\; |\hat{o}n_1, n_2 \ldots n_N\rangle + |n_1, \hat{o}n_2 \ldots n_N\rangle + \ldots + |n_1, n_2 \ldots \hat{o}n_N\rangle \;. \tag{3.23}$$

Since

$$|n_1, \ldots n_{k-1}, \hat{o}n_k, n_{k+1} \ldots n_N\rangle \;=\; d_k^\dagger c_{n_k}\,|n_1 n_2 \ldots n_N\rangle \;, \tag{3.24}$$

where $d_k^\dagger$ is the creation operator for an electron in the state $\hat{o}\,|n_k\rangle$ and, according to eq. (3.15), is given by

$$d_k^\dagger = \sum_\alpha c_\alpha^\dagger \,\langle\alpha|\hat{o}|n_k\rangle\,, \tag{3.25}$$

where the $|\alpha\rangle$ forms a complete orthonormal basis. We can then write the operator $\hat{O}$ as

$$\hat{O} \;=\; \sum_{\alpha,\alpha'} \langle\alpha|\hat{o}|\alpha'\rangle\, c_\alpha^\dagger c_{\alpha'} \;, \tag{3.26}$$

where $|\alpha\rangle$ and $|\alpha'\rangle$ span the same complete orthonormal basis set. If now we express $\hat{o}\,|n_i\rangle$ in terms of the basis $\{|\boldsymbol{r}\rangle\}$ by using its completeness relation

$$\hat{o}_i\,|n_i\rangle = \int d\boldsymbol{r}\,\langle\boldsymbol{r}|\,\hat{o}_i\,|n_i\rangle\,|\boldsymbol{r}\rangle \;, \tag{3.27}$$

then eq. (3.26) reads

$$\begin{aligned}
\hat{O}\,|n_1, n_2 \ldots n_N\rangle \;&=\; \int d\boldsymbol{r}\,\langle\boldsymbol{r}|\,\hat{o}_1\,|n_1\rangle\,|\boldsymbol{r}, n_2 \ldots n_N\rangle \\
&+\; \int d\boldsymbol{r}\,\langle\boldsymbol{r}|\,\hat{o}_2\,|n_2\rangle\,|n_1, \boldsymbol{r} \ldots n_N\rangle \;+\; \cdots \\
&+\; \int d\boldsymbol{r}\,\langle\boldsymbol{r}|\,\hat{o}_N\,|n_N\rangle\,|n_1, n_2 \ldots \boldsymbol{r}\rangle \\
&=\; \left[\sum_i^N \int d\boldsymbol{r}\,\langle\boldsymbol{r}|\,\hat{o}_i\,|n_i\rangle\,\hat{\psi}^\dagger(\boldsymbol{r}) c_{n_i}\right] |n_1, n_2 \ldots n_N\rangle
\end{aligned} \tag{3.28}$$

By expressing the creation and annihilation operators in terms of the corresponding field operators of eq. (3.17), we find

$$\hat{O} = \int d\boldsymbol{r} d\boldsymbol{r'} \langle \boldsymbol{r} | \hat{o} | \boldsymbol{r'} \rangle \psi^{\dagger}(\boldsymbol{r}) \psi(\boldsymbol{r'}) \ . \tag{3.29}$$

Equations (3.26) and (3.29) provide us with the representation of single-particle operators in the second quantization formalism.

3.2 Green's function formalism

Based on the concepts and notations introduced in Sec. 3.1, I introduce the Green's function formalism and the relevant physical quantities that can be obtained from the Green's functions. In this section, I will focus on the essential aspects and main formulas the present thesis relies on. More details about the formalism can be found in Refs. [167]–[173]. Since we are interested in electron transport and neglect electron-phonon interaction, in what follows we always refer to fermions.

3.2.1 Particle density and current operators

Let us consider the i "site" of the system, which corresponds to the ith state of the orthonormal basis. In our case, this is an orbital-like state of a given atom. The particle density operator $\hat{n}_i$ on site i in terms of the creation and annihilation operators is expressed as in eq. (3.14) by

$$\hat{n}_i \ = \ c_i^{\dagger} c_i \ . \tag{3.30}$$

Accordingly, the operator for the electronic charge on the site i is given by

$$\hat{Q}_i \ = \ (-e) c_i^{\dagger} c_i, \tag{3.31}$$

where $e > 0$ is the absolute value of the electron charge. By making use of the charge continuity equation, the operator $\hat{I}_i$ corresponding to the current outgoing site i is defined by minus the derivative of the charge operator on site i with respect to time

$$\hat{I}_i \ = \ -\frac{\partial \hat{Q}_i}{\partial t} = -\frac{1}{i\hbar}[\hat{Q}_i, \hat{H}]_- \ . \tag{3.32}$$

Let us consider a single-particle Hamiltonian operator as a simple form of eq. (3.26) in the second quantization representation, which is expressed by

$$\hat{H} \ = \ \sum_{mn} t_{mn} c_m^{\dagger} c_n \ , \tag{3.33}$$

where t_{mn} is called hopping energy for $m \neq n$ and on-site energy for $m = n$. Then, by using the anticommutation rules, the current operator of eq. (3.32) can be explicitly written as

$$\begin{aligned}
\hat{I}_i &= \frac{e}{i\hbar}\sum_{mn} t_{mn}[c_i^\dagger c_i c_m^\dagger c_n - c_m^\dagger c_n c_i^\dagger c_i] \\
&= \frac{e}{i\hbar}\sum_{mn} t_{mn}[c_i^\dagger(\delta_{mi} - c_m^\dagger c_i)c_n - c_m^\dagger(\delta_{in} - c_i^\dagger c_n)c_i] \\
&= \frac{e}{i\hbar}\sum_{m} \left(t_{im}c_i^\dagger c_m - t_{mi}c_m^\dagger c_i\right) \ . \qquad (3.34)
\end{aligned}$$

In the above formula, the first term of the summation corresponds to the particle current flow from site m to site i, while the second term corresponds to the particle current flow in the opposite direction, i.e. from site i to site m. Accordingly, the total net current flowing from site i to site m is expressed as

$$\hat{I}_{i\to m} = \frac{e}{i\hbar}(t_{im}c_i^\dagger c_m - t_{mi}c_m^\dagger c_i) \ . \qquad (3.35)$$

The average current is obtained by taking the expectation value of the current operator on the state of the system, which, as we will see later, is related to the lesser Green's function $G^<$ expressed by

$$\left\langle c_\alpha^\dagger c_\beta \right\rangle = \frac{\hbar}{i} G^<_{\beta\alpha}(\tau = 0) \ . \qquad (3.36)$$

In terms of the lesser Green's function, the current is written as

$$\begin{aligned}
I_{im} &= (-e)[t_{im}G^<_{mi}(\tau = 0) - t_{mi}G^<_{im}(\tau = 0)] \\
&= \frac{(-e)}{h}\int_{-\infty}^{\infty} dE[t_{im}G^<_{mi}(E) - t_{mi}G^<_{im}(E)] \\
&= \frac{(-e)}{h}\int_{-\infty}^{\infty} dE\ 2\mathrm{Re}[t_{im}G^<_{mi}(E)] \ , \qquad (3.37)
\end{aligned}$$

where $G^<(E)$ in the latter denotes the equivalent form in the energy domain by the Fourier transform of $G^<(\tau)$. In addition to the current, the Green's functions allow us to obtain physical quantities such as the density of states and the transmission coefficient, as I will detail in Subsec. 3.2.5.

3.2.2 Schrödinger and Heisenberg pictures

Before giving the definition of the Green's functions, it is useful to introduce the Schrödinger and Heisenberg pictures to describe the time-evolution of a quantum mechanical system determined by its Hamiltonian operator $\hat{H}$.

In the *Schrödinger picture*, a state $\left|\Psi^S(t)\right\rangle$ evolves with time according to the Schrödinger equation

$$i\hbar\frac{d}{dt}\left|\Psi^S(t)\right\rangle \;=\; \hat{H}\left|\Psi^S(t)\right\rangle \;. \tag{3.38}$$

When the state at time t_0 is known, its evolution at time t can be written as

$$\left|\Psi^S(t)\right\rangle \;=\; \hat{U}(t,t_0)\left|\Psi^S(t_0)\right\rangle \;, \tag{3.39}$$

where $\hat{U}$ is the time evolution operator, which, for time-independent Hamiltonian operators, is given by

$$\hat{U}(t,t_0) \;=\; e^{-i\hat{H}(t-t_0)/\hbar} \;. \tag{3.40}$$

The *Heisenberg picture*, which is more appropriate for our purposes, shifts the time dependence from states to operators by defining

$$\left|\Psi^H\right\rangle \;\equiv\; \left|\Psi^S(t_0)\right\rangle, \tag{3.41}$$

$$\hat{O}^H(t) \;\equiv\; \hat{U}(t_0,t)\;\hat{O}^S\;\hat{U}(t,t_0) \;. \tag{3.42}$$

Note that, as expected, $\left\langle\Psi^S(t)\middle|O^S|\Psi^S(t)\right\rangle \;=\; \left\langle\Psi^H\middle|O^H(t)|\Psi^H\right\rangle$, i.e. the expectation value of an operator on a given state is the same in the two representations. The evolution of Heisenberg operators is determined by

$$i\hbar\frac{d}{dt}\hat{O}^H(t) \;=\; \left[\hat{O}^H(t),\hat{H}\right]_- \;. \tag{3.43}$$

This equation is only valid for time-independent Schrödinger operators. In what follows, we omit the superscripts "S" and "H" since the chosen picture is evident from the indicated or omitted time dependence. The field operators of eq. (3.42) are expressed in the Heisenberg representation as

$$\hat{\psi}^\dagger(\boldsymbol{r},t) \;=\; e^{i\hat{H}(t-t_0)/\hbar}\hat{\psi}^\dagger(\boldsymbol{r})e^{-i\hat{H}(t-t_0)/\hbar} \quad\text{and}\quad \hat{\psi}(\boldsymbol{r},t) \;=\; e^{i\hat{H}(t-t_0)/\hbar}\hat{\psi}(\boldsymbol{r})e^{-i\hat{H}(t-t_0)/\hbar} \;. \tag{3.44}$$

In addition, the time-dependent creation and annihilation operators in a generic basis are written as

$$c_\alpha^\dagger(t) \;=\; e^{i\hat{H}(t-t_0)/\hbar}\;c_\alpha^\dagger\;e^{-i\hat{H}(t-t_0)/\hbar}, \tag{3.45}$$

$$c_\alpha(t) \;=\; e^{i\hat{H}(t-t_0)/\hbar}\;c_\alpha\;e^{-i\hat{H}(t-t_0)/\hbar} \;. \tag{3.46}$$

If $\{|\alpha\rangle\}$ is the basis of the Hamiltonian eigenstates with eigenvalues $\{E_\alpha\}$, then

$$c_\alpha^\dagger(t) \;=\; e^{iE_\alpha(t-t_0)/\hbar}\;c_\alpha^\dagger(t_0) \quad\text{and}\quad c_\alpha(t) \;=\; e^{-iE_\alpha(t-t_0)/\hbar}\;c_\alpha(t_0) \;. \tag{3.47}$$

3.2.3 Definition of Green's functions

We start by defining the time-ordered Green's function in terms of the creation and annihilation operators in the Heisenberg representation:

$$G_{\alpha\beta}(t,t') \;\equiv\; -\frac{i}{\hbar}\mathrm{Tr}\left[\hat{\rho}\;\hat{T}[c_\alpha(t)c^\dagger_\beta(t')]\right]\;, \tag{3.48}$$

where $\hat{T}$ is the time ordering operator that orders operators according to decreasing time with a minus sign for each permutation (fermions), Tr is the trace operator and $\hat{\rho}$ is the density matrix operator at time t_0. For a system at thermodynamic equilibrium at time t_0 (which we will take as very far in the past), the density matrix operator is

$$\hat{\rho} \;=\; \frac{e^{-(\hat{H}-\mu\hat{N})/(k_\mathrm{B}T)}}{\mathrm{Tr}\left[e^{-(\hat{H}-\mu\hat{N})/(k_\mathrm{B}T)}\right]}\;, \tag{3.49}$$

where T is the temperature, μ is the chemical potential, k_B is the Boltzmann constant and $\hat{N}$ is the number operator introduced in eq. (3.14).

There are other useful Green's functions:

$$G^R_{\alpha\beta}(t,t') \;\equiv\; -\frac{i}{\hbar}\mathrm{Tr}\left[\hat{\rho}\;[c_\alpha(t),c^\dagger_\beta(t')]_+\right]\theta(t-t')\;, \tag{3.50}$$

$$G^A_{\alpha\beta}(t,t') \;\equiv\; \frac{i}{\hbar}\mathrm{Tr}\left[\hat{\rho}\;[c_\alpha(t),c^\dagger_\beta(t')]_+\right]\theta(t'-t)\;, \tag{3.51}$$

$$G^>_{\alpha\beta}(t,t') \;\equiv\; -\frac{i}{\hbar}\mathrm{Tr}\left[\hat{\rho}\;c_\alpha(t)\;c^\dagger_\beta(t')\right]\;, \tag{3.52}$$

$$G^<_{\alpha\beta}(t,t') \;\equiv\; \frac{i}{\hbar}\mathrm{Tr}\left[\hat{\rho}\;c^\dagger_\beta(t')\;c_\alpha(t)\right]\;, \tag{3.53}$$

where θ is the Heaviside step function. G^R, G^A, $G^>$, and $G^<$ are the retarded Green's function, advanced Green's function, greater Green's function, and lesser Green's function, respectively. These functions are related to each other *via* the relation

$$G^R - G^A \;=\; G^> - G^<\;. \tag{3.54}$$

Furthermore, the time-ordered Green's function can be expressed by using lesser and greater Green's functions as

$$G_{\alpha\beta}(t,t') \;=\; G^>_{\alpha\beta}(t,t')\;\theta(t-t') + G^<_{\alpha\beta}(t,t')\;\theta(t'-t)\;. \tag{3.55}$$

In the independent electron approximation, when $\{|\alpha\rangle\}$ is the basis set of the eigenstates of the one-body Hamiltonian, the Green's functions are diagonal and eq. (3.47) allows us to write them as

$$G^R_{\alpha\beta}(t,t') \;=\; -\frac{i}{\hbar}\;e^{-iE_\alpha\tau/\hbar}\;\theta(\tau)\;\delta_{\alpha\beta}\;, \tag{3.56}$$

$$G^A_{\alpha\beta}(t,t') \;=\; \frac{i}{\hbar}\;e^{-iE_\alpha\tau/\hbar}\;\theta(-\tau)\;\delta_{\alpha\beta}\;, \tag{3.57}$$

where $\tau = t - t'$ and E_α is the αth eigenvalue of the Hamiltonian. Note that G^R and G^A do not depend on the state occupation. On the contrary, the greater and lesser Green's functions do depend on the states occupation, i.e. on the density matrix. In fact, it is straightforward to demonstrate that, at thermodynamic equilibrium, they are given by

$$G^{>}_{\alpha\beta}(t,t') = -\frac{i}{\hbar}\, e^{-iE_\alpha\tau/\hbar}\, [1 - f(E_\alpha,\mu,T)]\delta_{\alpha\beta} \tag{3.58}$$

$$G^{<}_{\alpha\beta}(t,t') = \frac{i}{\hbar}\, e^{-iE_\alpha\tau/\hbar}\, f(E_\alpha,\mu,T)\delta_{\alpha\beta}\ , \tag{3.59}$$

where $f(E,\mu,T)$ is the Fermi-Dirac distribution function, μ is the chemical potential of the system and T is the temperature.

Green's function in the energy domain

We have shown that, for time-independent Hamiltonian operators, the Green's functions only depend on the time difference $\tau = t - t'$. This allows us to easily use the Fourier transform to express the Green's function in the energy domain. We define the Fourier transform $F(E)$ in the energy domain of an arbitrary time-dependent function $F(\tau)$ as

$$F(E) \equiv \int d\tau\ e^{iE\tau/\hbar}\, F(\tau) \quad \text{so that} \quad F(\tau) = \frac{1}{h}\int dE\ e^{-iE\tau/\hbar}\, F(E)\ . \tag{3.60}$$

Accordingly, in the independent electron approximation, the (diagonal) retarded Green's function in the basis of the one-body Hamiltonian eigenstates in the energy domain is

$$G^R_{\alpha\alpha}(E) = \int_{-\infty}^{+\infty} d\tau e^{iE\tau/\hbar} G^R_{\alpha\alpha}(\tau) = -\frac{i}{\hbar}\int_0^{+\infty} d\tau e^{i(E-E_\alpha)\tau/\hbar}\ . \tag{3.61}$$

To make this integral convergent, we add a small and positive imaginary part to the energy $E = E + i\epsilon$ with $\epsilon \to 0^+$, and obtain

$$G^R_{\alpha\alpha}(E) = \frac{1}{E + i\epsilon - E_\alpha}\ . \tag{3.62}$$

By passing from the basis of the one-body Hamiltonian eigenstates to a generic basis, we get the matricial form

$$G^R(E) = \frac{1}{E + i\epsilon - H}\ . \tag{3.63}$$

Analogously, the other Green's functions in the energy domain (and at thermodynamic equilibrium) are

$$G^R(E) = \frac{1}{E + i\epsilon - H} , \tag{3.64}$$

$$G^A(E) = \frac{1}{E - i\epsilon - H} , \tag{3.65}$$

$$G^>(E) = [1 - f(E, \mu, T)] \, [G^R(E) - G^A(E)] , \tag{3.66}$$

$$G^<(E) = -f(E, \mu, T) \, [G^R(E) - G^A(E)] . \tag{3.67}$$

These Green's functions are the key ingredients to calculate important physical quantities, as I will detail in Subsec. 3.2.5.

3.2.4 Numerical evaluation of Green's functions

In this subsection, I discuss some useful techniques to efficiently evaluate the Green's functions. Such techniques are implemented in the numerical codes and allow us to deal with systems consisting of hundreds of thousands of orbitals and to calculate physical quantities such as current, transmission coefficient, and density of states.

Dyson equation for the retarded and advanced Green's functions

Let us consider a system described by a single-particle Hamiltonian H. In general, we can split the Hamiltonian into two components

$$H = H_0 + W , \tag{3.68}$$

where H_0 is a simpler one, for which the retarded and advanced Green's functions are known, and the term W can be seen as a not necessarily small perturbation. Then, the retarded Green's function corresponding to the Hamiltonian H can be calculated as

$$\begin{aligned} G^R(E) &= \frac{1}{E + i\epsilon - (H_0 + W)} \\ &= \frac{1}{E + i\epsilon - H_0} \, [E + i\epsilon - (H_0 + W) + W] \, \frac{1}{E + i\epsilon - (H_0 + W)} \\ &= \frac{1}{E + i\epsilon - H_0} + \frac{1}{E + i\epsilon - H_0} \, \frac{W}{E + i\epsilon - (H_0 + W)} \\ &= g^R + g^R W G^R = g^R + G^R W g^R , \end{aligned} \tag{3.69}$$

where g^R is the retarded Green's function corresponding to the Hamiltonian H_0 and G^R is that corresponding to the whole Hamiltonian H. Equation (3.69) is called *Dyson equation*, and it makes the calculation of the Green's function simpler by expressing it in terms of the known Green's function corresponding to the component H_0.

Decimation-renormalization method

The Dyson equation is a powerful tool to calculate the Green's function projected on a subspace of the system by *decimating* (i.e. eliminating) the degrees of freedom corresponding to the complementary subspace, and by incorporating their effect in a *renormalized* energy-dependent Hamiltonian for the subspace we are interested in.

For example, let us consider a Hilbert space and split it into subspaces A and B. We indicate the Hamiltonian operators projected on the two subspaces as H_{AA} and H_{BB} and the coupling between them as H_{AB} and H_{BA}. With reference to the notation of eq. (3.68), we can define $H_0 = H_A \oplus H_B$ and $W = H_{AB} \oplus H_{BA}$, i.e.

$$H \;=\; H_0 \;+\; W \;=\; \begin{pmatrix} H_{AA} & 0 \\ 0 & H_{BB} \end{pmatrix} \;+\; \begin{pmatrix} 0 & H_{AB} \\ H_{BA} & 0 \end{pmatrix} . \tag{3.70}$$

The retarded Green's function corresponding to the uncoupled subspaces can be written as

$$g^R(E) \;=\; \begin{pmatrix} g^R_A(E) & 0 \\ 0 & g^R_B(E) \end{pmatrix} \quad \text{with} \quad g^R_{A/B}(E) \;=\; \frac{1}{E + i\epsilon - H_{AA/BB}} , \tag{3.71}$$

while the retarded Green's function of the complete coupled system is

$$G^R(E) \;=\; \begin{pmatrix} G^R_{AA}(E) & G^R_{AB}(E) \\ G^R_{BA}(E) & G^R_{BB}(E) \end{pmatrix} . \tag{3.72}$$

From eq. (3.69), we obtain

$$\begin{cases} G^R_{AA}(E) &=& g^R_A(E) \;+\; g^R_A(E)\; H_{AB}\; G^R_{BA} \\ G^R_{AB}(E) &=& g^R_A(E)\; H_{AB}\; G^R_{BB} \\ G^R_{BA}(E) &=& g^R_B(E)\; H_{BA}\; G^R_{AA} \\ G^R_{BB}(E) &=& g^R_B(E) \;+\; g^R_B(E)\; H_{BA}\; G^R_{AB} \end{cases} \tag{3.73}$$

If, for example, we are interested in calculating the retarded Green's function projected on subspace A, we can combine the first and the third lines of the

previous equation and obtain

$$\begin{aligned} G^R_{AA}(E) &= g^R_A(E) \;+\; g^R_A(E)\; H_{AB}\; g^R_B(E)\; H_{BA}\; G^R_{AA}(E) \\ &= \Big[\big(g^R_A(E)\big)^{-1} \;-\; H_{AB}\; g^R_B(E)\; H_{BA}\Big]^{-1} \\ &= \big[E + i\epsilon \;-\; H_{AA} \;-\; \Sigma^R(E)\big]^{-1} \\ &= \left[E + i\epsilon - H_{\text{eff}}(E)\right]^{-1} \;. \end{aligned} \tag{3.74}$$

This relation indicates that the Green's function projected on subspace A can be interpreted as that corresponding to the effective *renormalized* Hamiltonian $H_{\text{eff}}(E) \equiv H_A + \Sigma^R(E)$, where the retarded self-energy

$$\Sigma^R(E) \;\equiv\; H_{AB}\; g^R_B(E)\; H_{BA} \;=\; H_{AB}\; \frac{1}{E + i\epsilon - H_{BB}}\; H_{BA} \tag{3.75}$$

accounts for the coupling with subspace B. It is important to note that the effective Hamiltonian does depend on the energy E, and that it has the same size of the subspace A. Accordingly, we can say that the degrees of freedom corresponding to subspace B are *decimated* into the self-energies and the Hamiltonian of the subspace A is renormalized to H_{eff}.

Renormalization method for a system between two contacts

The typical configuration that we consider for the simulation of electron transport consists of a central system (C) connected to two semi-infinite leads on the left side (L) and on right side (R) as electron reservoirs, see Fig. 3.1. With reference to the Dyson equation illustrated above, we consider the Hamiltonian H_0 corresponding to the three uncoupled regions, and the term W as the

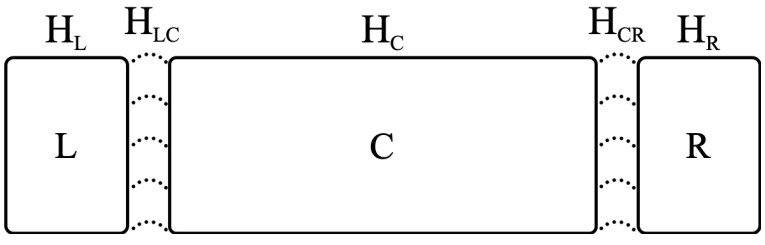

Figure 3.1: Scheme of the system that consists of three parts, a central system (C) and two semi-infinite leads on the left (L) and on the right (R). H_i for $i = L, R, C$ is the Hamiltonian of each uncoupled region. $H_{i,j}$ for $i \neq j$ is the coupling term between neighboring regions, region i and region j.

couplings between neighboring regions:

$$H = \begin{pmatrix} H_L & 0 & 0 \\ 0 & H_C & 0 \\ 0 & 0 & H_R \end{pmatrix} + \begin{pmatrix} 0 & H_{LC} & 0 \\ H_{CL} & 0 & H_{CR} \\ 0 & H_{RC} & 0 \end{pmatrix} = H_0 + W \,. \quad (3.76)$$

The hermiticity of the Hamiltonian operator implies $H_{LC} = H_{CL}^\dagger$ and $H_{RC} = H_{CR}^\dagger$. The infinite size of H_R and H_L can be treated by using the periodicity of the semi-infinite leads, as I will discuss later.

The retarded Green's functions corresponding to the uncoupled system g^R and to the whole system G^R are expressed by

$$g^R = \begin{pmatrix} g_L^R & 0 & 0 \\ 0 & g_C^R & 0 \\ 0 & 0 & g_R^R \end{pmatrix} \quad \text{and} \quad G^R = \begin{pmatrix} G_L^R & G_{LC}^R & G_{LR}^R \\ G_{CL}^R & G_C^R & G_{CR}^R \\ G_{RL}^R & G_{RC}^R & G_R^R \end{pmatrix} \,. \quad (3.77)$$

Among the different components of G^R, what we are interested in is the Green's function projected on the central region, G_C^R. According to the Dyson equation of eq. (3.69) and eq. (3.75)

$$G_C^R = g_C^R + g_C^R \, \Sigma_L \, G_C^R + g_C^R \, \Sigma_R \, G_C^R \,, \quad (3.78)$$

where Σ_L and Σ_R are the *self-energies* of the left and right contacts, respectively, and are defined as

$$\Sigma_L^R \equiv H_{CL} \, g_L^R(E) \, H_{LC} \quad \text{and} \quad \Sigma_R^R \equiv H_{CR} \, g_R^R(E) \, H_{RC} \,. \quad (3.79)$$

The retarded Green's function is then calculated as

$$G_C^R(E) = \frac{1}{E + i\epsilon - H_C - \Sigma_L^R(E) - \Sigma_R^R(E)} \,. \quad (3.80)$$

Therefore, provided we can calculate retarded self-energies Σ_L^R and Σ_R^R, the problem is reduced from the inversion of an infinite matrix to the inversion of a finite matrix with size equal to the number of degree of freedom (or orbitals) of the central region.

Renormalization of a periodic semi-infinite contact

In order to obtain the Green's function of the central region by using eq. (3.80), we need to calculate the self-energies of the semi-infinite contacts. In eq. (3.79), the matrix size of the Green's function for each isolated contact, g_L^R and g_R^R, is equal to the size of the corresponding lead Hamiltonian, i.e. it is infinite. However, since the coupling W only operates between the central region and the surface regions of the leads (i.e. those that are closer to the central region), we just need to calculate the Green's functions on these surface regions. This can

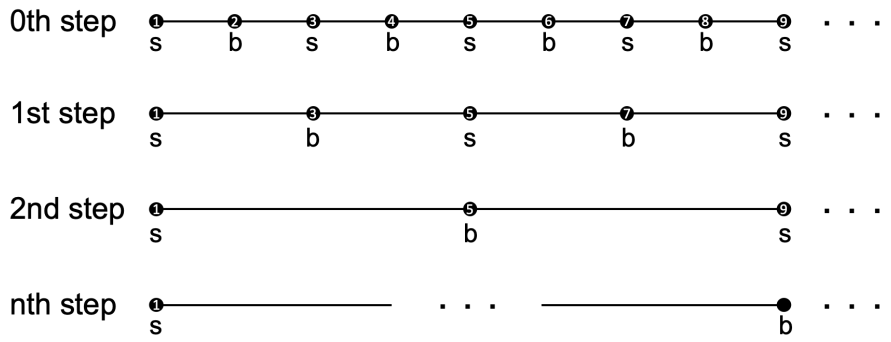

Figure 3.2: Schematic diagram of the procedure for the renormalization of a periodic and semi-infinite system. Surface (s) and bulk (b) denote odd and even index of sites from left, respectively.

be done by exploiting the periodicity of the leads and thanks to an algorithm based on the Dyson equation and developed by M. P. Lopez Sancho et al. in Ref. [174], also called Sancho-Rubio algorithm. For simplicity, we represent a lead as a semi-infinite series of points, see Fig. 3.2, where each point corresponds to a primitive cell of the lead. We assume that the Hamiltonian only couples neighbor cells. The first cell with index 1 is the surface cell, for which we are interested in calculating the Green's function. Due to the periodicity, the Hamiltonian is the same for each cell, as well as the coupling Hamiltonian between neighbor cells. We indicate the cells with odd index with the letter "s", which stands for "surface", as is the case of cell 1, and those with even index with the letter "b", which stands for "bulk". In order to obtain the renormalized surface Hamiltonian and then the Green's function on cell 1, all the bulk points are decimated at once in each step until the coupling between the leftmost point and the neighbor becomes negligible. Note that a small imaginary part in the energy is necessary to make the calculation of Green's functions converged. With reference to the decimation-renormalization technique illustrated above, we consider as H_0 the Hamiltonian of all the cells uncoupled. More specifically, we consider as subspace A all the cells with odd index, i.e. those labeled by the letter "s", and as subspace B the remaining cells with even index, i.e. those labeled by the letter "b". At the initial step, the cell-Hamiltonian h is the same for each cell, and the coupling Hamiltonian between neighboring cells is set to the coupling Hamiltonians w_{sb} and w_{bs} between cells. At each step we decimate all the cells with even index, which all have the same renormalized Hamiltonian and thus just require the inversion of a single matrix with size equal to the number of orbitals within each cell. After N steps, 2^{N-1} cells are decimated and the renormalized coupling between the cells will vanish. This allows us to finally consider the first surface cell as isolated and to calculate the corresponding Green's function. To be more specific, the decimation-renormalization procedure is summarized

as follows:

$$
\begin{aligned}
0\text{th step} \;:\; & h_s^{(0)} = h_0,\; h_b^{(0)} = h_0,\; w_{sb}^{(0)} = w_{sb},\; w_{bs}^{(0)} = w_{bs},\; g_b^{(0)} = \frac{1}{E - h_b} \\
n\text{th step} \;:\; & h_s^{(n)} = h_s^{(n-1)} + w_{sb}^{(n-1)} g_b^{(n-1)} w_{bs}^{(n-1)}, \\
& h_b^{(n)} = h_b^{(n-1)} + w_{sb}^{(n-1)} g_b^{(n-1)} w_{bs}^{(n-1)} + w_{bs}^{(n-1)} g_b^{(n-1)} w_{sb}^{(n-1)}, \\
& w_{sb}^{(n)} = w_{sb}^{(n-1)} g_b^{(n-1)} w_{sb}^{(n-1)}, \\
& w_{bs}^{(n)} = w_{bs}^{(n-1)} g_b^{(n-1)} w_{bs}^{(n-1)}, \\
& g_b^{(n)} = \frac{1}{E - h_b^{(n)}} \\
N\text{th step} \;:\; & w_{sb}^{(N)} \approx \mathbf{0} \;\rightarrow\; G_s = \frac{1}{E - h_s^{(N)}} \;,
\end{aligned}
\tag{3.81}
$$

where the superscript indicates the number of steps and we dropped the label R to indicate the retarded Green's function. When all components of the coupling term w_{sb}^N in the Nth step are close to zero, we can finally obtain the renormalized Hamiltonian of the leftmost point and thus its Green's function G_s. This procedure allows us to efficiently calculate the Green's function of periodic and semi-infinite contacts, which are used to obtain the corresponding self-energies.

Renormalization of a layered system

The tight-binding Hamiltonians considered in this manuscript typically limit the coupling between few nearest neighbor orbitals. This has the important advantage of allowing to partition the system under investigation in a set of layers, each containing a certain number of orbitals, such that the Hamiltonian only couples first neighbor layers, see Fig. 3.3. Let us imagine to have M layers, numbered from 1 to M. We indicate by H_{mm} the Hamiltonian projected on layer m, and by $H_{m,m+1}$ and $H_{m,m-1}$ the coupling with its neighbor layers. If we are interested in the retarded Green's function on a specific layer, say n, then we can proceed by decimating the other layers one-by-one, so to have to invert, at each step, matrices with same size as the layer Hamiltonian. To be more specific, we start by decimating layer 1 and renormalize accordingly the Hamiltonian of layer 2

$$
\Sigma_{(L)}^R(E) \;=\; H_{21}\; \left[E + i\epsilon - H_{11}\right]^{-1}\; H_{12} \;, \tag{3.82}
$$

where the label "L" indicates that we are renormalizing from the left. We continue with the same procedure by calculating

$$
\Sigma_{(L)}^R(E) \;=\; H_{m,m-1}\; \left[E + i\epsilon - H_{m-1,m-1} - \Sigma_{(L)}^R(E)\right]^{-1}\; H_{m-1,m} \;, \tag{3.83}
$$

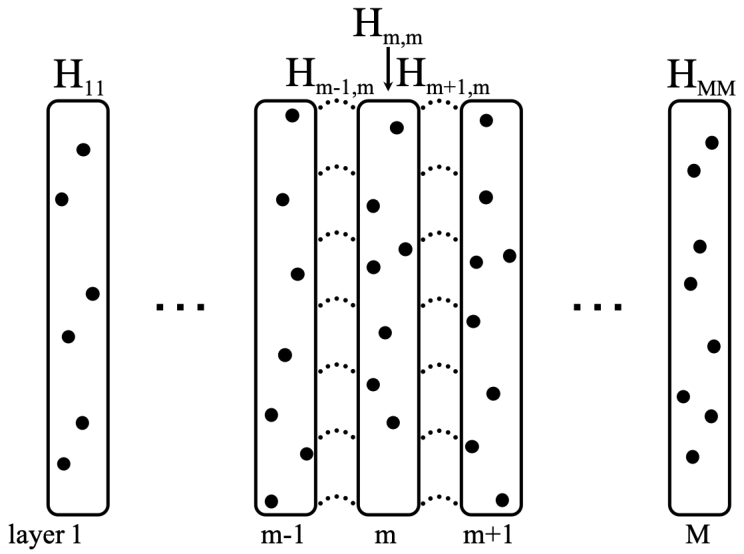

Figure 3.3: Scheme of the layered system with M layers. Each layer is a set of orbitals and it is coupled only with its neighbor layers.

up to $m = n$. We then start the decimation from the right side by

$$\Sigma^R_{(R)}(E) \;=\; H_{m,m+1}\,\left[E + i\epsilon - H_{m+1,m+1} - \Sigma^R_{(R)}(E)\right]^{-1}\,H_{m+1,m}\;, \qquad (3.84)$$

from $m = M - 1$ down to $m = n$. The label "R" indicates that we are renormalizing from the left. We can finally obtain the retarded Green's function on layer n by calculating

$$G^R_{nn} \;=\; \frac{1}{E + i\epsilon - H_{n,n} - \Sigma^L_{(R)}(E) - \Sigma^R_{(R)}(E)}\;. \qquad (3.85)$$

This technique, implemented in the codes, is very powerful, because it allows us to treat very large systems without inverting huge matrices.

Keldysh theory

As discussed in Subsec. 3.2.1, the lesser Green's function is necessary in order to calculate the current flowing through the system. For systems out of thermodynamic equilibrium, however, obtaining the lesser Green's function is more complicated, since, contrary to the retarded Green's function, it contains information about the occupation of the states. Thanks to the Keldysh theory [175], the lesser Green's function of the system out of equilibrium can be expressed in terms of the Green's functions for the system at equilibrium. We do not illustrate the quite lengthy derivation of the theory [165], which is based on the Feynman diagrammatic expansion of the time evolution operator, but just the main result, which is the analogous of the Dyson equation

for out-of-equilibrium Green's functions. Note that, for the following derivation, I limit to the non-interacting case, i.e. there is no electron-phonon and electron-electron interaction.

We consider an (out-of-equilibrium) system with Hamiltonian $H = H_0 + W$, where H_0 is the Hamiltonian for uncoupled subsystems and W is the coupling term between them. In the absence of W, each subsystem would be isolated and then individually at thermodynamic equilibrium. Therefore, we know how to calculate the corresponding lesser Green's functions, see eq. (3.67). For example, H_0 may correspond to the uncoupled leads and central region, where clearly the leads would be at equilibrium with the contacts at given temperature and chemical potential. We can thus easily define the density matrix in terms of eq. (3.49) and obtain the lesser Green's functions as illustrated below. The presence of W, in our example the coupling between the central region and the leads, drives the system out of equilibrium and makes the current flow through the system. We consider that W is adiabatically switched on from the time t_0 ($\rightarrow -\infty$) to the time t. In the Keldysh formalism, the kinetic equation for the lesser Green's function in the energy domain reads

$$G^< \;=\; g^< \;+\; G^R\, W\, g^< \;+\; G^<\, W\, g^A \;, \tag{3.86}$$

or equivalently as

$$G^< \;=\; (1 + G^R\, W)\; g^<\; (1 + W\; G^A) \;, \tag{3.87}$$

where G and g denote Green's functions for the whole system described by H and the uncoupled system described by H_0, respectively.

For the left-central-right region scheme of system we consider here, $g^<$ is the sum of the lesser Green's functions for each region, $g_L^<$, $g_C^<$, and $g_R^<$. The lesser Green's function of each region can be calculated as $g_i^< = -f_i(g_i^R - g_i^A)$ for $i = L, C, R$, since each of them is at equilibrium. Then, the lesser Green's function projected on the central region that we are interested in is expressed as

$$G^< \;=\; G^R\,(\Sigma_L^< \;+\; \Sigma_R^<)\; G^A \;=\; i f_L\; G^R\, \Gamma_L\; G^A \;+\; i f_R\; G^R\, \Gamma_R G^A \;, \tag{3.88}$$

where

$$\Sigma_L^< \;=\; -f_L(\Sigma_L^R - \Sigma_L^A) \;=\; i f_L\; \Gamma_L \tag{3.89}$$

$$\Sigma_R^< \;=\; -f_R(\Sigma_R^R - \Sigma_R^A) \;=\; i f_R\; \Gamma_R \;, \tag{3.90}$$

and $\Gamma_{L/R}$ are called rate operators. The Fermi-Dirac occupation function $f_{L/R}(E)$ stands for

$$f_L(E) \;=\; f(E, \mu_L, T_L) \qquad \text{and} \qquad f_R(E) \;=\; f(E, \mu_R, T_R) \;, \tag{3.91}$$

where μ_L and T_L are the chemical potential and the temperature of the left contact and μ_R and T_R are the chemical potential and the temperature of the

right contact. Note that the equilibrium μ_C and T_C for the central region are not important, because due to the finite size of the central region its initial equilibrium (or non-equilibrium) state does not affect the final state after the connection of the infinite leads.

Some useful identities can be derived from these equations. For the Green's functions projected on the central region, we obtain

$$G^R \; - \; G^A \; = \; -i \; G^R \; [\Gamma_L \; + \; \Gamma_R] \; G^A \; , \tag{3.92}$$

which is a by-product of eq. (3.88) for $f_L = f_R$.

3.2.5 Formulas for the density of states and the charge current

Density of states

Let us consider a complete orthonormal basis of eigenstates of the Hamiltonian $\{|\alpha\rangle\}$ with the corresponding eigenvalues $\{E_\alpha\}$. For the diagonal Hamiltonian, the operator form of the retarded Green's function of eq. (3.64) can be expressed as

$$G^R(E) \; = \; \sum_\alpha \frac{|\alpha\rangle \, \langle\alpha|}{E + i\epsilon - E_\alpha} \; . \tag{3.93}$$

Then, the Green's function in the real-space representation is written as

$$G^R(\boldsymbol{r}, \boldsymbol{r'}; E) \; = \; \sum_\alpha \frac{u_\alpha(\boldsymbol{r}) u_\alpha^*(\boldsymbol{r'})}{E + i\epsilon - E_\alpha} \; . \tag{3.94}$$

The summation contains terms of the type $f(x) = 1/(x + i\epsilon)$, which, if decomposed into its real and imaginary parts, gives

$$f(x) \; = \; \frac{x}{x^2 + \epsilon^2} \; - \; i \; \frac{\epsilon}{x^2 + \epsilon^2} \; . \tag{3.95}$$

The imaginary part is a Lorentzian function, which becomes $-\pi\delta(x)$ in the limit $\epsilon \to 0^+$. Then, the local density of states $\rho(\boldsymbol{r}, E)$ is obtained from the imaginary part of the retarded Green's function as

$$\rho(\boldsymbol{r}, E) = -\frac{1}{\pi} \mathrm{Im}\{G^R(\boldsymbol{r}, \boldsymbol{r}; E)\} = \sum_\alpha |u_\alpha(\boldsymbol{r})|^2 \delta(E - E_\alpha) \; . \tag{3.96}$$

Analogously, the density of states projected on the state $|\alpha\rangle$ is given by

$$\rho_\alpha(E) \; = \; -\frac{1}{\pi} \mathrm{Im}\{G^R_{\alpha\alpha}(E)\} \; = \; \delta(E - E_\alpha) \; . \tag{3.97}$$

The total density of states $\rho(E)$ is obtained by summing over the different orbitals (which corresponds to performing the trace) or by integrating in real space:

$$\rho(E) \;=\; -\frac{1}{\pi}\mathrm{Im}\{\mathrm{Tr}[G^R(E)]\} \;=\; -\frac{1}{\pi}\mathrm{Im}\left[\int d\boldsymbol{r} G^R(\boldsymbol{r},\boldsymbol{r};E)\right] \;=\; \sum_\alpha \delta(E-E_\alpha)\;, \tag{3.98}$$

where Tr is the trace operator.

Charge current

Let us consider that the central region of our system extends from layer 1 to layer M, see Fig. 3.4. Each layer is only coupled to the two neighbor ones. Using eq. (3.37), the current from site (or orbital) i of layer 0 to site j of layer 1 can be written as

$$I_{0i,1j} \;=\; \frac{-e}{h}\int_{-\infty}^{+\infty} dE\; 2\mathrm{Re}[t_{0i,1j}G^<_{1j,0i}(E)]\;. \tag{3.99}$$

In order to calculate the current, we have to evaluate the matrix elements of the Green's function. According to the kinetic equation of eq. (3.86) where W is the coupling between layer 0 and 1 and between layer M and $M+1$, the current is

$$I_{0i,1j} \;=\; \frac{-e}{h}\int_{-\infty}^{+\infty} dE\; 2\mathrm{Re}\left[t_{0i,1j}\sum_{kl}\left[G^R_{1j,1k}(E)\; t_{1k,0l}\; g^<_{0l,0i} + G^<_{1j,1k}(E)\; t_{1k,0l}\; g^A_{0l,0i}\right]\right]\;. \tag{3.100}$$

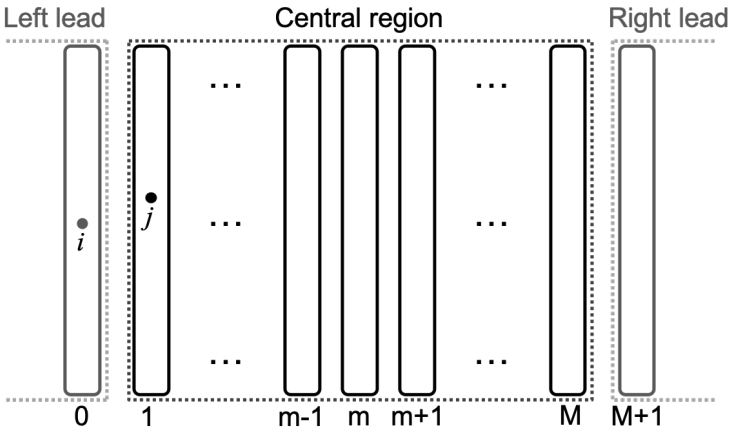

Figure 3.4: Scheme of the system with a central region, from layer 1 to layer M, connected with two semi-infinite leads on the left side and right side.

The total current is given by the sum of all the local currents from layer 0 to layer 1

$$\begin{aligned} I &= \sum_{ij} I_{0i,1j} \\ &= \frac{-e}{h}\int_{-\infty}^{+\infty} dE\ 2\ \mathrm{Re}\sum_{ijkl}\left[G^R_{1j,1k}(E)\ t_{1k,0l}\ g^<_{0l,0i}\ t_{0i,1j} + G^<_{1j,1k}(E)\ t_{1k,0l}\ g^A_{0l,0i}\ t_{0i,1j}\right] \\ &= \frac{-e}{h}\int_{-\infty}^{+\infty} dE\ 2\ \mathrm{Re}\sum_{ijk}\left[G^R_{1j,1k}(E)\ \Sigma^<_{1k,1j(L)}\ + G^<_{1j,1k}(E)\ \Sigma^A_{1k,1j(L)}\ \right] \\ &= \frac{-e}{h}\int_{-\infty}^{+\infty} dE\ 2\ \mathrm{Re}\ \mathrm{Tr}\left[G^R_{11}(E)\ \Sigma^<_{11(L)}\ + G^<_{11}(E)\ \Sigma^A_{11(L)}\ \right]\ . \end{aligned} \tag{3.101}$$

When we substitute the lesser Green's function of the central region with the expression in eq. (3.88), we finally obtain

$$\begin{aligned} I = \frac{e}{h}\int dE\ \ 2\mathrm{Re}\ \mathrm{Tr}\Big[& f_L(G^R_{11}\Sigma^R_{11(L)} - G^R_{11}\Sigma^A_{11(L)} - iG^R_{11}\Gamma_{11(L)}G^A_{11}\Sigma^A_{11(L)}) \\ & -if_R G^R_{1M}\Gamma_{MM(R)}G^A_{M1}\Sigma^A_{11(L)}\ \Big]\ . \end{aligned} \tag{3.102}$$

If now we substitute the third term of the right-hand side with the expression in eq. (3.105), the terms multiplying f_L become

$$\begin{aligned} & G^R_{11}\Sigma^R_{11(L)} - G^R_{11}\Sigma^A_{11(L)} - iG^R_{11}\Gamma_{11(L)}G^A_{11}\Sigma^A_{11(L)} \\ & \quad = G^R_{11}\Sigma^R_{11(L)} - G^A_{11}\Sigma^A_{11(L)} + iG^R_{1M}\Gamma_{MM(R)}G^A_{M1}\Sigma^A_{11(L)}\ . \end{aligned} \tag{3.103}$$

Note that

$$\mathrm{Re}\ \mathrm{Tr}\left[\ G^R_{11}\Sigma^R_{11(L)} - G^A_{11}\Sigma^A_{11(L)}\right]\ =\ 0 \tag{3.104}$$

according to the relation of $2\mathrm{Re}[\mathrm{Tr}[AB]] = \mathrm{Tr}[AB + (AB)^\dagger]$ for any couple of matrices A and B, and to the invariance under cyclic permutation of trace operator. Then, the first two terms of eq. (3.103) are cancelled. Moreover, we can demonstrate that $G^R_{1M}\Gamma_{MM(R)}G^A_{M1}\Sigma^A_{11(L)} = G^R_{11}\Gamma_{11(R)}G^A_{11}\Sigma^A_{11(L)}$. In fact, eq. (3.92) specified to the sites of layers 1 and M becomes

$$G^R_{11}\ -\ G^A_{11}\ =\ -iG^R_{11}\ \Gamma_{11(L)}G^A_{11}\ -\ iG^R_{1M}\ \Gamma_{MM(R)}\ G^A_{M1}\ , \tag{3.105}$$

and since we can arbitrarily choose the number of layers to include in the central region by shifting them between the leads and the central region, we can consider that the latter extends from layer 1 to layer M' ($M' \geq 1; M' \neq M$). By comparison with eq. (3.105), we get

$$G^R_{1M'}\ \Gamma_{M'M'(R)}\ G^A_{M'1}\ =\ G^R_{1M}\ \Gamma_{MM(R)}\ G^A_{M1}\ . \tag{3.106}$$

This equation allows us to substitute $G^R_{1M}\Gamma_{MM(R)}G^A_{M1}$ with $G^R_{11}\Gamma_{11(R)}G^A_{11}$, which makes the calculation simpler by restricting it on the first layer of the central region. Therefore, by using eq. (3.106), we get

$$\begin{aligned} I &= \frac{e}{h}\int dE\ 2(f_L - f_R)\mathrm{Re}\left[\ iG^R_{11}\Gamma_{11(R)}G^A_{11}\Sigma_{11(L)}\ \right] \\ &= \frac{e}{h}\int dE\ (f_L - f_R)\ \mathrm{Tr}\left[G^R_{11}\Gamma_{11(R)}G^A_{11}\Gamma_{11(L)}\right]\ , \end{aligned} \tag{3.107}$$

where the second line is obtained, in the same way as eq. (3.104), by considering that $\Gamma_{(L,R)} = i(\Sigma^A_{(L,R)} - \Sigma^A_{(L,R)})$. Equation (3.107) is exactly the same formula obtained in the framework of the Landauer-Büttiker formalism [176] where the transmission coefficient is $T(E) = \mathrm{Tr}[G^R\Gamma_{(R)}G^A\Gamma_{(L)}]$.

To be more quantitative, the room-temperature differential conductance $G(\mu)$ as a function of the chemical potential μ can be calculated in terms of $T(E)$,

$$G(\mu) = \frac{e^2}{h}\ \frac{1}{4k_\mathrm{B}\tau}\int\ dE\ \cosh^{-2}\left(\frac{E-\mu}{2k_\mathrm{B}\tau}\right)\ T(E)\ , \tag{3.108}$$

where k_B is the Boltzmann constant, and τ is the temperature.

3.3 Transport regimes

In this section, we summarize the main properties of the diffusive and localized transport regimes, which emerge in initially ballistic conductors when disorder is present. Indeed, from a semi-classical point of view, in a disordered system, electrons diffuse in zigzag motion by bouncing between impurities, where the distance traveled between two scattering events (the mean free path ℓ) decreases for increasing impurity density. In quasi-1D disordered system, as is the case of TMD ribbons considered in this manuscript, the transport regime is ballistic when the mean free path is larger than the system size, quasi-ballistic when it is longer than the system width but shorter then the system length (from contact to contact), and diffusive when it is smaller than the system size, see Fig. 3.5.

For strong disorder, the diffusion of electrons is highly affected and the system enters the localized transport regime, with a significant suppression of the conductance. Such a phenomenon, predicted in 1958 by P. W. Anderson [178], can indeed be explained in the frame of quantum mechanics, which takes into account the wave nature of the particles. The idea is that, in the presence of disorder and due to wave interference, a wave packet concentrated at a given time at a given point in a 1D or 2D system, cannot spread beyond a certain distance, i.e. it localizes in a finite spatial region, which can be

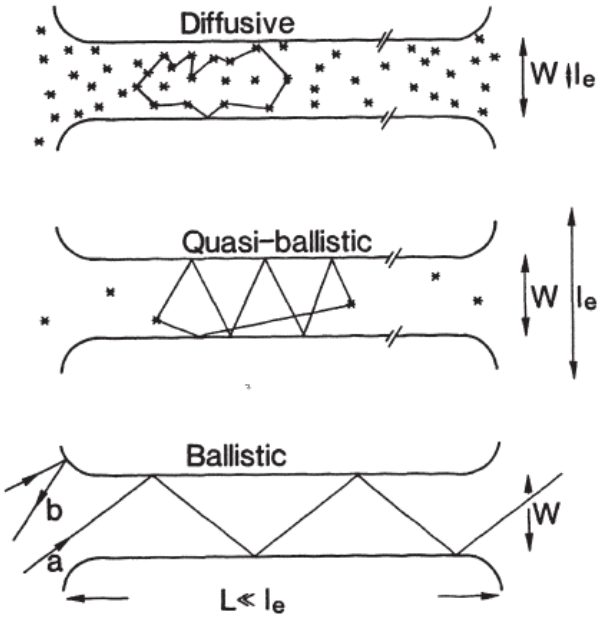

Figure 3.5: Different transport regimes from ballistic to diffusive depending on the length of the mean free path (l_e in the figure) with respect to the length L and the width W of the conductor. The quasi-ballistic and diffusive regimes allow closed electron paths and, by virtue of wave nature of the electrons, the observation of quantum phenomena as weak localization, which are not considered in this thesis. Reprint from Ref. [177]. © Springer-Verlag Berlin Heidelberg 1988.

(much) smaller than the system itself if disorder is strong enough. The localization scaling theory outlined in this section aims to analyze statistically the scaling of the conductance in the presence of disorders. What follows is a brief summary of the important aspects and quantitative analysis detailed in Ref. [179].

The focus of the statistical analysis of Ref. [179] is on chemically-disordered carbon nanotubes, where impurities are randomly distributed over a tube section with length L. Figure 3.6 shows the curves of relative fluctuations $\Delta T/\langle T\rangle$ and $|\Delta \ln T/\langle \ln T\rangle|$ as a function of L, where T is the transmission coefficient at a chosen reference electron energy, ΔT is the standard deviation of T calculated over a large ensemble of different disorder configurations, $\langle T\rangle$ is the average of T, $\Delta \ln T$ is the standard deviation of the logarithm of T and $\langle \ln T\rangle$ is its average. While $\Delta T/\langle T\rangle$ increases for increasing L, $|\Delta \ln T/\langle \ln T\rangle|$ first increases and reaches a peak near $L = \ell$, and then decreases, see Fig. 3.6. These curves suggest a criterion to discriminate between the transport regimes : the system remains in the quasi-ballistic or diffusive transport regime as long as $\Delta T/\langle T\rangle < 1$ and enters the localized regime when $\Delta T/\langle T\rangle > 1$ and $|\Delta \ln T/\langle \ln T\rangle| < 1$. Where the two fluctuation curves cross, at $L = L_c$, the resistance of the nanotube is of the order of the quantum resistance, thus

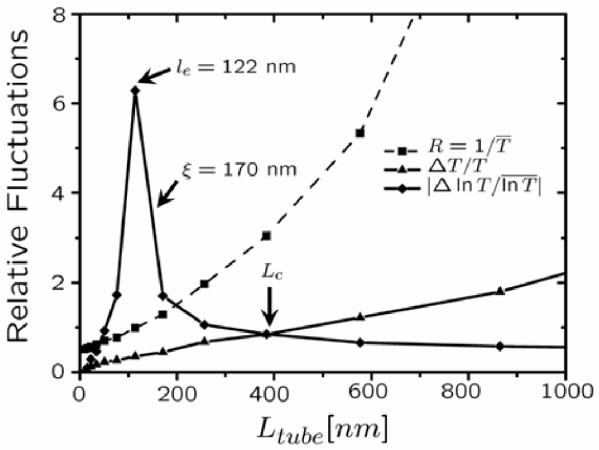

Figure 3.6: Relative fluctuations $\Delta T/\overline{T}$ and $|\Delta \ln T/\overline{\ln T}|$ at $E = 0.35$ eV for a (10,10) nanotube with 0.1% nitrogen doping as a function of the tube length L (continuous lines). ΔT ($\Delta \ln T$) is the standard deviation of T ($\ln T$) and $\overline{T}$ ($\overline{\ln T}$) is the average of T ($\ln T$) over an ensemble of disorder realizations. The curve of $R = 1/\overline{T}$ as a function of L (dashed line). ℓ_e and ξ denote a mean free path and a localization length, respectively. In the present thesis notation, we indicate $\overline{T}$ by $\langle T\rangle$, $\overline{\ln T}$ by$\langle \ln T\rangle$ and ℓ_e by ℓ. Reprint from Ref. [179]. Copyright (2007) World Scientific Pub Co Pte Lt.

indicating the localized transport regime, which is consistent with the argument of Thouless [180]. Thouless proposed that the normalized conductance is related to the ratio of two energy scaling as $G/G_0 \approx E_{th}/\Delta$, where G is the conductance, $G_0 = e^2/h$ is conductance quantum, $E_{th} = \hbar D/L^2$ denotes the Thouless energy related to the time for a wave packet to diffuse to the boundaries of the system and Δ is the mean energy level spacing in the system of size L. When $E_{th} \approx \Delta$ and the conductance is smaller than the quantum conductance, the localization takes place [180].

The transition of the transport regime from ballistic, to diffusive and then to localized can be statistically analyzed by considering the frequency distribution of the transmission coefficient over an ensemble of disorder realizations. When $\Delta T/\langle T\rangle < 1$ and the frequency distribution of T is very narrow with a maximum close to its ballistic value N, where N is the number of active modes in the system at the considered electron energy E, the transport regime of the system is quasi-ballistic. When L increases, as long as $\Delta T/\langle T\rangle < 1$, the frequency distribution becomes more symmetric, as a Gaussian distribution, which indicates the diffusive transport regime. In this regime, the transmission decreases progressively for increasing L, and it is characterized by a mean

free path ℓ such that

$$\langle T\rangle \;=\; \frac{N}{1+L/\ell} \quad\rightarrow\quad R \;=\frac{h}{2e^2}\,\frac{1}{\langle T\rangle} \;=\; \frac{h}{2e^2}\frac{1}{N} \;+\; \frac{h}{2e^2}\frac{L}{N\ell} \;\equiv\; R_{\rm co} \;+\; R_{\rm ch}\;. \tag{3.109}$$

In eq. (3.109), we split the zero-temperature average resistance R in terms of the contact resistance $R_{\rm co}$ and channel resistance $R_{\rm ch}$ components. According to this equation, the transmission is expected to be close to N for $L \ll \ell$, which indicates the quasi-ballistic regime. For larger L of the order of the mean free path, the system enters the diffusive regime, where it stays as long as $\Delta T/\langle T\rangle < 1$.

For even larger L, the transmission decreases exponentially, thus indicating that the system has entered the localized regime. Furthermore, a strongly asymmetric frequency distribution of T with a peak close to zero with $\Delta T/\langle T\rangle > 1$ emerges. At the same time, the distribution of the transmission coefficient logarithm $\ln T$ exhibits a Gaussian shape with $|\Delta \ln T/\langle \ln T\rangle| < 1$. In this regime, the average logarithm of the transmission coefficient scales as

$$\langle \ln T\rangle \propto -L/\xi\;, \tag{3.110}$$

where ξ is the localization length. The detailed fitting of the length scaling, ℓ and ξ, for the disordered systems considered in this thesis, is presented in Sec. 5.2 and Sec. 6.2.

3.4 Summary

In this Chapter, I presented the theoretical framework of the present thesis, which is the Green's function formalism. After introducing the second quantization formalism, and in particular the creation and annihilation operators, in Sec. 3.1.1, we defined the local charge operator and, by means of the charge continuity equation, the current operator. The expectation values of these operators were then expressed in terms of the Green's function, defined in Sec. 3.2. The retarded and advanced Green's functions contain information about the electronic structure, while the lesser and greater Green's function contain information about the statistics of the system, and therefore on the thermal equilibrium or out-of-equilibrium condition. To allow their efficient numerical evaluation, we introduced the decimation-renormalization method of the periodic semi-infinite contact and layered system. This approach permits us to evaluate the retarded and advanced Green's functions projected on the subsystem of interest and to reduce the number of degrees of freedom. Analogously, we illustrated how the Keldysh theory provides us with kinetic equations to obtain the out-of-equilibrium lesser and greater Green's functions in terms of those calculated at thermal equilibrium. This result is particularly important, because electron transport is a non-equilibrium phenomenon,

which occurs when the chemical potentials of the contacts are different. At the end of Sec. 3.2, we derived the formulas of physical quantities such as density of states, current, and transmission coefficient in terms of the Green's functions. These formulas are those implemented in the numerical code and used to obtain all the results presented in Chapter 5 and 6. Lastly, in Sec. 3.3, we discussed how (elastic) quantum transport can be classified in the ballistic, quasi-ballistic, diffusive and localized regimes. The scaling theory here summarized will be used to analyze the impact of various disorders on the transport properties of MoS_2 in Chapter 5 and 6.

Chapter 4

Structure and implementation of the numerical code

The numerical codes are written in both Fortran language and Matlab software and run on a multi-processor server operating under the Linux operating system. I made use of Matlab software for the graphic visualization of all the results presented in the following Chapters. In Sec. 4.1, I will briefly introduce the structure and procedure of the codes with a simple flowchart. Section 4.2 details the implementation of the TB Hamiltonian, which represents a significant and essential part of my thesis work. In particular, the choice of SK TB method for TMD materials allowed us to investigate the impact of various disorders with atomistic precision, and thus its numerical implementation is an important aspect.

4.1 General structure of the codes

The main code developed for the transport simulations consists of separate subroutines, each assigned to a specific task such as the evaluation of self-energies for contacts and renormalization of a layered system as discussed in Subsec. 3.2.4. In particular, as a prior task for the simulations, the definition of the Hamiltonian and its evaluation were, together with the geometrical definition of the defects in TMD ribbons, the main contributions to the numerical code development during my PhD, and they will be presented later in Sec. 4.2. This Section illustrates the general structure and procedure of the numerical codes.

Figure 4.1 shows the flowchart of the quantum transport simulations performed by the numerical codes. The first step is to define a unit cell, which is the building block of the system, for given lattice parameter and TMD ribbon chirality (n,m). The ribbon chirality determines the unit cell and the translation vectors, see Ref. [181] for more details. In this thesis, two repre-

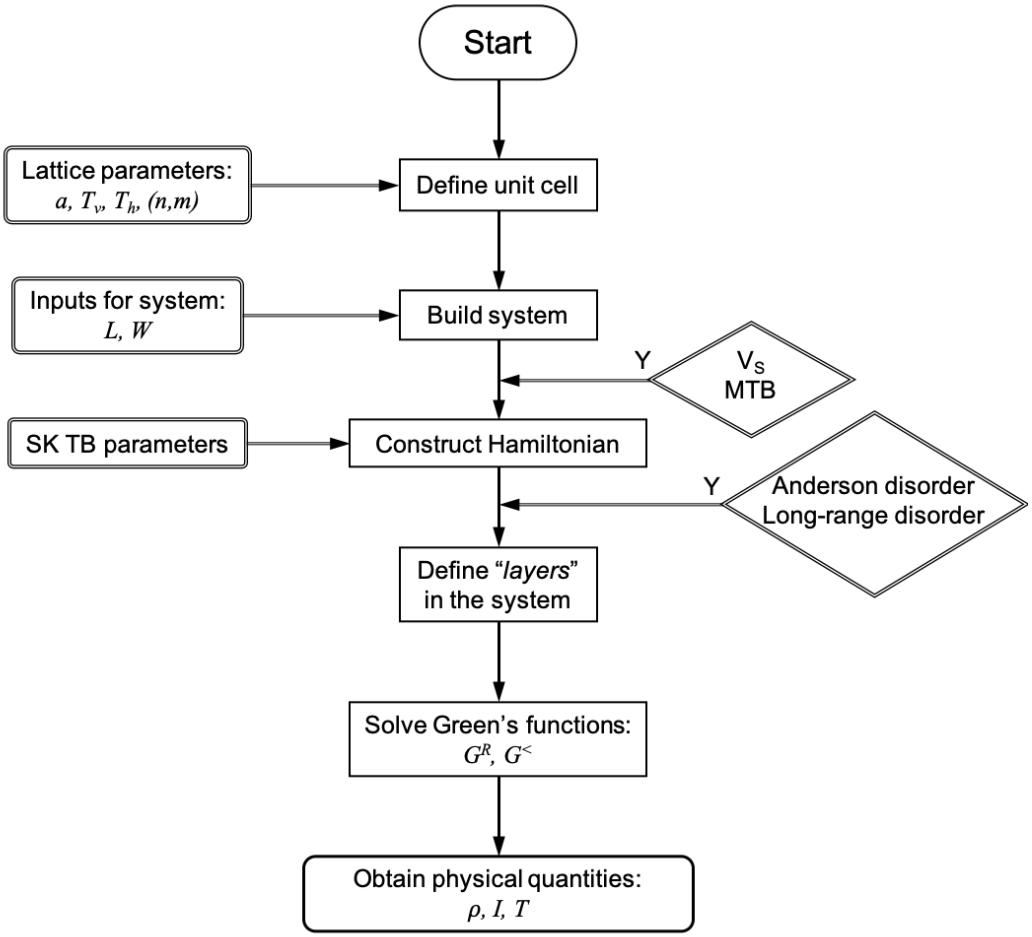

Figure 4.1: Flowchart of numerical code for the simulation of quantum electron transport in TMD ribbons. V_S denotes sulfur vacancies of MoS_2.

sentative ribbon orientations are considered: armchair, which corresponds to $n = m = 1$, and zigzag, which corresponds to $n = 1$ and $m = 0$. The resulting unit cells and translation vectors are indicated in Fig. 4.2. We make use of this unit cell as a building block to construct a system of width W and length L. Note that the system consists of a central region (C), which extends over length L, connected to the source and drain electron reservoirs by periodic semi-infinite left (L) and right (R) leads.

Based on the spatial coordinates of the atoms, the Hamiltonian of the system is calculated in the framework of the SK TB model with the parameterization of Ref. [29], as discussed in Sec. 2.1. On the basis of the coupling between atomic orbitals as encoded in the TB Hamiltonian, the code defines layers of orbitals that are only coupled with their neighbor layers. Once the Hamiltonian is defined and the system is layered, the code evaluates the self-

energies of the periodic semi-infinite contacts by the renormalization method. Then, by using the calculated self-energies of the contacts and the Hamiltonian of the layered system, the Green's functions for any layer within the central region are calculated by decimating the other layers one-by-one and by renormalizing the Hamiltonian accordingly. More details of these techniques are presented in Subsec. 3.2.4. From the so-obtained Green's functions, the code extracts all the requested physical quantities, such as the local density of states and transmission coefficient.

The main objective of my thesis is to investigate the impact of various disorders on the transport properties of TMD materials. For this purpose, several representative disorders found in experiments, as discussed in Sec. 1.4, are considered. Atomistic disorders such as vacancies, line defects and edge roughness are introduced when building the system. In this respect, the calibration of the geometrical (in particular the lattice distortion) and Hamiltonian parameters against DFT results is essential. Other considered sources of disorders only introduce a variation of the on-site potentials of atoms, i.e. they appear on the diagonal of the Hamiltonian matrix, and can then be introduced after the geometric construction of the system. More specifically, I implemented Anderson disorder [178], which corresponds to random very short-range potential variations on the atoms of the system, as well as long-range Gaussian impurities, which will be detailed in Sec. 6.1.

4.2 Implementation of TB Hamiltonians

In order to build the atomistic SK TB Hamiltonian of the system, we start from the structure of TMD material, which shows a hexagonal geometry whose primitive cell (blue rhombus) and lattice vectors (blue arrows) are indicated in Fig. 4.2. For the representative orientations, zigzag and armchair, we make use of a rectangular cell (red rectangle) as a unit block, whose lattice vectors (red arrows) are aligned along the x- and y-directions, to build the complete system. In the case of MoS_2, such a cell contains six atoms: two Mo atoms and four S atoms. We thus have 22 orbitals in total *per* cell (three p orbitals for each S atom and five d orbitals for each Mo atom). Each layer of the system is then built as a vertical series of cells and, accordingly, the whole system can is obtained with a longitudinal series of layers. Note that the number of cells in each layer determines the width of the system, while the number of the layers in the central region determines its length.

The Hamiltonian in the second quantization representation for the mth layer can be expressed as

$$H_{m,m} = \sum_{\alpha,\mu} \epsilon_{\alpha\mu} c^{\dagger}_{\alpha\mu} c_{\alpha\mu} + \sum_{\langle\alpha\beta\rangle,\mu\nu} \left[t_{\alpha\mu,\beta\nu} c^{\dagger}_{\alpha\mu} c_{\beta\nu} + \text{H.c.} \right] , \tag{4.1}$$

where the operators $c^{\dagger}_{\alpha\mu}$ ($c_{\alpha\mu}$) create (annihilate) an electron in the orbital μ

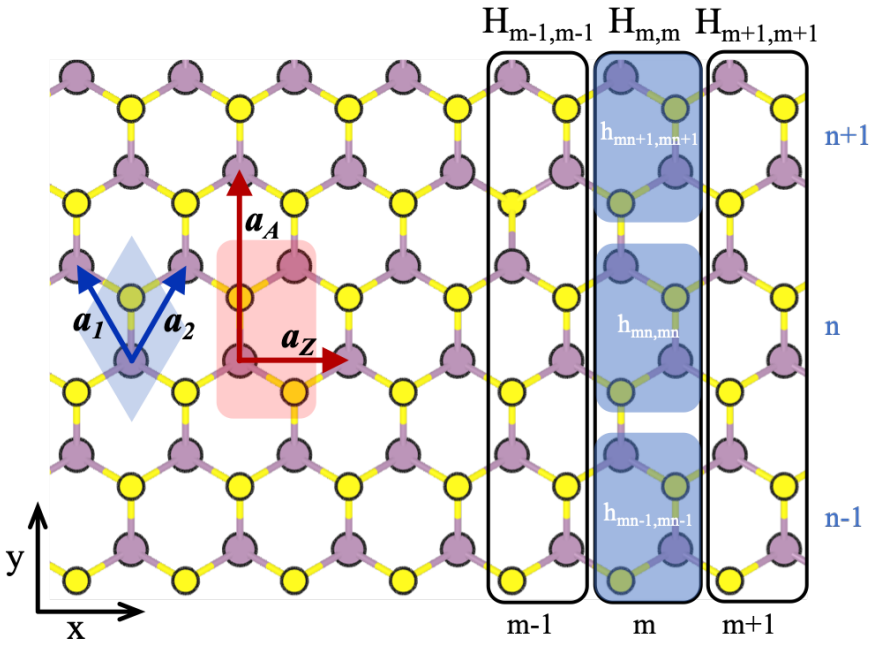

Figure 4.2: Atomistic structure of a layered system as Fig. 3.3. In this example, the transport direction aligns the zigzag orientation. Blue rhombus and arrows represent the primitive cell and its lattice vectors of TMDs, respectively. Red rectangle and arrows denote a unit cell and its lattice vectors of the representative orientations (zigzag and armchair), respectively. Purple and yellow dots denote molybdenum and sulfur atoms, respectively.

of the atom α belonging to layer m. The parameter $\epsilon_{\alpha\mu}$ is the on-site energy of the orbital μ in the atom α and $t_{\alpha\mu,\beta\nu}$ is the hopping energy between the orbital μ of the atom α and the orbital ν of the atom β. The first term contributes to the diagonal elements of the matrix. For the second term, $\langle\alpha\beta\rangle$ denotes a sum over pairs of atoms ($\alpha \neq \beta$), whose couplings include the NN Mo-S^{t,b}, Mo-Mo, and S-S (S^t-S^t, S^b-S^b, S^t-S^b) [29]. In the implemented code, this operation is performed by scanning all the atoms of layer m and finding their neighbor atoms in the same layer m within a given cut-off distance. Then, the hopping energy for each pair is obtained by the SK two-center energy integrals given in Table 2.1. In a similar way, the coupling term $H_{m\pm1,m}$ can be obtained by browsing the neighbor atoms within layer $m \pm 1$.

In the case of 2D systems, the system is obtained by periodically replicating the cell along the transverse y-direction. By making use of the basis of the Bloch states, we obtain a more manageable (and finite size) k_y-dependent Hamiltonian $H(k_y)$.

Chapter 5

Transport in rough MoS_2 ribbons

In microelectronics, an important aspect is the progressive miniaturization of the transistors, which enables the reduction of the power consumption, the increase of the switching speed and the large scale integration. This trend was prophesized by the Moore's law [76] and pragmatically coded in the International Technology Roadmap for Semiconductors [77] and more recently in the International Roadmap for Devices and Systems [78], which suggest the implementation of nanometer-size channels for the next transistor generation. Keeping the pace with this trend is technologically very challenging. Indeed, it is known that, in standard bulk semiconductor-based transistors, miniaturization is associated with performance degradation due to the so-called short-channel effects. They include electrostatic issues as well as source-to-drain direct tunneling, which originates from the quantum nature of electrons. The further lateral confinement of the transistor channel, in the case for example of nanowire transistors or FinFETs, exacerbates the problem of roughness at the interface between semiconductor and oxide, thus affecting the charge mobility [79], [80].

We can expect analogous problems for devices based on 2D materials [82], when using nanoribbons [83] as channel for ultrascaled devices. For the use of TMD nanoribbons, one issue is the presence of metallic edge states within the bulk gap and the other is edge roughness inevitably found in experiments, see more details in Subsec. 1.4.3. In particular, edge roughness is expected to play a major role in narrow ribbons obtained from 2D materials, due to the large length or surface ratio of the disordered edges with respect to the whole system surface. In the case of semiconducting TMDs, a physical and quantitative understanding of the impact of edge roughness on the transport properties of ribbons with nanometer width is essential in view of their potential application in ultrascaled nanoelectronics. In this Chapter, the impact of edge roughness on the transport properties of MoS_2 is investigated by means of atomistic

description presented in Sec. 2.1 and the Green's function technique detailed in Sec. 3.2. Section 5.1 introduces the geometric structure for this study and the model for edge roughness. In Sec. 5.2, we consider two aspects: the conductance due to edge states within the bulk gap and that of bulk states outside the gap. For better understanding, a quantitative insight by estimating physical quantities such as localization length and mean free path in terms of the transport regime is presented. Finally, Sec. 5.3 concludes.

This Chapter and its figures are largely reproduced from [J. Park, M. Mouis, F. Triozon, and A. Cresti, *Impact of edge roughness on the electron transport properties of MoS_2 ribbons*, Journal of Applied Physics **124** (22), 224302 (2018), doi: 10.1063/1.5050383], with the permission of AIP Publishing.

5.1 Simulation model

For the investigation of the impact of edge roughness on MoS_2 ribbons, we make use of an atomistic description of TB model, which reasonably describes atomistic disorders, and consider a 1D system along the x-direction. Edge roughness is introduced over a region with length L of the system. According to the atomistic structure, the Hamiltonian can be obtained in the TB description as discussed in Sec. 4.2.

In Subsec. 5.1.1, I introduce a model of edge roughness for MoS_2 ribbons and its parameterization by the comparison with the experimental results of Ref. [81]. Furthermore, according to the model of edge roughness, the geometric structure of the system as well as its Hamiltonian are detailed in Subsec. 5.1.2.

5.1.1 Model of edge roughness

We consider MoS_2 ribbons of width W, infinitely extended along the ribbon axis on both sides, and with a section of length L with rough edges, as shown in Fig. 5.1. Note that the two contacts are periodic in the x-direction without any edge roughness while the central part of the system has edge roughness over L. Edge roughness is introduced by generating random spatial profiles for the edges with shift $\Delta(x)$ along the transverse direction y and with autocorrelation function

$$\langle \Delta(x')\Delta(x-x') \rangle \;=\; \Delta_m^2 e^{-|x|\sqrt{2}/\ell_m} \;, \tag{5.1}$$

where Δ_m is the roughness amplitude and ℓ_m is the correlation length. This model is inspired by Ref. [182], where it is adopted to describe surface roughness at the interface between silicon and silicon oxide.

Reference [81] provides transmission electron microscopy micrographs of high-quality $MoSe_2$ zigzag nanoribbons obtained by MBE, see Fig. 1.8. It turns out that the roughness along the chalcogen-terminated edge is larger

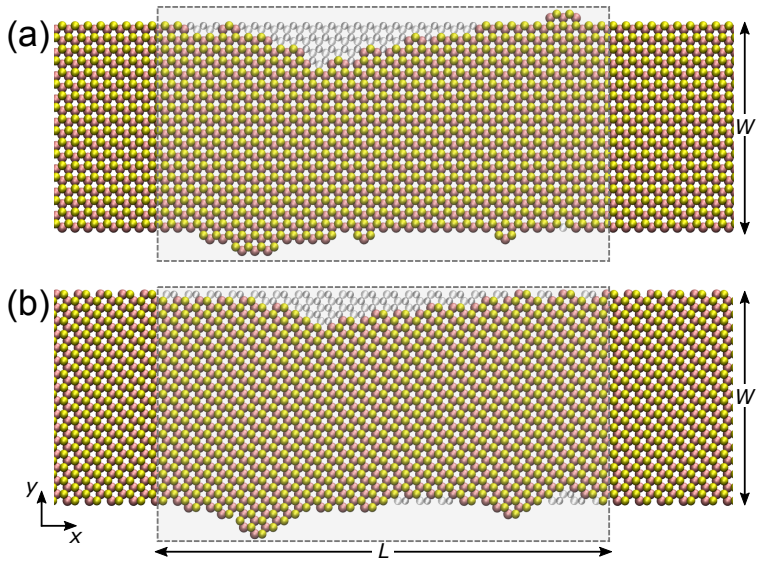

Figure 5.1: Sketch of (a) zigzag and (b) armchair MoS_2 ribbons. Mo atoms are in pink color, S atoms are in yellow color. The left part and right part of the ribbons are pristine, which corresponds to the contacts. The central part has edge roughness. In the region with rough edges, removed Mo and S atoms are indicated in gray color.

than along the metal-terminated edge. We approximately reproduce the experimental profiles by setting $\ell_m = 5$ nm, and $\Delta_m = 0.5$ nm and 0.25 nm, respectively. This asymmetry of the two different edges can be interpreted in terms of the energy gain. DFT calculations revealed that the energy gain of the reconstructed Mo-terminated edge is 0.82 eV, while that of the reconstructed Se-terminated edge is 0.16 eV, indicating that the Mo-terminated edge is more stable and thus becomes straighter than the Se-terminated edge [81]. For a fair comparison with zigzag ribbons, we consider an intermediate value $\Delta_m = 0.375$ nm on both edges of armchair ribbons. An example of edge roughness realization is illustrated in Fig. 5.1. Note that the rough edges are allowed to exceed the nominal width W of the ribbon.

5.1.2 Model structure

As representative of the two main crystallographic orientations, we consider zigzag (z-MoS_2) and armchair (a-MoS_2) ribbons, see Fig. 5.1. Note that, in the absence of edge roughness, z-MoS_2 terminate differently on the two edges, either with S atoms or Mo atoms while a-MoS_2 edges are symmetric and contain both species. We consider the presence of edge roughness on both edges over a region with length L, with the same parameters discussed above for $MoSe_2$. Left and right contacts connected to the central part are semi-

infinite in the $-x$- and $+x$-direction, respectively. Note that the contacts are pristine without edge roughness and thus they preserve their periodicity with the translation vectors, which allows the renormalization of the contacts as shown in Subsec. 3.2.4.

To describe the system, we make use of the TB model of Ridolfi *et al.* [29], which properly takes into account the atomistic details of the system, in particular of the rough edges, and accurately reproduces the low-energy electronic structure over the whole BZ, see Sec. 2.1.2. Note that we do not modify the model parameters at the ribbon edges, thus implicitly assuming their perfect passivation. To reduce the computational burden, we do not include SOC. Indeed, SOC is found not to play an essential role in our case, as we will discuss in Subsec. 5.2.6.

5.2 Results and discussion

By means of calculations of the Green's functions introduced in Sec. 3.2 based on the atomistic TB model, we explored the electronic properties as well as the electron quantum transport of MoS_2 ribbons in the presence of edge roughness. As discussed in Subsec. 1.4.3, zigzag edges show metallic properties with the presence of states along the edges for energies within the bulk band gap, while for armchair edges the dispersive bands corresponding to edge states do not completely close the bulk band gap, thus leaving some forbidden energy ranges, see the red bands in the insets of Fig. 5.2. In what follows, I will provide a detailed analysis of the electronic structure of these states and of the robustness of their transport properties in the presence of edge roughness. Furthermore, I will show the impact of edge roughness on the conductance for energies outside the bulk band gap, which provides a physical understanding of the transport degradation for the use in electronic applications.

This Section is organized as follows. Subsection 5.2.1 details the electronic structure of MoS_2 ribbons with two representative orientations, a-MoS_2 and z-MoS_2. In Subsec. 5.2.2 and Subsec. 5.2.3, we investigate electron transport of the edge and bulk states, respectively, in the presence of edge roughness. Furthermore, the scaling analysis of the transport properties with physical quantities is reported. The detailed analysis of the impact of edge roughness on the conductance of the bulk states outside the gap are discussed in terms of the mean free path in Subsec. 5.2.4. Moreover, the different impact of edge roughness on a-MoS_2 and z-MoS_2 and the effect of SOC, which gives a large spin-splitting of the VB in TMD materials, are discussed in Subsec. 5.2.5 and Subsec. 5.2.6, respectively.

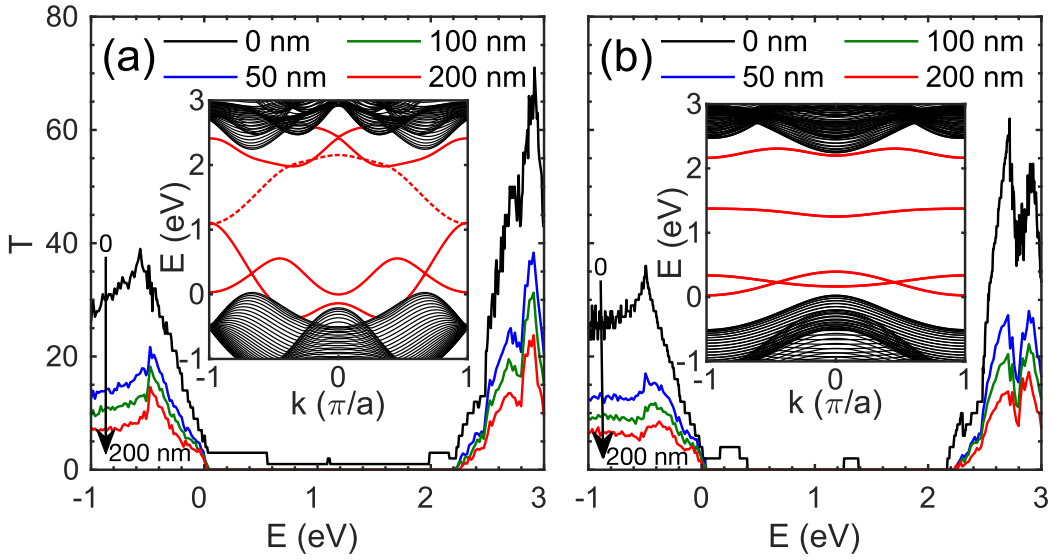

Figure 5.2: (a) Inset: Band structure of a z-MoS_2 with width $W = 10$ nm. The bands corresponding to edge states are indicated by red lines. Main panel: Transmission coefficient for the ribbon in the pristine case ($L = 0$) and in the presence of edge roughness over a section of length L varying from 50 nm to 200 nm. The parameters for edge disorder generation are $\ell_m = 5$ nm, $\Delta_m = 0.5$ nm on the S-terminated edge and 0.25 nm on the Mo-terminated edge. (b) Same as (a) for an a-MoS_2. In this case, $\Delta_m = 0.375$ nm on both edges.

5.2.1 Electronic properties

We consider zigzag and armchair MoS_2 ribbons with width $W = 10$ nm. The insets of Fig. 5.2 show the corresponding band structure as obtained from the TB Hamiltonians. In the case of the z-MoS_2, we observe three valence valleys, two at the BZ sides and one at the center. They correspond to the K/K' valleys and Γ valley of 2D MoS_2, respectively. Note that these bulk bands (black lines) appear as quantized subbands due to lateral confinement. As for the CB, we observe four main valleys, which correspond to the K/K' and Q valleys of 2D MoS_2. Importantly, some edge states (indicated by red lines) are present within the bulk band gap. The edge states corresponding to the band indicated by a dashed red line are located at the S-terminated edge of ribbon, while the edge states corresponding to the bands indicated by continuous red lines are on the Mo-terminated edge. This asymmetry, which relates the energy of the edge states to their spatial distribution, is also experimentally confirmed in the case of $MoSe_2$ zigzag ribbons [81]. In the case of the a-MoS_2, the valence Γ and K/K' valleys of 2D MoS_2 are all folded at the center of the BZ, where a single valley appears. In the CB, the K/K' valleys of 2D MoS_2 are folded at the center of the BZ and the Q valleys at the sides. Again, edge states are present. However, they do not completely close

the band gap. These states are doubly degenerate and located at both edges, since the a-MoS_2 has symmetric edges.

The main panels of Fig. 5.2 report the transmission coefficient T as a function of the electron energy E for the pristine ribbons and in the presence of edge roughness over ribbon sections of length L. For pristine ribbons, T is quantized and equal to the number of active bands at energy E. In particular, we observe the significant contribution of the bands from the Γ valley for $E \lesssim -200$ meV. Analogous considerations hold for the Q valleys in the CB. Note that such contributions would incorrectly not be present if we made use of a simple $k \cdot p$ model, see Sec. 2.2. Within the bulk band gap, due to the presence of the dispersive edge states, electron transport is possible in the absence of edge roughness.

5.2.2 Localized transport regime of edge states

In the presence of edge roughness, the transmission coefficient of the edge states is completely suppressed, and a transport gap opens in correspondence of the band gap of 2D MoS_2. As already reported in the literature [138], this is a consequence of the quasi-1D nature of these states, which determines their localization in the presence of short-range disorder. To better quan-

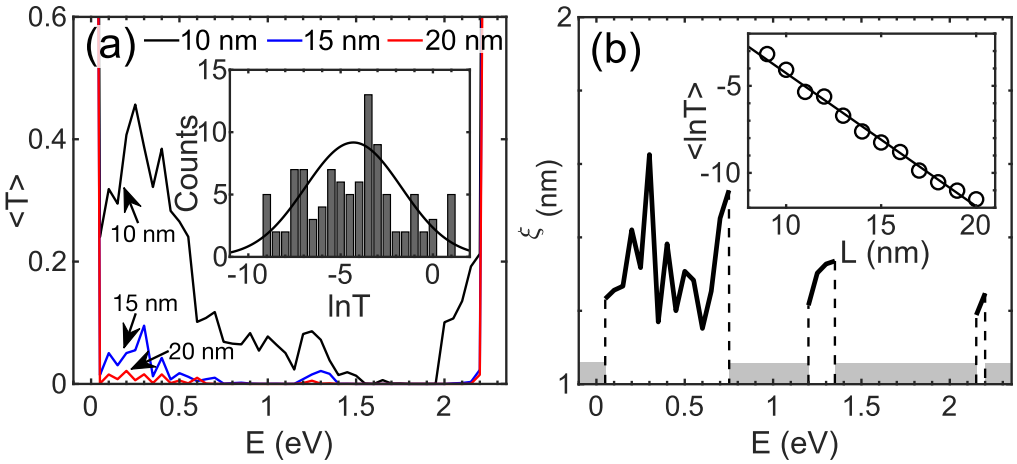

Figure 5.3: (a) Main panel: Average transmission coefficient as a function of the electron energy for the z-MoS_2 with width $W = 10$ nm in the energy range of the bulk band gap. The average is performed over 100 realizations of edge roughness. Inset: Frequency distribution of $\ln T$ for $L = 10$ nm at $E = 0.5$ eV. (b) Main panel: Localization length as a function of the electron energy. The shadowed regions correspond to energy ranges where we could not extract ξ, because too small (inside the bulk band gap) or too large (just outside the bulk gap). Inset: Average logarithm of the transmission coefficient as a function of L at $E = 0.5$ eV. The continuous line corresponds to the linear fit.

tify this behavior, we consider shorter lengths $L \leq 20$ nm and an ensemble of 100 edge disorder realizations for each length. Figure 5.3(a) reports the average transmission coefficients $\langle T \rangle$ as a function of the energy within the band gap. We observe that $\langle T \rangle$ rapidly decreases for increasing L and it is already strongly suppressed for $L = 20$ nm. This suggests that the transport regime is localized, as confirmed by the inset of Fig. 5.3(a), which shows, for the representative energy $E = 0.5$ eV and length $L = 10$ nm, a typical Gaussian frequency distribution of the transmission coefficient logarithm $\ln T$ with $|\Delta \ln T \ / \ \langle \ln T \rangle| < 1$, where $\Delta \ln T$ is the standard deviation, in agreement with the criterion of the localized transport regime discussed in Sec. 3.3. The inset of Fig. 5.3(b) confirms the linear scaling of $\langle \ln T \rangle$ with L for the representative energy $E = 0.5$ eV. The main panel of Fig. 5.3(b) reports the localization length as a function of the energy, extracted from eq. (3.110). We find that $\xi \approx$ 1-2 nm within the whole bulk gap, thus confirming the extremely short localization length for the edge states and the suppression of their transmission contribution for $L \gtrsim 20$ nm. If, on the one hand, this makes the experimental observation of edge states in realistic samples difficult, on the other, it restores the bulk gap and limits subthreshold leakage in transistors. Note, however, that a residual edge conductivity is experimentally measured in micrometer-size samples [92], which might be related to the specific passivation of the edge dangling bonds.

5.2.3 Diffusive transport regime of bulk states

Outside the gap region, T decreases progressively when increasing L from 50 nm to 200 nm, as shown in Fig. 5.2. This suggests that a transition from ballistic to diffusive transport regime takes place. To better investigate this aspect, we consider again an ensemble of 100 different edge roughness realizations for each length L. Figure 5.4 shows the average transmission coefficients. We can confirm that the transport regime is diffusive by looking, for given E and L, at the frequency distribution of T around its average value $\langle T \rangle$, as discussed in Sec. 3.3. As in the example reported in the insets of Fig. 5.4 for a representative energy $E = 2.3$ eV and length $L = 100$ nm, we observe a typical Gaussian distribution with $\Delta T / \langle T \rangle < 1$, with ΔT the standard deviation of T. According to eq. (3.109), the channel resistance R_{ch} scales linearly with L, which allows us to extract the mean free path ℓ, see Fig. 5.5. With the exception of the energy regions at the band gap edges, for the chosen configuration and disorder parameters, both z-MoS_2 and a-MoS_2 show a relatively large mean free path ℓ between 40 nm and 60 nm. Therefore, these ribbons are expected to be in the quasi-ballistic transport regime for L in the order of tens of nm ($L < \ell$), and to stay in the diffusive regime up to hundreds of nm ($L < N\ell$) before entering the localized regime ($L \gg N\ell$).

5.2.4 Scaling of mean free path

We now consider how the mean free path scales with the ribbon width W and the roughness strength Δ_m. Figure 5.6 reports ℓ for a representative energy $E = -200$ meV in the VB. But for some fluctuations, we observe that ℓ scales linearly with the ribbon width and is inversely proportional to $\Delta_m^{3/4}$. The fit for this specific case is indicated in the caption of Fig. 5.6. Such a behavior is consistent with the observation that the effect of the edge roughness is expected to be proportional to the area of the disordered edges over that of the pristine *bulk* region. The detrimental effect of edge roughness on electron transport is thus considerably more significant in ultra-narrow ribbons. Indeed, for $W = 5$ nm the mean free path can be less than 20 nm at the edges of the bulk gap. Therefore, in that energy range, transport rapidly degrades and enters the localized regime for longer ribbons, with an estimated localization length $\xi \approx 75$ nm. We can thus conclude that ultra-narrow ribbons ($W < 5$ nm) undergo a stronger reduction of the charge mobility around the bulk gap.

To be more quantitative, we calculated the room-temperature differential conductance $G(\mu, L)$ of 5 nm wide ribbons with different roughness amplitudes as a function of the chemical potential μ and the length L by using eq. (3.108). To reduce the computational burden, we considered the average over only 10 realizations for each roughness amplitude, and not over an ensemble of 100 realizations as for the other simulations. The results are

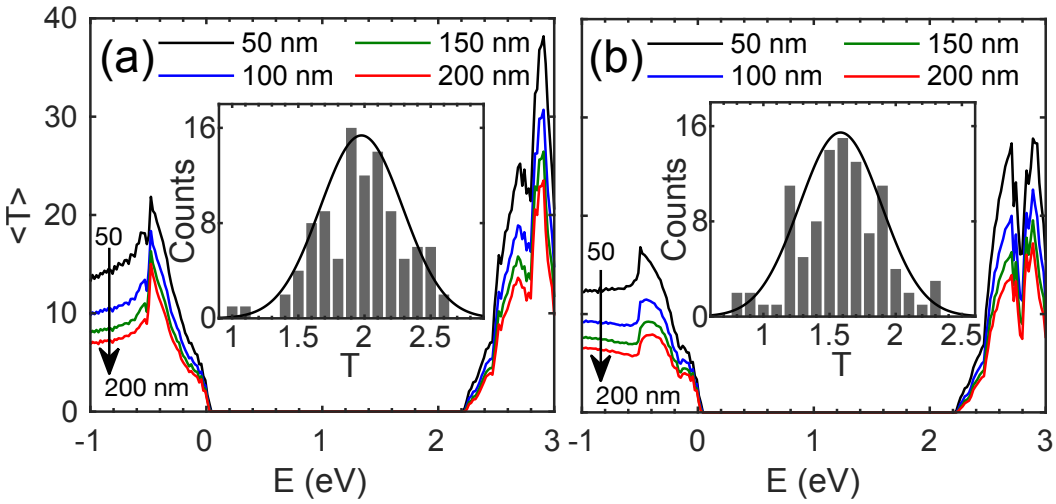

Figure 5.4: Main panels: Average transmission coefficient as a function of the electron energy for (a) the z-MoS_2 and (b) the a-MoS_2 of Fig. 5.2. The average is performed over 100 realizations of edge roughness. Insets: Frequency distribution of T for $L = 100$ nm at $E = 2.3$ eV, in the CB just above the bulk gap. The standard deviation ΔT is around 0.3 in both cases.

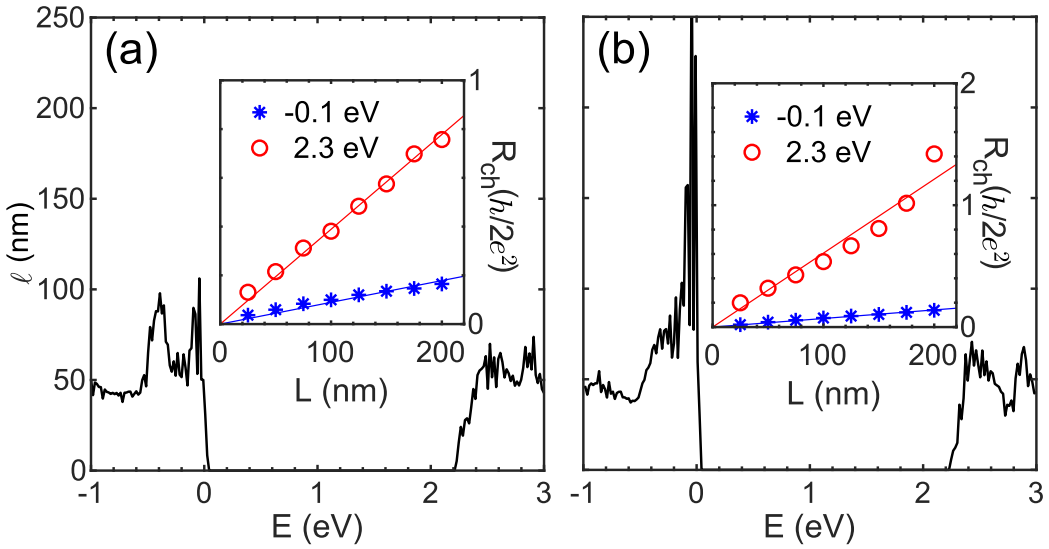

Figure 5.5: Main panels: Mean free path as a function of the electron energy for (a) the z-MoS_2 and (b) the a-MoS_2 of Fig. 5.4. Insets: Average zero-temperature channel resistance at two selected electron energies close to the edges of the bulk gap, $E = -100$ meV and $E = 2.3$ eV. The continuous lines correspond to the linear fit with length L.

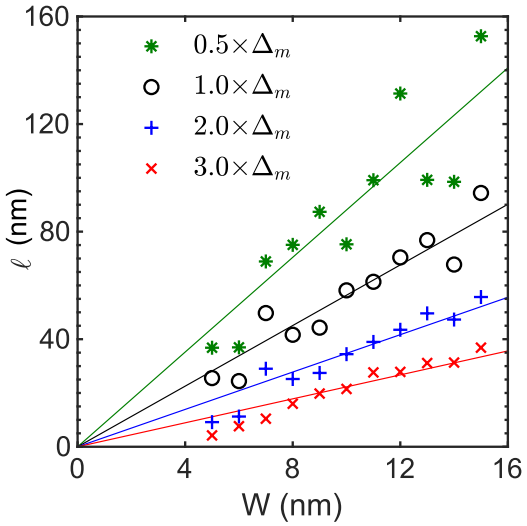

Figure 5.6: Mean free path for a z-MoS_2 at $E = -200$ meV as a function of the ribbon width and for different strengths of the edge roughness. The case $1.0 \times \Delta_m$ corresponds to $\Delta_m = 0.5$ nm on the S-terminated edge and 0.25 nm on the Mo-terminated edge. In the other cases, Δ_m are scaled accordingly. For the configuration here considered, we find $\ell \approx 2.61\ W\ /\ \Delta^{3/4}$ nm, where Δ is the average of Δ_m on the two edges. The continuous lines correspond to the linear fit.

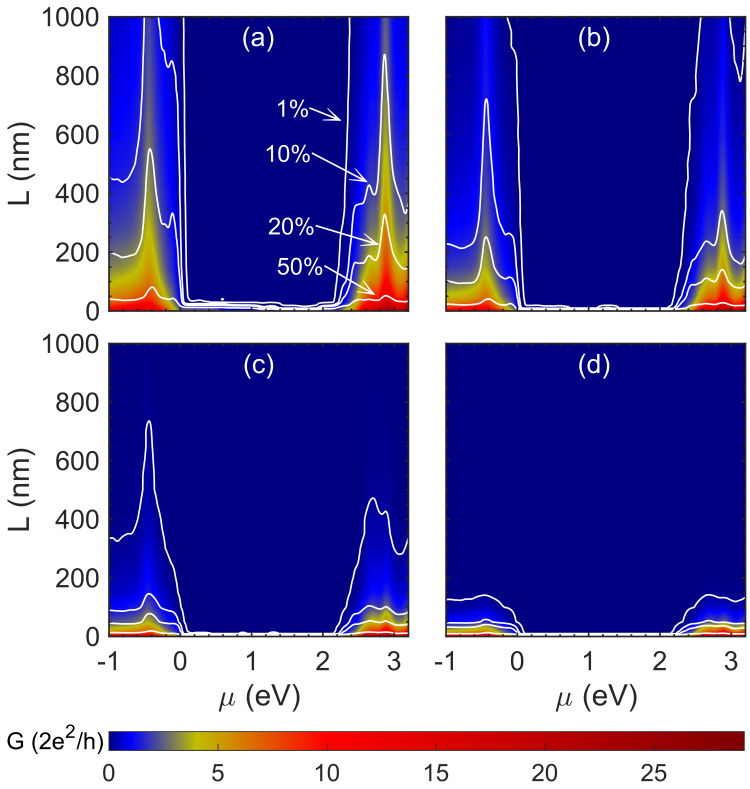

Figure 5.7: Color map: average room-temperature differential conductance over an ensemble of 10 zigzag ribbons of width 5 nm as a function of the chemical potential μ and the length L of the rough ribbon section, for different values of the roughness amplitude (a) $0.5 \times \Delta_m$, (b) $1.0 \times \Delta_m$, (c) $2.0 \times \Delta_m$, and (d) $3.0 \times \Delta_m$. The white lines indicate the length where the conductance is 1%, 10%, 20% and 50% that of the pristine ribbon.

anyway representative, since the long length of the ribbon and the temperature smearing introduce a self-averaging effect, which limits the variability between different disorder realizations. The white lines in Fig. 5.7 indicate the length where the conductance is reduced to 50%, 20%, 10% and 1% that of the pristine ribbon.

5.2.5 Different behavior of zigzag and armchair ribbons

In Fig. 5.2, we observe that for large L and $E \lesssim -300$ meV, the transmission coefficient for $E \lesssim -300$ meV is more affected for a-MoS_2 than for z-MoS_2. At first sight, this difference is surprising, because the number of conductive modes are quite similar in the two cases, and the effective mass of 2D MoS_2 at K, K' and Γ points is rather isotropic [183]. Since the different behavior starts at an energy that roughly coincides with the activation of the Γ valley,

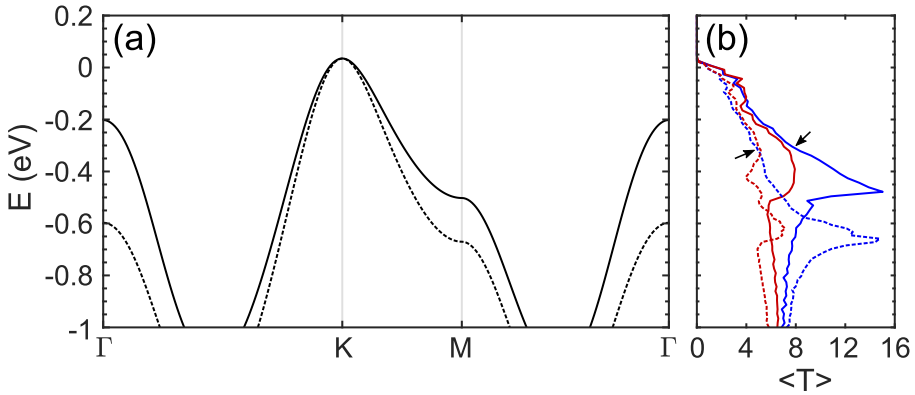

Figure 5.8: (a) Continuous line: Top VB of 2D MoS_2. Dashed line: Top VB of 2D MoS_2 with modified TB parameters to shift down the states at the Γ-point and exclude their contribution to transport. The band shift is obtained by decreasing the on-site energy of the orbital d_{z^2} of Mo atoms by -0.4 eV, which corresponds to the states at Γ. (b) Continuous lines: Average transmission coefficient for z-MoS_2 (blue) and a-MoS_2 (red). Dashed line: Average transmission coefficient for for z-MoS_2 (blue) and a-MoS_2 (red) with the modified TB parameters. Arrows indicate the energy where the average transmission coefficient for a-MoS_2 and z-MoS_2 starts to differ.

we initially conjectured that its physical origin was related to some enhanced inter-valley scattering. In order to examine this possibility, we made a change of the TB parameters to artificially shift the valence Γ valley toward more negative energies, see Fig. 5.8(a). Then, we recalculated the average transmission coefficient with the new parameters and compared it with the previous result, see Fig. 5.8(b). Surprisingly, the smaller transmission coefficient of a-MoS_2 compared to that of z-MoS_2 is still observed with the modified parameters in the same energy range. Therefore, we ruled out this possibility and excluded any significant role of inter-valley scattering.

A clarifying physical insight can instead be gained by looking at the local density of states. Figure 5.9 shows the difference between the density of states, averaged over the ribbon length, across the ribbon section in the presence and in the absence of edge roughness. While for z-MoS_2 no significant variation is observed along the edges, for a-MoS_2 localized edge states form at negative energies (see arrows), which enhance electron scattering. Though only the results for a single disorder realization are shown here, we verified that this behavior is general. We ascribe such a difference to the different way edge roughness affects the ribbon geometry in the two orientations. As shown in Fig. 5.1(b), due to the orientation of the ribbon axis, in a-MoS_2 the roughness mainly entails the formation of adjacent and extended zigzag segments with Mo-terminated or S-terminated edges. As a consequence, edge states form on the Mo-terminated regions (as at the Mo-terminated edges

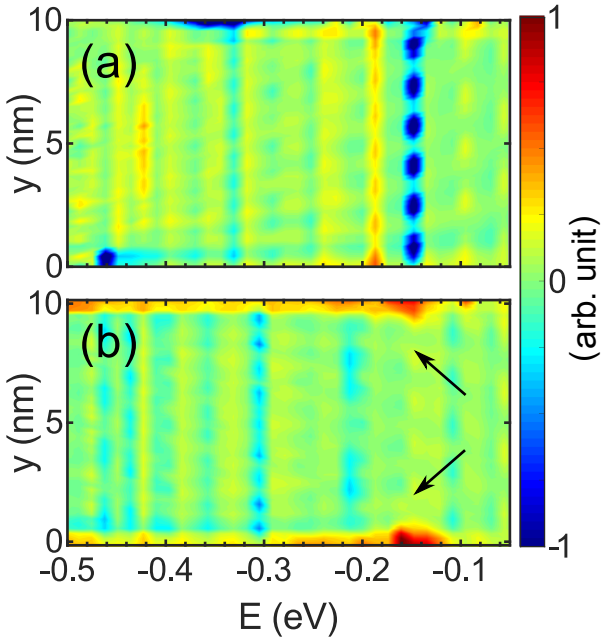

Figure 5.9: (a) Difference of the density of state, averaged over the whole disordered region, between a rough and a pristine z-MoS_2 as a function of the electron energy and the y-coordinate along the ribbon transverse section. The vertical features correspond to the band edges in the pristine system, where van Hove singularities appear. (b) Same as (a) for an a-MoS_2. The arrows indicate the localized states induced at the ribbon edges. It can be shown that they are located on Mo-terminated edge segments.

of pristine z-MoS_2 at negative energies), which are separated by the insulating S-terminated regions (since the edge states in the S-terminated edges of z-MoS_2 are only present at positive energy). Note that, differently from z-MoS_2, pristine a-MoS_2 do not show any edge state for $E < 0$, see the insets of Fig. 5.2. These states, only induced by roughness, are at the origin of the enhanced backscattering, especially at more negative energies ($E \lesssim -300$ meV), since the corresponding bulk modes have a more significant component at the edges and thus their coupling to the induced edge states is larger.

5.2.6 Effect of spin-orbit coupling

Finally, we would like to comment on the role of SOC, whose strength is quite substantial in TMDs [25], as discussed in Chapter 2. We repeated the simulation for the z-MoS_2 of Fig. 5.2(a) by doubling the basis and including SOC in the Hamiltonian [131]. As illustrated in Fig. 5.10(a), the energy bands of the pristine z-MoS_2 show the expected spin-splitting of the VB at the K/K' valleys. To be more precise, in the absence of SOC, the edge of

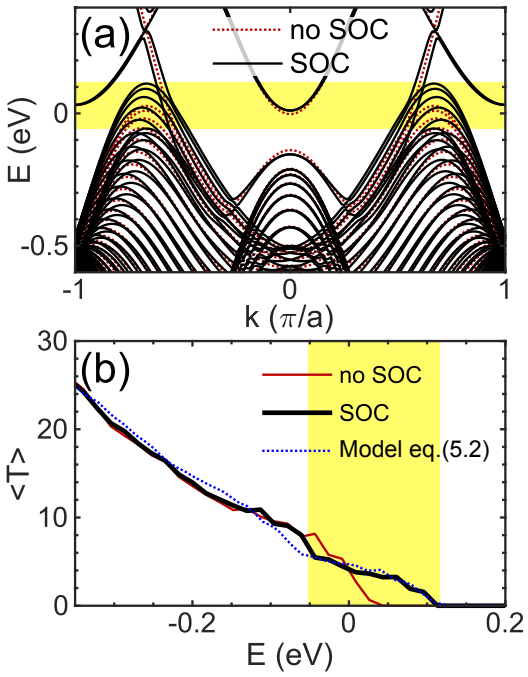

Figure 5.10: (a) Band structure of the z-MoS_2 ribbon of Fig. 5.2(a) in the presence of SOC. The band structure in the absence of SOC is indicated by red thin lines, for comparison. The yellow stripe indicates the energy separation between the spin-split bands at K and K' valleys. (b) Transmission coefficient for the pristine ribbon and in the presence of edge roughness over a length $L = 100$ nm, with and without SOC. Note that to take into account the spin degeneracy in the absence of SOC, the transmission coefficients have been doubled compared to the previous figures.

the VB at K and K' valleys is at $E \approx 28$ meV. In the presence of SOC, the VB at K/K' split into two series of bands, one starting at $E \approx 113$ meV and the other at $E \approx -57$ meV. The split bands are spin polarized, with opposite polarization at different valleys. This splitting is indicated by a yellow horizontal strip in the figure, which separates the two series of spin-split bands. If now we examine the average transmission coefficient $\langle T_{\rm SOC}\rangle$ obtained for a rough ribbon with $L = 100$ nm with SOC, see Fig. 5.10(b), we obtain that it can be roughly fitted by

$$\langle T_{\rm SOC}(E)\rangle \;\approx\; \frac{\langle T_{\rm no-SOC}(E-85{\rm meV})\rangle \;+\; \langle T_{\rm no-SOC}(E+85{\rm meV})\rangle}{2}\;, \qquad (5.2)$$

where $T_{\rm no-SOC}$ is the transmission coefficient in the absence of SOC obtained before (and multiplied by 2 to take into account spin degeneracy), while the energy shifts correspond to the energy spin-splitting of the bands. In other words, apart from the energy shift and the removed spin degeneracy, the transmission coefficient is roughly the same as in the case without SOC inves-

tigated before. This validates our previous assumption, and, more interestingly, excludes any significant role of inter-valley scattering at low energies. Indeed, due to the spin-valley locking [145] and the absence of magnetic disorder, inter-valley scattering just below the charge neutrality point is forbidden, contrary to the case without SOC. Since the observed behavior is *de facto* equivalent in the two cases, we can conclude that the complete suppression of inter-valley scattering by SOC does not significantly affect the way edge roughness degrades the electron transport.

5.3 Summary

In this Chapter, I presented a numerical study of the quantum electron transport properties of MoS_2 nanoribbons with edge roughness. The edge states of the pristine ribbon are found to rapidly localize, with a localization length in the nanometer order. As a consequence, the electron transport within the bulk gap is strongly suppressed. For energies outside the bulk gap, the main conclusion is that for ribbon widths larger than 10 nm and moderate (but realistic) edge roughness, the system shows a rather large mean free path, which allows the system to stay in the diffusive transport regime over a large range of ribbon lengths. The effect of edge roughness is thus compatible with the use of TMD ribbons in nanoelectronics. The mean free path decreases with the ribbon width, thus more rapidly degrading the conductance of ultra-narrow ribbons, especially for energies close to the bulk gap edges. Completely smooth edges, as obtained for ribbons produced by electron irradiation [85] or encapsulation in carbon nanotubes [86], would prevent the transport regime to become localized in ultra-narrow ribbons, but, at the same time, would not suppress the edge conductance within the bulk gap.

Chapter 6

Transport along and across disordered mirror twin grain boundaries in MoS_2

For applications, a large-scale fabrication of large-area TMDs is crucial. In this respect, CVD [54]–[56] has emerged as a very efficient growth technique, which is promising for industrial production, as discussed in Sec. 1.3. However, CVD TMDs may present several kinds of defects, which are expected to significantly impact the electronic and transport properties, with possible degradation of the device performance. The most common defect is the polycrystallinity of CVD TMDs, which is inherent in the synthesis process, see more details in Subsec. 1.4.2. The grain boundaries at the interfaces between crystalline grains have been reported to strongly localize electrons [58], with consequent carrier mobility degradation [59], [60]. Therefore, understanding the impact of grain boundaries on the transport properties of TMDs is of central importance.

In this Chapter, based on the Green's function approach discussed in Sec. 3.2 and a DFT-calibrated TB model, we explore electron quantum transport along and across grain boundaries in MoS_2. Among the huge variety of grains boundaries with different geometries, we focus here on MTBs, which show interesting properties. As mentioned in Sec. 1.4, an MTB forms at the interface between two grains with a 60° rotation angle, see Fig. 6.1(a) and (b). DFT calculations [56], [72], [73] and STS [66] reveal that MTBs show conducting states within the bulk gap of the two-dimensional semiconducting TMDs. This is illustrated in Fig. 6.1 (c) and (d) in the case of $MoSe_2$.

More precisely, we investigate the *robustness of transport along the MTB channels against short-range and long-range disorders*. Such a study is important to understand to what extent grain boundaries could be deleterious for applications, such as FETs based on 2D materials, where they could contribute to the leakage current through the TMD band gap. At the same time, conductive MTB networks, as those obtained by MBE [66], could be

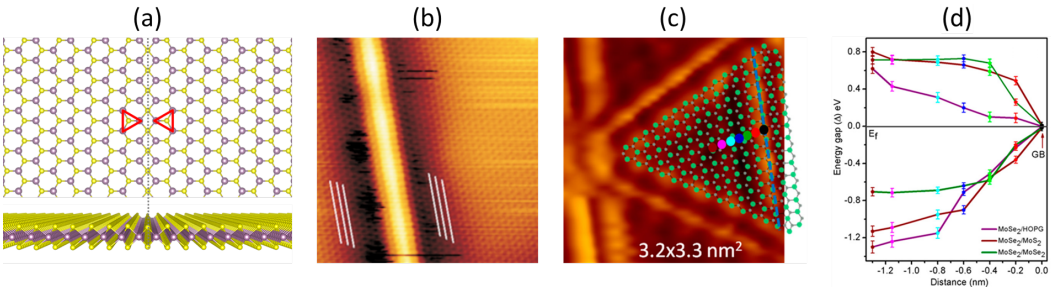

Figure 6.1: (a) Top and side view of the MTB considered in this thesis. (b) STM image of an MTB in MoS_2. (c) STM image of a network of MTBs in $MoSe_2$ obtained by MBE. One of the MTBs is indicated by a blue dashed line. (d) Energy gap obtained by STS measurements along the line, indicated in (c), for three different samples. The closure of the gap indicates that the grain boundary is metallic. Panel (b) is adapted from Ref. [184]. Panels (c) and (d) are adapted with permission from [Y. Ma *et al.*, *Metallic Twin Grain Boundaries Embedded in $MoSe_2$ Monolayers Grown by MBE*, ACS Nano 11 (5), 5130-5139 (2017), doi: 10.1021/acsnano.7b02172]. Copyright (2017) American Chemical Society.

exploited to realize metallic contacts from semiconducting TMDs. Therefore, understanding how their conductivity is affected by the presence of disorder is particularly important. Furthermore, we simulate electron transport across an MTB in 2D MoS_2 and provide a physical understanding of its degradation. This study is important for applications in electronics and for the possible perspectives it opens in spin-valleytronics.

In Sec. 6.1, I introduce the simulation model and detail the adopted procedure for the calibration of TB parameters for the description of systems with MTBs. In Sec. 6.2, I present the simulation results together with a full analysis of the impact of MTBs on the transport properties of MoS_2. Lastly, Sec. 6.3 concludes.

This Chapter and its figures are largely reproduced from [J. Park, K.-H. Xue, M. Mouis, F. Triozon, and A. Cresti, *Electron transport properties of mirror twin grain boundaries in molybdenum disulfide: Impact of disorder*, Physical Review B **100** (23), 235403 (2019), doi: 10.1103/physrevb.100.235403], ©2019 American Physical Society (APS).

6.1 Simulation model

TB models are computationally low-cost and highly flexible for the investigation of large systems with low geometric symmetry and with various defects, as discussed in Sec. 2.1. In particular, the TB models based on the SK description can be adapted (up to a certain extent) to describe systems with lower symmetry. Thus, we make use of the TB model of Ref. [29] for the description

of TMD grain boundaries, which induce large geometrical distortions. A finer tuning of the model takes into account the strain in the vicinity of the grain boundaries, the calibration of the parameters to reproduce the energy levels and density of states corresponding to the grain boundary states, and SOC, which is known to play an important role in TMDs.

6.1.1 Calibration of the TB model

Strain effect

The presence of MTBs induces a large distortion in the geometric structure of the 2D MoS_2, with a change of the interatomic distances in the vicinity of MTBs. Figure 6.2 shows the change of bonding distances with respect to the pristine case, as obtained by DFT calculations, for the representative type of 4|4 P MTB shown in Fig. 1.7. The magnitude of strain is up to 4.5% and this behavior is related to changes of the coordination number for the S atoms along the MTB. While each S atom in the pristine case has three neighbor Mo atoms, the S atoms in the 4|4 P MTB have four neighbor Mo atoms. The region affected by strain is rather narrow, with a width of ∼1 nm around the grain boundary.

The use of the SK TB model allows us to take in consideration the effect of strain. The two-center energy integral elements [185] depend on the interatomic distance d_{ij} between i and j orbitals, which can be expressed as

$$V_{ij}(d_{ij}) = V_{ij}(d_{ij}^0)\left(\frac{d_{ij}^0}{d_{ij}}\right)^{\gamma_{ij}} , \tag{6.1}$$

where d_{ij}^0 is the equilibrium interatomic distance for the given hopping energy V_{ij}, and γ_{ij} is a fitting parameter. This parameter can be assumed as $\gamma_{ij} = l_i + l_j + 1$ with l_i and l_j the angular momenta of the orbitals i and j,

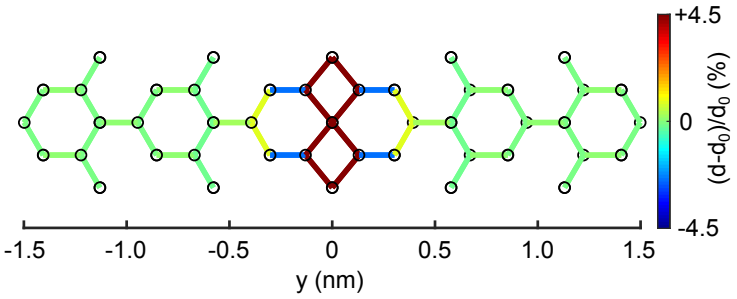

Figure 6.2: Strain of bonding distances Mo-S between neighbor atoms in the vicinity of a 4|4 P MTB, with respect to the distances in the pristine MoS_2. Optimized structure is obtained by DFT calculations.

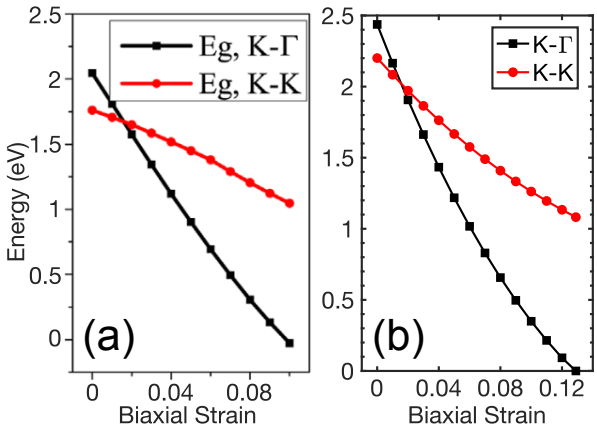

Figure 6.3: The K-K direct bandgap and the K-Γ indirect bandgap under different biaxial strains obtained with (a) non-orthogonal first-nearest neighbor sp^3d^5 TB model [185] and (b) orthogonal 11-band model [138]. (a) Reprinted from [185]. Copyright (2017) Wiley Online Library.

respectively [133]. Together with the relaxed geometry obtained from DFT calculations, this provides an accurate description of the effect of strain induced by the MTB.

To verify whether this strain effect is properly reproduced by the TB model, we investigate the bandgap engineering by biaxial strains and compare the results with the previous study of Ref. [185]. Figure 6.3 shows the comparison between both models for the direct energy gaps at K valley and indirect gaps between K and Γ valleys as a function of strain. With both models, a transition from direct to indirect gap occurs for a biaxial strain of about 2.5 %. Furthermore, a semiconductor-metal transition is observed, but at a strain of about 13 % with our chosen TB model, which is higher compared to that found in Ref. [185].

Calibration with DFT results

Even after the consideration of the strain effect induced by MTBs, a further calibration of the TB model is required for the accurate description of the MTB states. To this aim, we analyze the wave functions of the MTB states as resulting from the TB model, see Fig. 6.4, and compare them with those obtained by DFT calculations. The shape of the MTB bands within the gap as well as the different spatial extension of their wave functions for states on bands ① and ②, which denote two MTB bands within the gap, well match the DFT results [72], [184]. The bands corresponding to the edge states do not match those of the cited references, since they depend on the specific edge passivation. However, we are not interested here in edge states. As for the

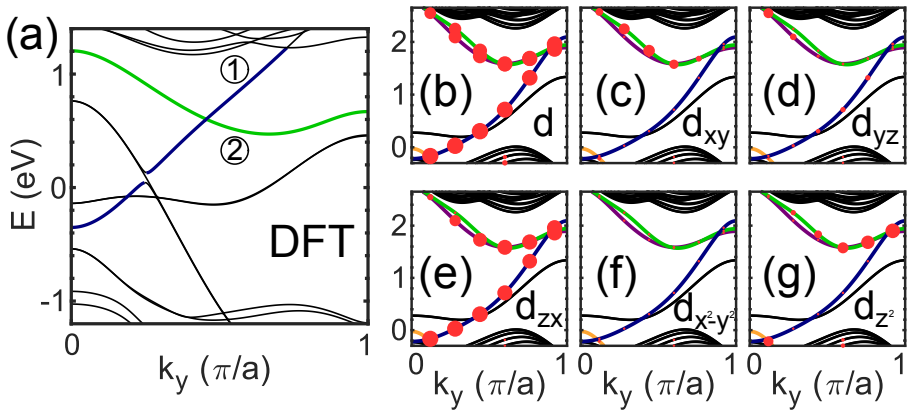

Figure 6.4: (a) Band structure obtained by DFT calculations for a ribbon with width $W = 2.2$ nm and a periodic MTB along its axis. Such a narrow ribbon width was chosen to reduce the computational burden. However, the shape of the MTB bands is not significantly affected by the ribbon width, provided the ribbon is large enough to avoid the coupling between edge and MTB states. ① and ② indicate the two MTB bands within the bulk gap, which are highlighted in blue and green lines. (b-g) Band structure of a zigzag ribbon with width $W = 10$ nm obtained with the non-calibrated TB model and without SOC. The MTB bands within the bulk gap are indicated in blue, green and purple lines. The MTB bands in blue and green lines correspond to band ① and band ② in (a). The orange lines display the MTB band above the bulk states at the Γ point. The red circles denote the weight of the corresponding wave functions of (b) all d orbitals, and on the selected orbitals of the molybdenum atoms in the MTB region: (c) d_{xy}, (d) d_{yz}, (e) d_{zx}, (f) $d_{x^2-y^2}$, and (g) d_{z^2}. The contribution of S atoms to the MTB bands within the bulk gap is insignificant compared to that of Mo atoms and thus not displayed.

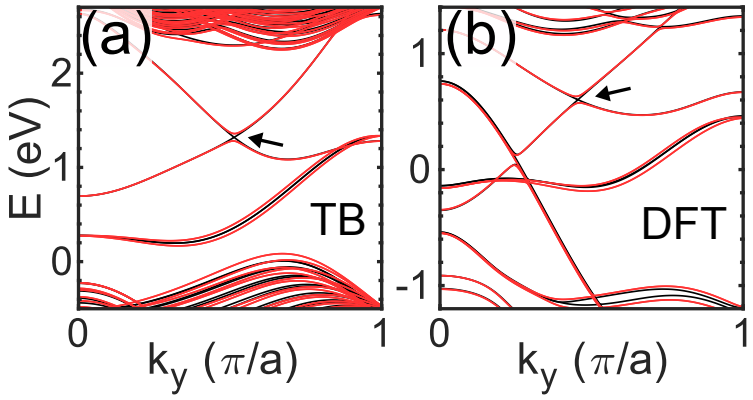

Figure 6.5: (a) Band structure obtained with the calibrated TB model for the ribbon of Fig. 6.4(b). The SOC-induced gap is indicated by an arrow. (b) Band structure obtained by DFT calculations for the ribbon of Fig. 6.4(a). The SOC-induced gap, indicated by an arrow, is ∼60 meV, i.e. slightly narrower than ∼80 meV observed for the TB case. Black and red lines display the bands without and with SOC, respectively.

states along the MTB, the main difference with DFT calculations is the energy downshift of band ①. By the analysis of the wave function composition, we observe that the main contributions to band ① come from the Mo orbitals d_{yz} and d_{zx}, see Figs. 6.4(c) and (d), respectively. To shift the energy of band ①, we thus modified the on-site energies of the corresponding orbitals of the Mo atoms closest to the MTB. The shift is +1 eV for the d_{zx} orbital and +0.2 eV for the d_{yz} orbital. The extreme spatial localization along the grain boundary of the states of band ① allows us to shift it without significantly affecting the other bands. Note that the extra MTB band indicated by purple lines in Fig. 6.4, which possesses the same orbital contribution as band ①, is also shifted upward to the bottom of and inside the CB. The other aspect to take into account is the presence of MTB states on the top of the VB at the Γ point, which appears at even higher energies than the bulk states, see the orange lines in Figs. 6.4. However, in the DFT results, the MTB states at Γ in the VB are located at lower energies [184]. Therefore, we modified the on-site energies of the same Mo atoms by -0.3 eV for the d_{xy} orbital and by -0.8 eV for the d_{z^2} orbital, so to shift down and calibrate the energy of the MTB states in the VB.

Figure 6.5(a) shows the band structure of a MoS_2 ribbon with a periodic MTB along its axis obtained with the calibrated TB model, with and without SOC. The MTB states (band ① and band ②) within the bulk gap well reproduce those of the DFT calculation, see Fig. 6.5(b). The MTB states outside the bulk gap, as well as the presence of MTB states below the edge of the VB and close to the edge of the CB, also agree with the results of Ref. [184]. Note that the SOC couples band ① and band ②, which results

in their anticrossing and in the opening of a small gap of the order of 60 meV, which is indicated by an arrow in Fig. 6.5.

Details of the density functional theory calculations

The DFT results shown above and used for the TB Hamiltonian calibration were obtained by Prof. Kan-Hao Xue, who had been visiting professor at IMEP-LaHC for one year starting from September 2018. The computational details of the DFT calculations are as follows. DFT calculations were carried out using the plane-wave basis set with a kinetic energy cutoff of 500 eV and the projector augmented-wave method, as implemented in the Vienna *Ab initio* Simulation Package [186]. Generalized gradient approximation of the Perdew-Burke-Ernzerhof functional form [187] was used. The valence electron configurations were $4d$ and $5s$ for Mo, $3s$ and $3p$ for S, $1s$ for H. The BZs were sampled using Γ-centered k-point mesh. Monolayer MoS_2 was fully relaxed with a vacuum layer greater than 2 nm to avoid its interaction with periodic images along the c-axis. The resulting Mo-S bond length is 2.41 Å, while the a-axis lattice constant is 3.175 Å. A ribbon model with MTB was set up, whose width is 2.24 nm and the optimized lattice constant along the a-direction is 3.179 Å, very close to the pure monolayer case. At least 1 nm vacuum space was introduced in the b- and c-directions, and four hydrogen atoms per supercell were introduced to saturate the corresponding four S atoms on the edges. The electronic structures were calculated either with or without SOC.

6.1.2 Model structure

The main objectives of this Chapter are the study of the robustness of the conductivity of the extended 1D states along the MTBs and the study of their impact on the bulk conductance when transport is orthogonal to the MTB. For the study of transport along the MTB, we consider MoS_2 ribbons oriented along the y-axis, with a periodic MTB along its axis, see Fig. 6.6(a). Note that we exclusively focus on the rather common geometry called 4|4 P [56], whose relaxed structure calculated by DFT is shown in Fig. 6.2. To focus on the MTB transmission and suppress the contribution of the ribbon edge states, which are also present in the bulk band gap and would thus complicate the analysis, we consider a wide ribbon of W=10 nm, so to avoid the coupling between the edges and MTBs. Moreover, we introduce edge roughness with amplitude 0.25 nm over a length of at least 20 nm, so to suppress the edge-state contribution to transport, as observed for $L \gtrsim 20$ nm in Fig. 5.3(a) in the previous Chapter.

To investigate transport across the MTB, which may give a physical understanding of polycrystalline MoS_2, we consider a 2D system that is infinite

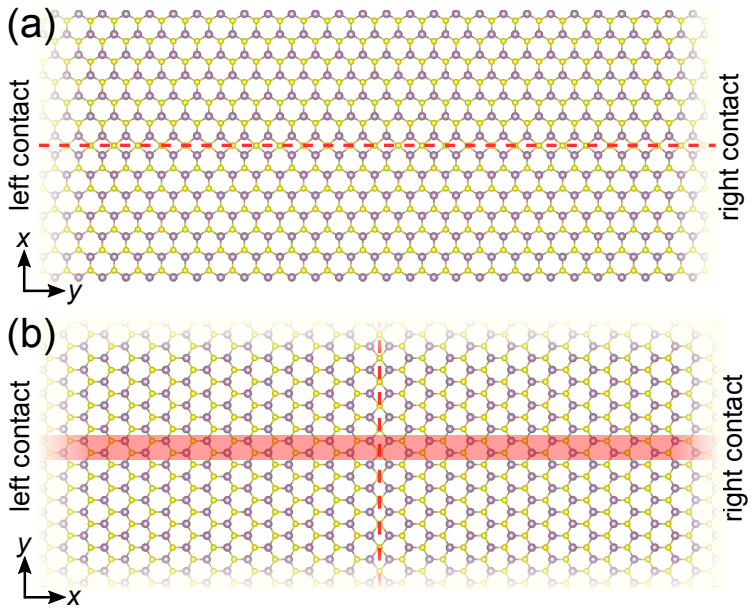

Figure 6.6: Sketch of systems used to calculate the transport properties (a) along and (b) across an MTB in MoS_2. (a) MoS_2 ribbon with a 1D periodic MTB. Semi-infinite contacts are obtained by the prolongation of the pristine regions on both sides along the y-axis. (b) 2D MoS_2 with a perpendicular MTB. The cell shaded in red is repeated periodically along the y-direction. Note that the contacts on the left and right directions are semi-infinite along the x-axis. Dashed lines in red indicate MTBs. Purple and yellow circles represent Mo and S atoms, respectively.

in both x- and y-directions with an MTB perpendicular to the transport direction, see Fig. 6.6(b). In particular, the system is periodic along y-axis and obtained by the periodic repetition of the unit cell highlighted in red. This periodicity along the y-axis allows us to define a k_y-dependent Hamiltonian and, as a consequence, a k_y-dependent transmission coefficient, which will be discussed in Subsec. 6.2.3.

6.2 Results and discussion

By means of calculations of the Green's functions based on the DFT-calibrated TB model discussed in Subsec. 6.1.1, we explored the electronic properties of MTBs as well as the electron quantum transport along and across an MTB in MoS_2, according to the system geometries described in Subsec. 6.1.2. As discussed earlier in Subsec. 1.4.2, MTBs show metallic properties, with the presence of extended states along the grain boundary for energies within the bulk band gap. After analysing in detail the electronic structure of these states also in terms of orbital composition, we investigated their transport proper-

ties, and in particular their robustness against short-range and long-range disorders. We also considered the case of a 2D MoS_2 layer with an MTB orthogonal to the transport direction, and provided a physical understanding of the transport degradation that goes with it. Note that SOC is taken into account in all calculations, which is found to play an important role, unless otherwise specified.

This Section is organized as follows. Subsection 6.2.1 details the electronic properties of the MTB. In Subsec. 6.2.2 and Subsec. 6.2.3, we investigate the electron transport along and across an MTB, respectively. The scaling analysis of the transport properties in the presence of disorder, the analysis in terms of two individual MTB bands, and the importance of SOC are also reported.

6.2.1 Electronic properties of MTBs

We consider MoS_2 ribbons with a periodic MTB along their axis in the y-direction, see Fig. 6.6(a). Note that the MTB is along the zigzag direction, which implies that edges are along the zigzag orientation. Figure 6.7(b) shows the band structure of a zigzag ribbon with width $W = 10$ nm and a periodic MTB along its axis. These results are comparable with those previously obtained in the literature by DFT calculations [184]. The electronic structure consists of bulk bands, with direct gap at the K and K' points, which appear as quantized subbands due to lateral confinement, and dispersive bands within the bulk gap. Among these latter, in addition to those corresponding to edge states, we find those (indicated by red dots) corresponding to MTB states. The two MTB spin-degenerate bands within the bulk band gap, indicated by ① and ② in Fig. 6.7(b), display different properties in terms of wave functions and atomic orbital compositions, as discussed in the previous section. In particular, band ① exhibits a narrow wave function (with width up to ∼0.8 nm) composed of d_{yz} and d_{zx} Mo orbitals, while band ② shows a spatially more extended wave function (with width up to ∼1.3 nm) mainly stemming from d_{xy}, d_{z^2} and d_{x^2} orbitals of Mo atoms, see more details in Subsec. 6.1.1 and Fig. 6.7(c).

We would like to further comment on the effect of SOC, which is responsible for the anticrossing of the two MTB bands and the opening of a small gap in the order of 80 meV, see the inset of Fig. 6.7(b). This feature is also observed in the DFT calculations, where the results with and without SOC clearly show the band anticrossing and crossing, respectively, as we saw in Fig. 6.5. The anticrossing is the consequence of the hybridization between two MTB bands induced by the SOC coupling of the different orbitals composing the two bands. Note that the bands are spin-degenerate, because, in contrast with the pristine MoS_2, in the presence of the MTB the system is invariant under inversion symmetry. Together with the time-reversal symmetry,

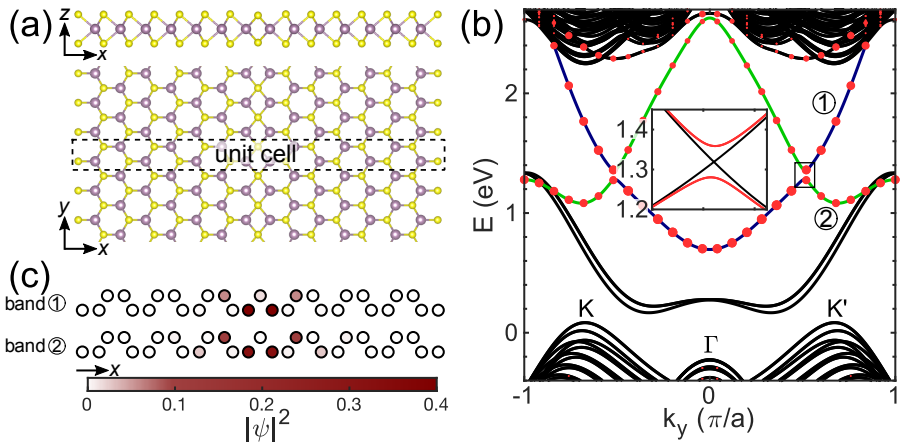

Figure 6.7: (a) Side and top views of the relaxed atomic structure of a periodic MTB in MoS_2. Mo atoms are in purple color and S atoms are in yellow color. The dashed rectangle indicates a unit cell for the ribbon, which is periodic along the y-direction and whose lattice parameter is $a = 0.316$ nm. (b) Band structure obtained with the calibrated TB model of a zigzag ribbon with width $W = 10$ nm and a periodic MTB along its axis. ① and ② indicate the two spin-degenerate MTB bands within the bulk gap, which are highlighted in blue and green lines. The size of the red dots corresponds to the weight of the states on the molybdenum atoms in the MTB region. The indicated K, K' and Γ points correspond to the projection of the corner and the center of the hexagonal BZ of 2D MoS_2 onto the 1D BZ of the ribbon. Inset: band structures with (red line) and without (black line) SOC in the region indicated by a square. The energy gap induced by SOC is ∼80 meV, which is close to that found by DFT calculations, see Fig. 6.5 for more details. (c) Probability density of the states at $E = 2$ eV on bands ① and ② on the atoms close to MTB.

this entails the Kramers degeneracy of the bands. While for the whole ribbon the presence of the inversion symmetry requires the MTB to be exactly along the ribbon axis (as in our case), such a symmetry always holds for the region around the grain boundary itself. As a consequence, the spin-degeneracy of the MTB dispersive bands within the bulk band gap is expected to be generally observed.

Let us now analyze how bulk states outside the bulk band gap are affected by the MTB. As shown in Fig. 6.8(a), the shape and the spacing of the quantized bulk VBs for the ribbon in the presence of the MTB are comparable to those of a pristine ribbon with a half-width, i.e. $W = 5$ nm. This indicates that the MTB has the effect of "cutting" the ribbon into two narrower ones. The weak coupling between these resulting two ribbons induces a small splitting of the VBs, as observed in the figure. Note that the split bands of the ribbon with MTB are spin-degenerate. On the contrary, the small splitting observed for the pristine ribbon bands is due to the joint effect of SOC and

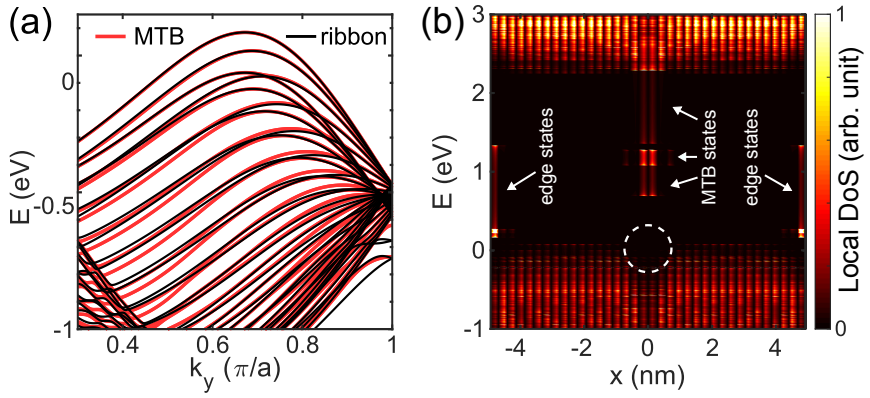

Figure 6.8: (a) Band structures of a zigzag ribbon with $W = 10$ nm and the MTB along its axis (same as in Fig. 6.7) and for a pristine zigzag ribbon with half-width $W = 5$ nm. Only the VB region is shown. (b) Local density of states of the ribbon with an MTB as a function of the x-coordinate along the ribbon transverse section and the electron energy E. Edge states and MTB states within the bulk gap are indicated by white arrows. A white dashed circle displays the region with reduced density of states on the MTB.

absence of inversion symmetry. A more detailed physical insight can be gained by looking at the local density of states (LDoS) displayed in Fig. 6.8(b) as a function of the electron energy E and of the x-position across the ribbon. The MTB is located in the center at $x = 0$ nm. In agreement with the band structure of Fig. 6.7(b), the LDoS exhibits MTB states within the bulk band gap, while it vanishes away from $x = 0$ nm. More importantly, as shown as the dashed circle in Fig. 6.8(b), the LDoS turns out to be relatively low in the vicinity of the MTB in the VB, thus illustrating and confirming the effective separation of the ribbon into two narrower ribbons. This effect also significantly affects the transport properties, as we will discuss in Subsec. 6.2.3.

6.2.2 Transport along MTBs

In this subsection, we investigate the electron transport along the MTB, as shown in Fig. 6.6(a), in the energy region of the bulk gap, where the grain boundary states are active and surrounded by an insulating bulk. We study the robustness of the MTB conductive channels against additional short-range disorder (single sulfur vacancies and Anderson disorder) and long-range (Gaussian) impurities. We provide a quantitative scaling analysis in terms of the different (quasi-ballistic, diffusive and localized) transport regimes, as discussed in Sec. 3.3. Before proceeding, we would like to recall that, for an infinite periodic ribbon with an MTB but no additional disorder, the transmission coefficient is quantized at values corresponding to the number of active conductive channels at given energy.

Sulfur vacancies

Sulfur vacancies, as one of the most common defects observed in experiments, are expected to induce localized midgap states, which can significantly affect transport [188]. These vacancies could be fatal for the conductive MTB channels within the bulk gap.

To investigate this aspect, we introduce one single sulfur vacancy at different distances from the grain boundary, see Fig. 6.9(a). The impact of the single sulfur vacancy is expected to be negligible when the vacancy is far enough from the grain boundary, because the localized vacancy states and the MTB states are spatially separated. Indeed, we do not observe any impact of the vacancy when its distance d from the MTB is larger than ~ 1.4 nm. This is consistent with the fact that the vacancy state has a spatial extension of about 0.5 nm [188], while the MTB states have a maximum extension of about 1.3 nm. For shorter distances and down to $d \approx 0.6$ nm, however, the MTB transmission shows some dips around specific energies, see Fig. 6.9(b). Such dips are a clear indication of resonant scattering between the MTB states and the localized vacancy states, as confirmed by the correspondence between the dip energies and the energies of the vacancy states, see the dashed lines in Fig. 6.9(c). When the vacancy is closer to the grain boundary ($d = 0.3$ nm), its impact is much more effective and the transmission decreases over the whole energy range. Interestingly, when the sulfur vacancy is exactly placed on the grain boundary, we observe a strong suppression of two conductive channels for energies $E > 1.1$ eV, as demonstrated by the nearly quantized transmission coefficient $T \approx 4$ and $T \approx 2$ compared to $T = 6$ and $T = 4$ for the pristine system. We find that the suppressed conductive channels cor-

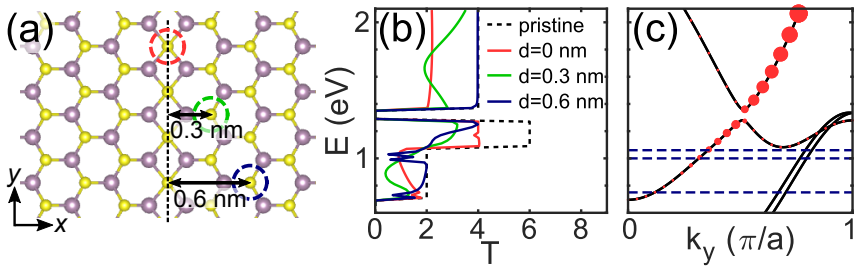

Figure 6.9: (a) Three sulfur vacancy positions, indicated by circles, at different distances d from the MTB. (b) Transmission coefficient as a function of energy for the pristine system and in the presence of a single sulfur vacancy at the three positions specified in (a). (c) Band structure of the pristine ribbon in the bulk gap region. The size of the dots indicates the weight of the sulfur component of the corresponding states, which is only present for ①. The dashed lines indicate the energies of the localized sulfur vacancy states for the system of Fig. 1.6(b) in inclusion of SOC.

respond to the MTB spin-degenerate band ①, which is contributed by the sulfur atoms. The sulfur weight in the wave functions is indicated by dots in Fig. 6.9(c). Sulfur orbitals hardly contribute to band ②, which is active for $E \gtrsim 1.1$ eV, and thus the corresponding conductive channel is not appreciably affected by the vacancy.

Anderson disorder

The short-range Anderson disorder [178] introduces a random potential energy for each atom with value in the range $[-\Delta, \Delta]$, where Δ is the disorder strength. Despite its simplicity, such a popular disorder model allows a general physical understanding of the effect of very short-range disorders. Figure 6.10(a) shows an example of generated random on-site potentials with strength $\Delta = 100$ meV applied on the atoms close to the grain boundary over a section of length L. Note that having disorder over the whole ribbon width would not modify our results, which are focused on energies within the bulk band gap. That is why we limit Anderson disorder to a stripe that is wide enough to cover the spatial extension of MTB states. To better statistically analyze the different transport regimes according to the theory outlined in Sec. 3.3, we consider an ensemble of 100 Anderson disorder realizations for each case under study.

Figure 6.10(b) reports the transmission coefficient for the pristine MTB and the average transmission coefficients $\langle T \rangle$ in the presence of Anderson disorder as a function of the electron energy E within the bulk band gap for $\Delta = 100$ meV and different lengths L. We can identify three energy regions, indicated in Fig. 6.10(b) by the letters A (for $E \lesssim 1.1$ eV), B (for 1.1 eV $\lesssim E \lesssim 1.29$ eV, i.e. below the SOC-induced gap) and C (for $E \gtrsim 1.37$ eV, i.e. above the SOC-induced gap). In region A, only band ① is active and the decrease of $\langle T \rangle$ with L is exponential for $L > 100$ nm. According to the criterion discussed in Sec. 3.3, this suggests a transition to the localized transport regime, with a Gaussian frequency distribution of $\ln T$, with $|\Delta \ln T / \langle \ln T \rangle| < 1$. By using eq. (3.110), the localization length is extracted as $\xi \approx 25-80$ nm. Such a localization length entails a huge transmission suppression when L is hundreds of nm. In region B, where six conductive channels are active, i.e. both bands ① and ② contribute and the energy is below the SOC-induced gap, $\langle T \rangle$ decreases more slowly with increasing L, as shown in Fig. 6.10(b). This suggests that the system is in the diffusive transport regime, which is characterized by a mean free path ℓ, as obtained by eq. (3.109), ranging between 20 nm and 50 nm. Finally, in region C, the average transmission coefficient decreases very slowly, which indicates that the system is in transition from the quasi-ballistic to the diffusive transport regime, as evidenced by the extremely large estimated mean free path up to $\sim$0.8 μm. Therefore, at these energies the MTB conductive channels are expected to be robust against Anderson disorder, and to stay in

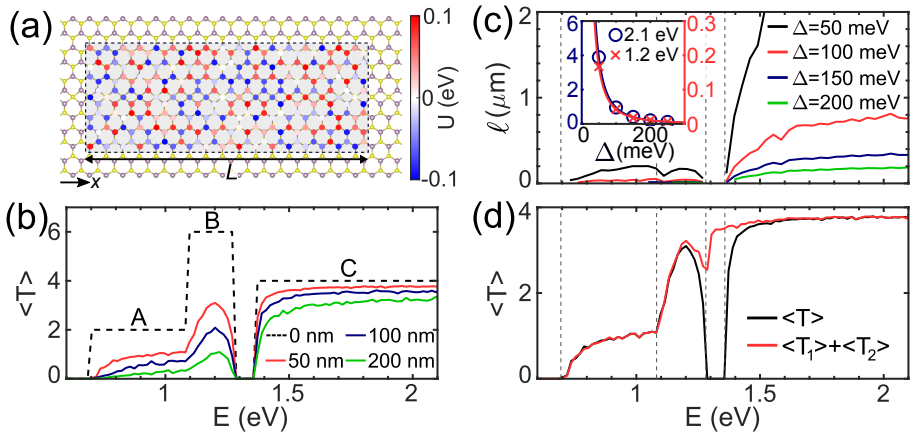

Figure 6.10: (a) Example of Anderson disorder realization with random on-site energies for the atoms over the section of length L, and with strength $\Delta = 100$ meV. The width of the disordered section around the MTB is 2 nm. (b) Average transmission coefficient as a function of the electron energy E for the MTB system in the pristine case ($L = 0$ nm) and in the presence of Anderson disorder with $\Delta = 100$ meV and L varying from 50 nm to 200 nm. The average is performed over 100 disorder realizations. (c) Mean free path ℓ as a function of the electron energy E for different Anderson disorder strengths Δ. The energies where we could not extract ℓ correspond to the energies close to the SOC-induced gap or where the transport regime is localized. Inset: mean free path as a function of Δ for two representative energies $E = 1.2$ eV and $E = 2.1$ eV. The continuous lines correspond to the fit $\propto \Delta^{-2}$. (d) Average transmission coefficient as a function of E for the MTB system in the presence of Anderson disorder with $\Delta = 100$ meV and $L = 50$ nm, and sum of the average transmission of the two MTB bands. $\langle T_1 \rangle$ is the average transmission of band ① contribution and $\langle T_2 \rangle$ is that of band ②.

the quasi-ballistic transport for L of the order of hundreds of nm ($L < \ell$) and in the diffusive regime for L of the order of a few μm.

To illustrate the scaling analysis performed to statistically analyze the transport regimes in the presence of Anderson disorder, we fix the disorder strength to $\Delta = 100$ meV, and we select two representative energies E=1 eV and E=1.8 eV. As shown in Fig. 6.10(b), at E=1 eV, $\langle T \rangle$ rapidly decreases when L increases. This suggests the transport regime is localized, as confirmed by the linear decrease of the average logarithm of the transmission coefficient $\langle \ln T \rangle$ as a function of L, see Fig. 6.11(a). The localization length is then extracted according to eq. (3.110), which gives $\xi = 58$ nm at the considered energy. Also, Fig. 6.11(b) shows the typical [179] Gaussian frequency distribution of $\ln T$ with $|\Delta \ln T \ / \ \langle \ln T \rangle| < 1$. At E=1.8 eV, $\langle T \rangle$ decreases more slowly for increasing L, thus suggesting a diffusive transport regime. This is confirmed by Fig. 6.11(c), which shows the inverse of the average transmission coefficient $\langle T \rangle$ as a function of the length L. Its linear scaling allows us to

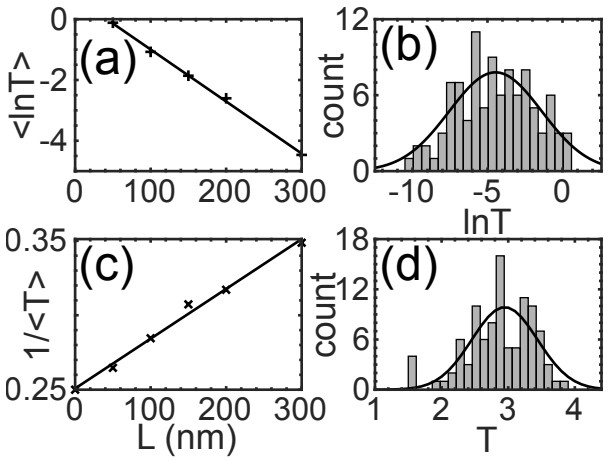

Figure 6.11: Scaling analysis of the transport regimes, localized (a-b) and diffusive regimes (c-d), for Anderson disorder with $\Delta = 100$ meV. (a) Average logarithm of the transmission coefficient as a function of L at $E = 1$ eV, which corresponds to the energy region A in Fig. 6.10 (b). The continuous line shows the linear fit. The estimated localization length is $\xi \approx 58$ nm. (b) Frequency distribution of $\ln T$ for $L = 300$ nm at the same energy. (c) Inverse of the average of the transmission coefficient as a function of L at $E = 1.8$ eV in the energy region C in Fig. 6.10 (b). The continuous line shows the linear fit. The estimated mean free path is $\ell \approx 750$ nm. (d) Frequency distribution of T for $L = 300$ nm at the same energy.

extract the mean free path according to eq. (3.109), which turns out to be $\ell = 750$ nm at the considered energy. Moreover, we observe the typical [179] Gaussian distribution with $\Delta T/\langle T \rangle < 1$, see Fig. 6.11(d).

The mean free path ℓ as a function of the energy E is reported in Fig. 6.10(c) for different disorder strengths Δ. The energies for which ℓ is not defined correspond to the SOC-induced gap or to regions where the transport regime is localized. The mean free path scaling with the Anderson disorder strength Δ is reported in the inset of Fig. 6.10(c) for two representative energies $E = 1.2$ eV and $E = 2.1$ eV (in regions B and C, respectively), where the transport regime is diffusive. We find that ℓ is inversely proportional to Δ^2 for both representative energies. Such a behavior is consistent with a weak scattering regime, where the Fermi golden rule is a good approximation and yields a scattering probability proportional to Δ^2.

The origin of the different behaviors observed in the three regions can be understood by noting that bands ① and ② contribute independently to the transport properties. Indeed, it is possible to separate band ① and band ②, by artificially modifying the Hamiltonian to shift alternatively one of the two bands at higher energy and isolate the contribution of the other. To this aim, we only modify the on-site energies of the specific d orbitals of the Mo atoms close to the MTB contributing to the states of the chosen band. To

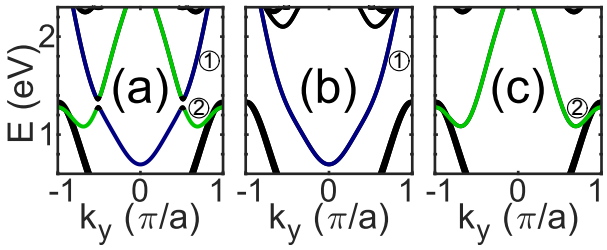

Figure 6.12: Separation of the MTB bands, ① (green lines) and ② (blue lines), by modification of the Hamiltonian. (a) Band structure without any modification for the ribbon of Fig. 6.7(b). (b) and (c) Band structures obtained by modification of the Hamiltonian for isolating band ① and band ②, respectively.

isolate the contribution to transport of band ①, band ② is shifted upward by increasing the on-site energies of the d_{xy} and the d_{z^2} orbitals by 0.5 eV and 2.0 eV, respectively. To isolate the contribution to transport of band ②, band ① is shifted upward by increasing the on-site energy of the d_{zx} orbital by 3.0 eV. The resulting modified band structures are reported in Fig. 6.12. Compared to the unmodified band structure shown in Fig. 6.12(a), only one band remains in its initial position, while the other one enters into the CB, thus not contributing to transport in the energy range of the bulk band gap, see Figs. 6.12(b) and (c).

Figure 6.10(d) demonstrates that the total average transmission is given by the sum of the average transmission of the two bands, i.e. $\langle T \rangle \approx \langle T_1 \rangle + \langle T_2 \rangle$, except, of course, around the SOC gap, where the two bands hybridize. This means that Anderson disorder does not introduce any significant scattering between these two bands with different orbital compositions, and that we can analyze each band independently. In the first energy region ($E \lesssim 1.1$ eV), the short mean free path and the transition to the localized transport regime are due to the fact that electrons are at the bottom of band ①. Therefore, Anderson disorder is more effective in inducing intraband scattering. At higher energies, in the region B and even more above the SOC gap, the wave number separation between counter-propagating states in band ① becomes larger, thus significantly tempering the backscattering. In the region B, band ② provides four conductive channels. However, again, the small separation in the BZ between counter-propagating states significantly enhances backscattering, especially close to the bands extrema, i.e. at the van Hove singularities. As a consequence, in this energy region the main contribution to transport comes from band ①. Analogously to what is observed for band ①, in region C above the SOC gap, the backscattering for the two conductive channels from band ② is strongly and progressively suppressed at higher energies. The resulting transmission coefficient is close to the ballistic case.

To provide a more detailed analysis, Fig. 6.13 reports the mean free path

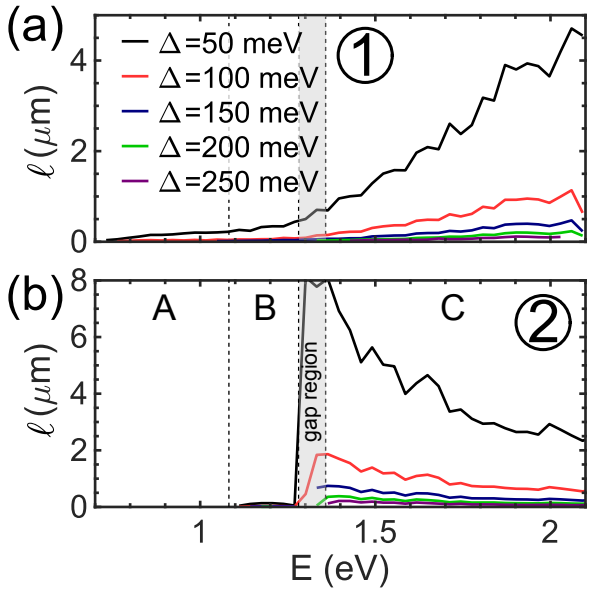

Figure 6.13: Mean free path as a function of the electron energy in the presence of Anderson disorder with strength Δ varying from 50 meV to 250 meV. The individual mean free paths of (a) band ① and (b) band ②, are calculated starting from the modified Hamiltonian corresponding to the band structures in Fig. 6.12(b) and Fig. 6.12(c), respectively.

of each band as a function of the energy E. At lower energies corresponding to regions A and B in Fig. 6.10(b), band ① exhibits a relatively large mean free path compared to ②. This behavior indicates the main contribution of band ① to transport. For higher energies above the SOC-induced gap, on the other hand, both bands are activated and contribute to the diffusive transport regime with relatively large mean free paths. The mean free path corresponding to band ① is shorter than for band ②, and it becomes longer for $E > 1.8$ eV.

Long-range disorder

We now consider the impact of long-range disorder, which corresponds to real-space potential energy fluctuations induced, for example, by the presence of charged impurities in the substrate underlying the 2D material. Adam *et al.* [189] proposed a model of the potential profile $U(\mathbf{r})$ for graphene as a random distribution of Gaussian long-range scatterers

$$U(\mathbf{r}) = \sum_{i=1}^{N} \epsilon_i e^{\frac{-(\mathbf{r}-\mathbf{R}_i)^2}{2\chi^2}} , \tag{6.2}$$

where i is the impurity index, $\mathbf{R}_i$ is its random position, ϵ_i is a randomly chosen potential energy that we select in the range [-Δ,Δ], N is the total number of Gaussian impurities and χ denotes the spatial range. Here, we consider

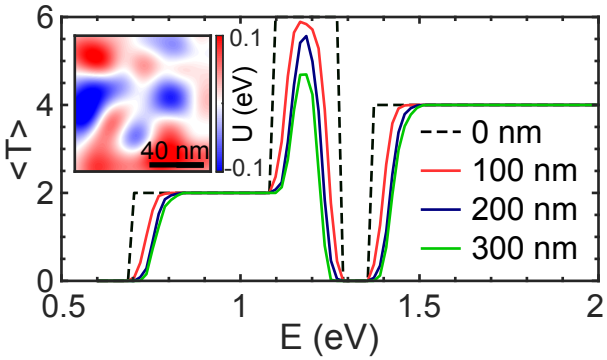

Figure 6.14: Main panel: Average transmission coefficient as a function of the energy and for different L in the case of a SiO_2 substrate. The averaging is performed over 100 disorder realizations. Inset: Example of long-range potential profile realization for a SiO_2 substrate.

two energy potential profiles corresponding to SiO_2 and hBN substrates. We adopt the parameters available in the literature for graphene [190], which are $\Delta = 50$ meV, $\chi = 10$ nm and $n = 10^{12}$ cm^{-2} for SiO_2, and $\Delta = 5$ meV, $\chi = 30$ nm and $n = 10^{11}$ cm^{-2} for hBN, where n is the density of impurities *per* surface area. These parameters may be different for MoS_2, due to the different screening properties compared to those of graphene. Nonetheless, this effective model provides a physical understanding of the impact of long-range disorder on the transport properties of MTBs.

The inset of Fig. 6.14 shows the potential profile reproducing the effect of the SiO_2 substrate. We consider such a potential to be active over a section of the system with length L. The transmission coefficient averaged over 100 different profile realizations for different L is reported in the main panel of Fig. 6.14. We observe a huge suppression of the transmission only close to edges of the transmission plateaus, where conductive channels are activated or deactivated. This behavior is explained by the fact that the long-range disorder induces local shifts of quasi-1D MTB states along the MTB. In particular, the band edges, which determine the activation of the conductive channels, are smoothly shifted all along the grain boundary. The regions with the highest and lowest shifts, which tend to be about $\pm\Delta$ for long enough L, determine the energy width of the decreased transmission region, as observed in the main panel of Fig. 6.14. For the hBN substrate, we do not observe any significant impact on the transport properties because of the extremely weak disorder strength Δ.

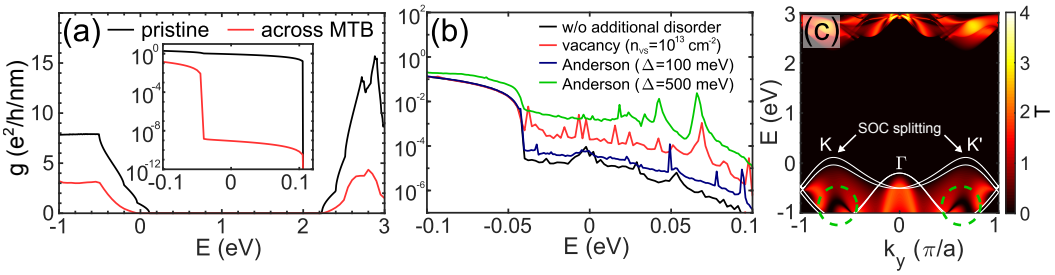

Figure 6.15: (a) Main panel: Zero-temperature conductance *per* unit of width as a function of the electron energy for pristine 2D MoS_2 and in the presence of a transverse MTB. Inset: Conductance at the top of the VB in logarithmic scale. (b) Zero-temperature conductance *per* unit of width at the top of the VB for 50 nm-wide MoS_2 ribbons with a transverse MTB in the absence (black line) and in the presence of short-range disorders in the region of the MTB, namely sulfur vacancies over an $L = 80$ nm-long section and Anderson disorder over a 2 nm-wide stripe surrounding the MTB with different strengths. In order to suppress edge contribution to the transmission, we introduced edge roughness. (c) Transmission coefficient as a function of the wave number and the electron energy for 2D MoS_2 with a transverse MTB. The white lines correspond to the band profile of 2D MoS_2, while the dashed circles indicate the strong suppression of transmission in the VB.

6.2.3 Transport across MTBs

We now report the degradation of the electronic transmission of a 2D MoS_2 layer in the presence of an MTB orthogonal to the transport x-direction, see the sketch in Fig. 6.6(b). Note that the system is periodic along the y-direction, which allows us to introduce the wave number k_y and, through the use of Bloch sums, to define the k_y-dependent Hamiltonian $H(k_y)$. We can thus calculate the transmission coefficient $T(E, k_y)$ for given energy E and wave number k_y, and obtain the zero-temperature conductance *per* unit of width by integration over the 1D BZ

$$g(E) \;=\; \frac{e^2}{h}\,\frac{1}{2\pi}\int_{\text{B.Z.}} T(E,k_y)\;dk_y\;. \tag{6.3}$$

Figure 6.15(a) compares the conductance *per* unit of width for pristine MoS_2 and in the presence of the MTB. Of course, there is no transmission in the energy region of the gap, since no state is available for injecting electrons. We observe a general degradation of the conductance with a more than 50% reduction.

Interestingly, as already observed in the literature [75], the conductance is completely suppressed over about 150 meV from the top of the VB, which corresponds to the SOC-induced splitting of the VB in 2D MoS_2 [29], see the inset of Fig. 6.15(a). In this energy region, in pristine 2D MoS_2 the top of the VB at K and K' points are oppositely spin-polarized, i.e. we have the so-

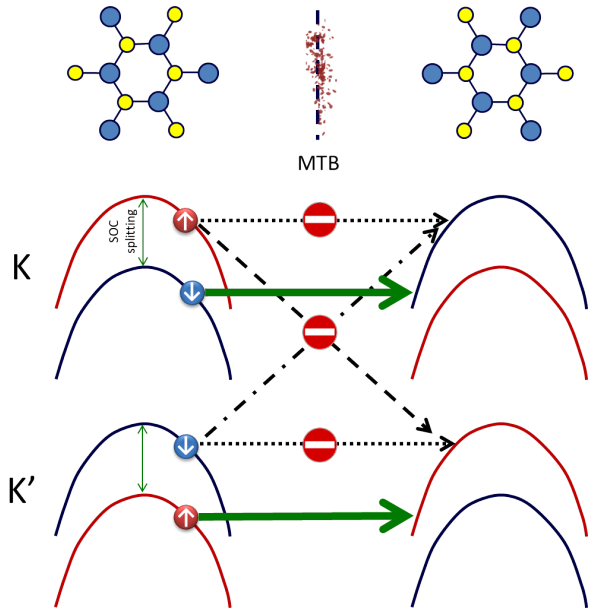

Figure 6.16: Top of the VB at the K and K' points on the two sides of the MTB. The SOC induces a splitting of the VBs at the K and K' points. Due to time reversal symmetry, the spin splitting is opposite at the two valleys. So, for energies at the top of the VB, we have the so called spin-valley locking. On the other side of the MTB, the lattice is rotated by 60°. As a consequence, also the BZ is rotated and the K and K' valleys are inverted. Therefore, the spin-valley polarization is inverted. In the spin-splitting energy region, just below the VB edge, intravalley transmission is forbidden due to spin conservation (dotted arrows). At the same time, intervalley transmission is forbidden by the system invariance under translations along the MTB (dashed arrows). Only at energies below the spin-splitting region, intravalley transmission is allowed (green arrows). This explains why the conductance is completely suppressed at the top of the VB, as seen in Fig. 6.15. However, if we include short-range disorder, indicated by the red dots along the MTB, intervalley scattering (along the dashed arrows) is allowed by the breaking of the translation symmetry, and the conductance increases as observed in Fig. 6.15(b).

called spin-valley locking, see Sec. 1.2.2 and the discussion in Sec. 5.2.6. In the presence of the MTB, opposite spin polarization at the K/K' valleys is reversed in the two grains on the two sides of the MTB due to the mirror reflection symmetry of the system. Therefore, as a consequence of spin preservation, the current can only flow in the presence of intervalley scattering, which is however suppressed due to the y-translation symmetry. This mechanism, illustrated in Fig. 6.16, results in the observed transport suppression [75]. The very small but finite (10^{-8}) residual transmission across the MTB, as shown in the inset of Fig. 6.15(a), can be considered as zero within the calculation accuracy.

We investigate the robustness of this phenomenon against short-range dis-

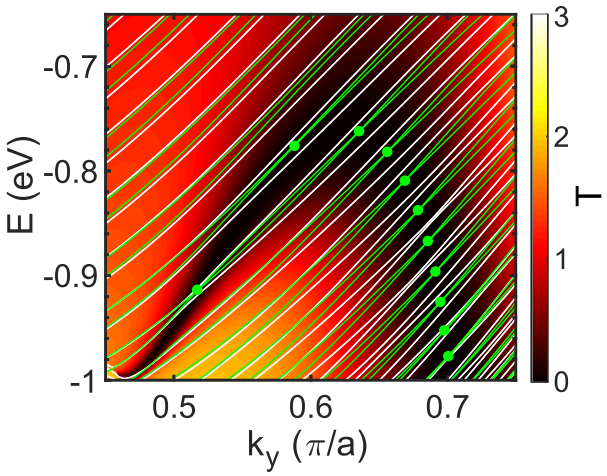

Figure 6.17: Transmission coefficient as a function of the wave number and the electron energy in one of the two regions indicated by dashed circles in Fig. 6.15(c). The band structure of a 20 nm-wide zigzag ribbon with a periodic MTB without (green lines) and with (white lines) SOC is superimposed.

order, which is expected to induce intervalley scattering and activate transport. To this aim, we consider a large ribbon ($W = 50$ nm) with edge roughness and an MTB across its section. Figure 6.15(b) shows that the conductance is still suppressed at the top of the VB, but there is a residual transmission due to intervalley scattering induced by the ribbon edges. Given the extremely small conductance, a residual contribution of edge state channels cannot be excluded. Note that, to be effective, intervalley scattering must occur at the grain boundary, where electrons pass from one grain to the other. Incidentally, at the top of the VB and within the same grain, intervalley scattering is suppressed by the spin-valley locking mechanism. The conductance increases when including Anderson disorder along the MTB (over a width of 2 nm), see Fig. 6.15(b), which strongly enhances intervalley scattering all along the grain boundary length. The conductance increase is larger for larger Anderson disorder strength Δ from 100 meV to 500 meV. A similar effect is observed in the presence of sulfur vacancies with density $n_{\mathrm{VS}} = 10^{13}$ cm^{-2}, whose extremely short-range nature entails a strong intervalley scattering. Note that our model does not consider the Hartree potential induced in the vicinity of MTB, whose estimation may be sensitive to the model details and which is expected to entail a further reduction of the transmission for energies close to the top of the VB [72], [75]. This choice does not affect our physical analysis.

A further insight into the results of Fig. 6.15(a) can be gained from the energy- and k_y-resolved transmission coefficient $T(E, k_y)$ reported in Fig. 6.15(c). This figure clearly shows the different contributions of the K/K' valleys, close to the sides of the BZ, and of the Γ valley at the center. The result confirms the

complete suppression of transport at energies between the two SOC-split topmost VBs. Surprisingly enough, we observe a strong suppression of $T(E, k_y)$ at low energies in the VB, as indicated by dashed circles. This behavior is related to the MTB effect of "cutting" the system into weakly coupled parts, as mentioned in Subsec. 6.2.1. A more detailed physical insight is obtained in terms of wave functions of the weakly coupled states. At the energies and wave numbers where $T(E, k_y)$ is suppressed, the coupling between the two parts of the system on the sides of the MTB is very small.

To support this interpretation, we superimpose the VBs of a 20 nm-wide zigzag ribbon with a periodic MTB to the transmission coefficient. At first, we do not consider SOC, see the green lines in Fig. 6.17. As discussed in Subsec. 6.2.1, the band structure is determined by the coupling of the subbands that reside on each side of the MTB. Since the coupling is weak, we observe couples of split bands. Where the bands cross, see the green dots in the figure, the coupling between the two regions at the sides of the MTB is vanishing. This explains why the low transmission coefficient is exactly observed at these crossing points. Note that increasing the width of the ribbon would just increase the number of the subbands and crowd the crossing points along the lowest transmission region (not shown here), thus confirming the validity of this picture in the 2D limit. Introducing the SOC, see the white lines in Fig. 6.17, makes the interpretation more convoluted due to the absence of the crossing points. This is because of the opposite spin-splitting energy on the states at two sides of the MTB for given K/K' valley, which again is consequence of the spin-valley locking mechanism and the mirror symmetry.

In conclusion of this subsection, we would like to point out that transport properties of the polycrystalline MoS_2 can be highly dependent on the density of the grain boundaries, which may cause a severe degradation of the conductivity. Controlling the density of grain boundaries will be a significant factor for the use in electronic applications [59].

6.3 Summary

In this Chapter, we have numerically investigated the transport properties of MoS_2 in the presence of an MTB. Along the grain boundary, conductive channels develop at energies within the band gap of 2D MoS_2. The conductance of these states is found to be sensitive to chalcogen vacancies, relatively robust against short-range Anderson disorder, and scarcely affected by long-range disorder. On the other side, transport across the MTB is significantly affected, and its analysis in terms of wave number dependent transmission reveals peculiar features of this grain boundary, as the separation of the ribbon into two weakly coupled narrower ribbons. Moreover, as already demonstrated in the literature [75], the transmission across the grain boundary is suppressed in the energy range of the spin-orbit splitting of the VB, due to spin-valley

locking. However, in the presence of short-range disorder, transmission is partially allowed as a consequence of the induced intervalley scattering. Our results provide physical and quantitative insight into the interplay between grain boundaries and additional disorder. They could thus be beneficial to the design of electronic devices based on TMDs, in particular for the control of leakage current in FETs and the fabrication of 2D metallic contacts based on grain boundary networks.

Chapter 7

Conclusions and perspectives

In this thesis, a thorough numerical study of the impact of various disorders on the transport properties of MoS_2, chosen as a paradigmatic TMD, was presented. The quantum transport simulations were based on an atomistic TB description calibrated, when necessary, with DFT results for a better accuracy, and on the Green's function techniques.

In Chapter 1, various properties, growth techniques, experimentally observed defects, and applications of TMDs were briefly introduced. The necessity of the theoretical and numerical study on the impact of disorders on electron transport in these materials emerged as a natural consequence of the experimentally observed low charge mobility.

On the methodological side, in Chapter 2, several models of Hamiltonian were thoroughly examined in order to identify the most appropriate to accurately reproduce the properties of TMDs and their defects. Most importantly, two different TB approaches, specifically the framework of the structural symmetries or the SK description, were reviewed in terms of their flexibility to describe the electronic properties. In particular, the SK description was found more adaptable to the description of disordered systems, where the presence lattice distortions can induce a spatial symmetry breaking, and was therefore chosen for the entire study of this thesis. Furthermore, the k·p model and DFT based Hamiltonian, and their limitations, in our context, compared to the TB model were discussed. The theoretical methodology of the Green's function formalism was presented in Chapter 3. The second quantization formalism, with the important introduction of the creation and annihilation operators, allowed us to define several other operators, as the local charge operator and the current operator, in terms of the Green's functions. Four relevant Green's functions were defined: the retarded and advanced Green's functions, which are related to the electronic structure, and the lesser and greater Green's functions, which contain information about the statistics of the system. For their efficient numerical evaluations, several methods were introduced, in particular the decimation-renormalization method for the extraction of the retarded

Green's function on a subsystem of interest. Similarly, the Keldysh theory allows one to obtain the out-of-equilibrium lesser and greater Green's functions in terms of those of the system at equilibrium. This is the key ingredient that allows the simulation of electron transport in biased systems. Most importantly, the explicit formulas for the electron current and the LDoS were derived in terms of the Green's functions. Their numerical implementation and the relative code structure were briefly described in Chapter 4.1, which notably reports how the layered structure was constructed in terms of the TB Hamiltonian. At the end of Chapter 3, the different quantum transport regimes (ballistic, quasi-ballistic, diffusive and localized) and their scaling theory were introduced. They turned out to be valuable tools for a qualitative and quantitative analysis of the simulation results.

The impact of two representative disorders was deeply investigated in this thesis. Chapter 5 reports on the impact of edge roughness on the quantum electron transport properties of MoS_2 nanoribbons. In the presence of edge roughness, the metallic edge states within the bulk gap tend to rapidly localize with an extremely small localization length, which indicates that the conductance of the metallic edge states is strongly suppressed. On the other hand, the electron transport outside the bulk gap was found to be moderately affected by edge roughness, and to show a diffusive transport regime with a rather large mean free path. This indicates that the effect of edge roughness for ribbons widths larger than 10 nm is compatible with their use in nanoelectronic applications, since the leakage current due to edge states would be suppressed without too much altering the on current. Ultra-narrow ribbons, however, were found to be more affected by edge roughness, particularly for energies close to the bulk gap edges according to the scaling of the mean free path.

In Chapter 6, one of the most commonly observed grain boundaries in experiments, MTB, was investigated. The MTB was found to support 1D metallic states at energies within the band gap of 2D MoS_2. We investigated the robustness of these states against several short-range and long-range disorders. The conductance along this MTB was found to be very sensitive to chalcogen vacancies. On the contrary, it turned out to be relatively robust against short-range Anderson disorder, and hardly affected by long-range disorder. Besides, the transport across the MTB in 2D MoS_2 was investigated. In the presence of the transverse MTB, the conductance is strongly suppressed, particularly for the energies close to the top of the VB where the spin-orbit splitting is observed. This behavior follows from the spin-valley locking, which is due to the inverted spin-valley polarization in the grains at the two sides of the MTB. However, we found that the presence of short-range disorder partially allowed the transmission due to the induced intervalley scattering. This study gives a physical insight into the interplay between grain boundaries and additional disorder. We expect that it could be helpful in the design of large-scale electronic devices based on TMDs, especially for the control

of leakage current in polycrystalline TMDs and potential use of MTB-based metallic contacts.

In conclusion, the theoretical and numerical results presented in this thesis provide a physical understanding of the impact of various disorders on the transport properties of TMDs, including the interplay with SOC. Most importantly, the statistical analysis in terms of the transport regimes and relative scaling lengths allowed a quantitative insight into the role of disorder, which could guide the design of TMD-based devices.

The methodology adopted and developed in this thesis, especially concerning the Hamiltonian calibration, could be easily employed for the investigation of different 2D materials of technological interest and other sources of disorder. In particular, chemical impurities and dislocations could be deleterious for short-channel or tunnel FETs due to the formation of midgap states. Finally, some elements of the present work suggest that the research could be profitably extended toward the study of spin transport in disorder TMDs.

Bibliography

[1] K. S. Novoselov, A. K. Geim, S. V. Morozov, D. Jiang, Y. Zhang, S. V. Dubonos, I. V. Grigorieva, and A. A. Firsov, "Electric Field Effect in Atomically Thin Carbon Films," *Science*, vol. 306, no. 5696, pp. 666–669, 2004, ISSN: 0036-8075. DOI: 10.1126/science.1102896.

[2] F. Pulizzi, O. Bubnova, S. Milana, D. Schilter, D. Abergel, and A. Moscatelli, "Graphene in the making," *Nature Nanotechnology*, vol. 14, no. 10, pp. 914–918, 2019. DOI: 10.1038/s41565-019-0552-5.

[3] A. H. C. Neto, F. Guinea, N. M. R. Peres, K. S. Novoselov, and A. K. Geim, "The electronic properties of graphene," *Reviews of Modern Physics*, vol. 81, no. 1, pp. 109–162, 2009. DOI: 10.1103/revmodphys.81.109.

[4] K. S. Novoselov, D. Jiang, F. Schedin, T. J. Booth, V. V. Khotkevich, S. V. Morozov, and A. K. Geim, "Two-dimensional atomic crystals," *Proceedings of the National Academy of Sciences*, vol. 102, no. 30, pp. 10 451–10 453, 2005. DOI: 10.1073/pnas.0502848102.

[5] F. Schwierz, "Graphene transistors," *Nature Nanotechnology*, vol. 5, no. 7, pp. 487–496, 2010. DOI: 10.1038/nnano.2010.89.

[6] W. Han, R. K. Kawakami, M. Gmitra, and J. Fabian, "Graphene spintronics," *Nature Nanotechnology*, vol. 9, no. 10, pp. 794–807, 2014. DOI: 10.1038/nnano.2014.214.

[7] S. Roche, J. Åkerman, B. Beschoten, J.-C. Charlier, M. Chshiev, S. P. Dash, B. Dlubak, J. Fabian, A. Fert, M. Guimarães, F. Guinea, I. Grigorieva, C. Schönenberger, P. Seneor, C. Stampfer, S. O. Valenzuela, X. Waintal, and B. van Wees, "Graphene spintronics: The European Flagship perspective," *2D Materials*, vol. 2, no. 3, p. 030 202, 2015. DOI: 10.1088/2053-1583/2/3/030202.

[8] Y. Cao, V. Fatemi, S. Fang, K. Watanabe, T. Taniguchi, E. Kaxiras, and P. Jarillo-Herrero, "Unconventional superconductivity in magic-angle graphene superlattices," *Nature*, vol. 556, no. 7699, pp. 43–50, 2018. DOI: 10.1038/nature26160.

[9] P. Miró, M. Audiffred, and T. Heine, "An atlas of two-dimensional materials," *Chemical Society Reviews*, vol. 43, no. 18, pp. 6537–6554, 2014. DOI: 10.1039/c4cs00102h.

[10] G. Fiori, F. Bonaccorso, G. Iannaccone, T. Palacios, D. Neumaier, A. Seabaugh, S. K. Banerjee, and L. Colombo, "Electronics based on two-dimensional materials," *Nature Nanotechnology*, vol. 9, no. 10, pp. 768–779, 2014. DOI: 10.1038/nnano.2014.207.

[11] F. Schwierz, J. Pezoldt, and R. Granzner, "Two-dimensional materials and their prospects in transistor electronics," *Nanoscale*, vol. 7, no. 18, pp. 8261–8283, 2015. DOI: 10.1039/c5nr01052g.

[12] Q. H. Wang, K. Kalantar-Zadeh, A. Kis, J. N. Coleman, and M. S. Strano, "Electronics and optoelectronics of two-dimensional transition metal dichalcogenides," *Nature Nanotechnology*, vol. 7, no. 11, pp. 699–712, 2012. DOI: 10.1038/nnano.2012.193.

[13] F. Giannazzo, G. Greco, F. Roccaforte, and S. Sonde, "Vertical Transistors Based on 2D Materials: Status and Prospects," *Crystals*, vol. 8, no. 2, p. 70, 2018. DOI: 10.3390/cryst8020070.

[14] B. Radisavljevic, A. Radenovic, J. Brivio, V. Giacometti, and A. Kis, "Single-layer MoS_2 transistors," *Nature Nanotechnology*, vol. 6, no. 3, pp. 147–150, 2011. DOI: 10.1038/nnano.2010.279.

[15] S. Wachter, D. K. Polyushkin, O. Bethge, and T. Mueller, "A microprocessor based on a two-dimensional semiconductor," *Nature Communications*, vol. 8, p. 14 948, 2017. DOI: 10.1038/ncomms14948.

[16] S. Manzeli, D. Ovchinnikov, D. Pasquier, O. V. Yazyev, and A. Kis, "2d transition metal dichalcogenides," *Nature Reviews Materials*, vol. 2, no. 8, p. 17 033, 2017. DOI: 10.1038/natrevmats.2017.33.

[17] X. Qian, J. Liu, L. Fu, and J. Li, "Quantum spin hall effect in two-dimensional transition metal dichalcogenides," *Science*, vol. 346, no. 6215, pp. 1344–1347, 2014. DOI: 10.1126/science.1256815.

[18] L. F. Mattheiss, "Band structures of transition-metal-dichalcogenide layer compounds," *Physical Review B*, vol. 8, no. 8, pp. 3719–3740, 1973. DOI: 10.1103/physrevb.8.3719.

[19] F. Wypych and R. Schöllhorn, "1t-MoS_2, a new metallic modification of molybdenum disulfide," *Journal of the Chemical Society, Chemical Communications*, no. 19, pp. 1386–1388, 1992. DOI: 10.1039/c39920001386.

[20] R. Bissessur, M. G. Kanatzidis, J. L. Schindler, and C. R. Kannewurf, "Encapsulation of polymers into MoS_2 and metal to insulator transition in metastable MoS_2," *Journal of the Chemical Society, Chemical Communications*, no. 20, p. 1582, 1993. DOI: 10.1039/c39930001582.

[21] M. A. Py and R. R. Haering, "Structural destabilization induced by lithium intercalation in MoS_2 and related compounds," *Canadian Journal of Physics*, vol. 61, no. 1, pp. 76–84, 1983. DOI: 10.1139/p83-013.

[22] X. Cui, G.-H. Lee, Y. D. Kim, G. Arefe, P. Y. Huang, C.-H. Lee, D. A. Chenet, X. Zhang, L. Wang, F. Ye, F. Pizzocchero, B. S. Jessen, K. Watanabe, T. Taniguchi, D. A. Muller, T. Low, P. Kim, and J. Hone, "Multi-terminal transport measurements of MoS_2 using a van der Waals heterostructure device platform," *Nature Nanotechnology*, vol. 10, no. 6, pp. 534–540, 2015. DOI: 10.1038/nnano.2015.70.

[23] L. Yu, Y.-H. Lee, X. Ling, E. J. G. Santos, Y. C. Shin, Y. Lin, M. Dubey, E. Kaxiras, J. Kong, H. Wang, and T. Palacios, "Graphene/MoS_2 Hybrid Technology for Large-Scale Two-Dimensional Electronics," *Nano Letters*, vol. 14, no. 6, pp. 3055–3063, 2014. DOI: 10.1021/nl404795z.

[24] R. A. Bromley, R. B. Murray, and A. D. Yoffe, "The band structures of some transition metal dichalcogenides. III. group VIA: Trigonal prism materials," *Journal of Physics C: Solid State Physics*, vol. 5, no. 7, pp. 759–778, 1972. DOI: 10.1088/0022-3719/5/7/007.

[25] Z. Y. Zhu, Y. C. Cheng, and U. Schwingenschlögl, "Giant spin-orbit-induced spin splitting in two-dimensional transition-metal dichalcogenide semiconductors," *Physical Review B*, vol. 84, no. 15, p. 153 402, 2011. DOI: 10.1103/physrevb.84.153402.

[26] Q. Yue, J. Kang, Z. Shao, X. Zhang, S. Chang, G. Wang, S. Qin, and J. Li, "Mechanical and electronic properties of monolayer MoS_2 under elastic strain," *Physics Letters A*, vol. 376, no. 12-13, pp. 1166–1170, 2012. DOI: 10.1016/j.physleta.2012.02.029.

[27] E. S. Kadantsev and P. Hawrylak, "Electronic structure of a single MoS_2 monolayer," *Solid State Communications*, vol. 152, no. 10, pp. 909–913, 2012. DOI: 10.1016/j.ssc.2012.02.005.

[28] F. Zahid, L. Liu, Y. Zhu, J. Wang, and H. Guo, "A generic tight-binding model for monolayer, bilayer and bulk MoS_2," *AIP Advances*, vol. 3, no. 5, p. 052 111, 2013. DOI: 10.1063/1.4804936.

[29] E. Ridolfi, D. Le, T. S. Rahman, E. R. Mucciolo, and C. H. Lewenkopf, "A Tight-Binding Model For MoS_2 Monolayers," *Journal of Physics: Condensed Matter*, vol. 27, no. 36, p. 365 501, 2015. DOI: 10.1088/0953-8984/27/36/365501.

[30] K. F. Mak, C. Lee, J. Hone, J. Shan, and T. F. Heinz, "Atomically Thin MoS_2: A new direct-gap semiconductor," *Physical Review Letters*, vol. 105, no. 13, p. 136 805, 2010. DOI: 10.1103/physrevlett.105.136805.

[31] A. Splendiani, L. Sun, Y. Zhang, T. Li, J. Kim, C.-Y. Chim, G. Galli, and F. Wang, "Emerging photoluminescence in monolayer MoS_2," *Nano Letters*, vol. 10, no. 4, pp. 1271–1275, 2010. DOI: 10.1021/nl903868w.

[32] C. Zhang, A. Johnson, C.-L. Hsu, L.-J. Li, and C.-K. Shih, "Direct imaging of band profile in single layer MoS_2 on graphite: Quasiparticle energy gap, metallic edge states, and edge band bending," *Nano Letters*, vol. 14, no. 5, pp. 2443–2447, 2014. DOI: 10.1021/nl501133c.

[33] A. Ramirez-Torres, D. Le, and T. S. Rahman, "Effect of monolayer supports on the electronic structure of single-layer MoS_2," *IOP Conference Series: Materials Science and Engineering*, vol. 76, p. 012 011, 2015. DOI: 10.1088/1757-899x/76/1/012011.

[34] J. Mann, Q. Ma, P. M. Odenthal, M. Isarraraz, D. Le, E. Preciado, D. Barroso, K. Yamaguchi, G. von Son Palacio, A. Nguyen, T. Tran, M. Wurch, A. Nguyen, V. Klee, S. Bobek, D. Sun, T. F. Heinz, T. S. Rahman, R. Kawakami, and L. Bartels, "2-dimensional transition metal dichalcogenides with tunable direct band gaps: MoS2$(1-x)$Se2x monolayers," *Advanced Materials*, vol. 26, no. 9, pp. 1399–1404, 2013. DOI: 10.1002/adma.201304389.

[35] J. Heyd, G. E. Scuseria, and M. Ernzerhof, "Hybrid functionals based on a screened coulomb potential," *The Journal of Chemical Physics*, vol. 118, no. 18, pp. 8207–8215, 2003. DOI: 10.1063/1.1564060.

[36] D. Y. Qiu, F. H. da Jornada, and S. G. Louie, "Optical spectrum of MoS_2: Many-body effects and diversity of exciton states," *Physical Review Letters*, vol. 111, no. 21, p. 216 805, 2013. DOI: 10.1103/physrevlett.111.216805.

[37] P. A. Maksym and H. Aoki, "Complete spin and valley polarization by total external reflection from potential barriers in bilayer graphene and monolayer transition metal dichalcogenides," *arXiv:1911.03077v2*, 2019.

[38] S. Z. Butler, S. M. Hollen, L. Cao, Y. Cui, J. A. Gupta, H. R. Gutiérrez, T. F. Heinz, S. S. Hong, J. Huang, A. F. Ismach, E. Johnston-Halperin, M. Kuno, V. V. Plashnitsa, R. D. Robinson, R. S. Ruoff, S. Salahuddin, J. Shan, L. Shi, M. G. Spencer, M. Terrones, W. Windl, and J. E. Goldberger, "Progress, challenges, and opportunities in two-dimensional materials beyond graphene," *ACS Nano*, vol. 7, no. 4, pp. 2898–2926, 2013. DOI: 10.1021/nn400280c.

[39] F. A. Rasmussen and K. S. Thygesen, "Computational 2d materials database: Electronic structure of transition-metal dichalcogenides and oxides," *The Journal of Physical Chemistry C*, vol. 119, no. 23, pp. 13 169–13 183, 2015. DOI: 10.1021/acs.jpcc.5b02950.

[40] W. Zhang, Z. Huang, W. Zhang, and Y. Li, "Two-dimensional semiconductors with possible high room temperature mobility," *Nano Research*, vol. 7, no. 12, pp. 1731–1737, 2014. DOI: 10.1007/s12274-014-0532-x.

[41] H. Wang, L. Yu, Y.-H. Lee, Y. Shi, A. Hsu, M. L. Chin, L.-J. Li, M. Dubey, J. Kong, and T. Palacios, "Integrated circuits based on bilayer MoS_2 transistors," *Nano Letters*, vol. 12, no. 9, pp. 4674–4680, 2012. DOI: 10.1021/nl302015v.

[42] G. Wang, J. Zhang, S. Yang, F. Wang, X. Zhuang, K. Müllen, and X. Feng, "Vertically aligned MoS_2 nanosheets patterned on electrochemically exfoliated graphene for high-performance lithium and sodium storage," *Advanced Energy Materials*, vol. 8, no. 8, p. 1 702 254, 2017. DOI: 10.1002/aenm.201702254.

[43] D. Ovchinnikov, A. Allain, Y.-S. Huang, D. Dumcenco, and A. Kis, "Electrical transport properties of single-layer WS_2," *ACS Nano*, vol. 8, no. 8, pp. 8174–8181, 2014. DOI: 10.1021/nn502362b.

[44] E. Gao, S.-Z. Lin, Z. Qin, M. J. Buehler, X.-Q. Feng, and Z. Xu, "Mechanical exfoliation of two-dimensional materials," *Journal of the Mechanics and Physics of Solids*, vol. 115, pp. 248–262, 2018. DOI: 10.1016/j.jmps.2018.03.014.

[45] A. J. Mannix, B. Kiraly, M. C. Hersam, and N. P. Guisinger, "Synthesis and chemistry of elemental 2d materials," *Nature Reviews Chemistry*, vol. 1, no. 2, p. 0014, 2017. DOI: 10.1038/s41570-016-0014.

[46] C. R. Dean, A. F. Young, I. Meric, C. Lee, L. Wang, S. Sorgenfrei, K. Watanabe, T. Taniguchi, P. Kim, K. L. Shepard, and J. Hone, "Boron nitride substrates for high-quality graphene electronics," *Nature Nanotechnology*, vol. 5, no. 10, pp. 722–726, 2010. DOI: 10.1038/nnano.2010.172.

[47] A. K. Geim, "Graphene: Status and prospects," *Science*, vol. 324, no. 5934, pp. 1530–1534, 2009. DOI: 10.1126/science.1158877.

[48] J. N. Coleman, M. Lotya, A. O'Neill, S. D. Bergin, P. J. King, U. Khan, K. Young, A. Gaucher, S. De, R. J. Smith, I. V. Shvets, S. K. Arora, G. Stanton, H.-Y. Kim, K. Lee, G. T. Kim, G. S. Duesberg, T. Hallam, J. J. Boland, J. J. Wang, J. F. Donegan, J. C. Grunlan, G. Moriarty, A. Shmeliov, R. J. Nicholls, J. M. Perkins, E. M. Grieveson, K. Theuwissen, D. W. McComb, P. D. Nellist, and V. Nicolosi, "Two-dimensional nanosheets produced by liquid exfoliation of layered materials," *Science*, vol. 331, no. 6017, pp. 568–571, 2011. DOI: 10.1126/science.1194975.

[49] G. Cunningham, M. Lotya, C. S. Cucinotta, S. Sanvito, S. D. Bergin, R. Menzel, M. S. P. Shaffer, and J. N. Coleman, "Solvent exfoliation of transition metal dichalcogenides: Dispersibility of exfoliated nanosheets varies only weakly between compounds," *ACS Nano*, vol. 6, no. 4, pp. 3468–3480, 2012. DOI: 10.1021/nn300503e.

[50] M. Lotya, P. J. King, U. Khan, S. De, and J. N. Coleman, "High-concentration, surfactant-stabilized graphene dispersions," *ACS Nano*, vol. 4, no. 6, pp. 3155–3162, 2010. DOI: 10.1021/nn1005304.

[51] G. Eda, H. Yamaguchi, D. Voiry, T. Fujita, M. Chen, and M. Chhowalla, "Photoluminescence from chemically exfoliated MoS_2," *Nano Letters*, vol. 11, no. 12, pp. 5111–5116, 2011. DOI: 10.1021/nl201874w.

[52] F. Torrisi, T. Hasan, W. Wu, Z. Sun, A. Lombardo, T. S. Kulmala, G.-W. Hsieh, S. Jung, F. Bonaccorso, P. J. Paul, D. Chu, and A. C. Ferrari, "Inkjet-printed graphene electronics," *ACS Nano*, vol. 6, no. 4, pp. 2992–3006, 2012. DOI: 10.1021/nn2044609.

[53] R. Worsley, L. Pimpolari, D. McManus, N. Ge, R. Ionescu, J. A. Wittkopf, A. Alieva, G. Basso, M. Macucci, G. Iannaccone, K. S. Novoselov, H. Holder, G. Fiori, and C. Casiraghi, "All-2d material inkjet-printed capacitors: Toward fully printed integrated circuits," *ACS Nano*, vol. 13, no. 1, pp. 54–60, 2018. DOI: 10.1021/acsnano.8b06464.

[54] A. M. van der Zande, P. Y. Huang, D. A. Chenet, T. C. Berkelbach, Y. You, G.-H. Lee, T. F. Heinz, D. R. Reichman, D. A. Muller, and J. C. Hone, "Grains and grain boundaries in highly crystalline monolayer molybdenum disulphide," *Nature Materials*, vol. 12, no. 6, pp. 554–561, 2013. DOI: 10.1038/nmat3633.

[55] S. Najmaei, Z. Liu, W. Zhou, X. Zou, G. Shi, S. Lei, B. I. Yakobson, J.-C. Idrobo, P. M. Ajayan, and J. Lou, "Vapour phase growth and grain boundary structure of molybdenum disulphide atomic layers," *Nature Materials*, vol. 12, no. 8, pp. 754–759, 2013. DOI: 10.1038/nmat3673.

[56] W. Zhou, X. Zou, S. Najmaei, Z. Liu, Y. Shi, J. Kong, J. Lou, P. M. Ajayan, B. I. Yakobson, and J.-C. Idrobo, "Intrinsic Structural Defects in Monolayer Molybdenum Disulfide," *Nano Letters*, vol. 13, no. 6, pp. 2615–2622, 2013. DOI: 10.1021/nl4007479.

[57] Y. Zhou, S. G. Sarwat, G. S. Jung, M. J. Buehler, H. Bhaskaran, and J. H. Warner, "Grain Boundaries as Electrical Conduction Channels in Polycrystalline Monolayer WS_2," *ACS Applied Materials & Interfaces*, vol. 11, no. 10, pp. 10 189–10 197, 2019. DOI: 10.1021/acsami.8b21391.

[58] K. Hsieh, V. Kochat, X. Zhang, Y. Gong, C. S. Tiwary, P. M. Ajayan, and A. Ghosh, "Effect of Carrier Localization on Electrical Transport and Noise at Individual Grain Boundaries in Monolayer MoS_2," *Nano Letters*, vol. 17, no. 9, pp. 5452–5457, 2017. DOI: 10.1021/acs.nanolett.7b02099.

[59] S. Najmaei, M. Amani, M. L. Chin, Z. Liu, A. G. Birdwell, T. P. O'Regan, P. M. Ajayan, M. Dubey, and J. Lou, "Electrical Transport Properties of Polycrystalline Monolayer Molybdenum Disulfide," *ACS Nano*, vol. 8, no. 8, pp. 7930–7937, 2014. DOI: 10.1021/nn501701a.

[60] T. H. Ly, D. J. Perello, J. Zhao, Q. Deng, H. Kim, G. H. Han, S. H. Chae, H. Y. Jeong, and Y. H. Lee, "Misorientation-angle-dependent electrical transport across molybdenum disulfide grain boundaries," *Nature Communications*, vol. 7, no. 1, p. 10 426, 2016. DOI: 10.1038/ncomms10426.

[61] Z. Yu, Y. Pan, Y. Shen, Z. Wang, Z.-Y. Ong, T. Xu, R. Xin, L. Pan, B. Wang, L. Sun, J. Wang, G. Zhang, Y. W. Zhang, Y. Shi, and X. Wang, "Towards intrinsic charge transport in monolayer molybdenum disulfide by defect and interface engineering," *Nature Communications*, vol. 5, no. 1, p. 5290, 2014. DOI: 10.1038/ncomms6290.

[62] S. Vishwanath, X. Liu, S. Rouvimov, P. C. Mende, A. Azcatl, S. McDonnell, R. M. Wallace, R. M. Feenstra, J. K. Furdyna, D. Jena, and H. G. Xing, "Comprehensive structural and optical characterization of MBE grown MoSe 2 on graphite, CaF 2 and graphene," *2D Materials*, vol. 2, no. 2, p. 024 007, 2015. DOI: 10.1088/2053-1583/2/2/024007.

[63] R. Yue, Y. Nie, L. A. Walsh, R. Addou, C. Liang, N. Lu, A. T. Barton, H. Zhu, Z. Che, D. Barrera, L. Cheng, P.-R. Cha, Y. J. Chabal, J. W. P. Hsu, J. Kim, M. J. Kim, L. Colombo, R. M. Wallace, K. Cho, and C. L. Hinkle, "Nucleation and growth of WSe 2 : Enabling large grain transition metal dichalcogenides," *2D Materials*, vol. 4, no. 4, p. 045 019, 2017. DOI: 10.1088/2053-1583/aa8ab5.

[64] H. C. Diaz, Y. Ma, R. Chaghi, and M. Batzill, "High density of (pseudo) periodic twin-grain boundaries in molecular beam epitaxy-grown van der Waals heterostructure: $MoTe_2/MoS_2$," *Applied Physics Letters*, vol. 108, no. 19, p. 191 606, 2016. DOI: 10.1063/1.4949559.

[65] L. A. Walsh, R. Yue, Q. Wang, A. T. Barton, R. Addou, C. M. Smyth, H. Zhu, J. Kim, L. Colombo, M. J. Kim, R. M. Wallace, and C. L. Hinkle, "Wte2 thin films grown by beam-interrupted molecular beam epitaxy," *2D Materials*, vol. 4, no. 2, p. 025 044, 2017. DOI: 10.1088/2053-1583/aa61e1.

[66] Y. Ma, S. Kolekar, H. C. Diaz, J. Aprojanz, I. Miccoli, C. Tegenkamp, and M. Batzill, "Metallic Twin Grain Boundaries Embedded in $MoSe_2$ Monolayers Grown by Molecular Beam Epitaxy," *ACS Nano*, vol. 11, no. 5, pp. 5130–5139, 2017. DOI: 10.1021/acsnano.7b02172.

[67] S. McDonnell, R. Addou, C. Buie, R. M. Wallace, and C. L. Hinkle, "Defect-dominated doping and contact resistance in MoS_2," *ACS Nano*, vol. 8, no. 3, pp. 2880–2888, 2014. DOI: 10.1021/nn500044q.

[68] D. Edelberg, D. Rhodes, A. Kerelsky, B. Kim, J. Wang, A. Zangiabadi, C. Kim, A. Abhinandan, J. Ardelean, M. Scully, D. Scullion, L. Embon, R. Zu, E. J. G. Santos, L. Balicas, C. Marianetti, K. Barmak, X. Zhu, J. Hone, and A. N. Pasupathy, "Approaching the intrinsic limit in transition metal diselenides via point defect control," *Nano Letters*, vol. 19, no. 7, pp. 4371–4379, 2019. DOI: 10.1021/acs.nanolett.9b00985.

[69] J. Hong, Z. Hu, M. Probert, K. Li, D. Lv, X. Yang, L. Gu, N. Mao, Q. Feng, L. Xie, J. Zhang, D. Wu, Z. Zhang, C. Jin, W. Ji, X. Zhang, J. Yuan, and Z. Zhang, "Exploring atomic defects in molybdenum disulphide monolayers," *Nature Communications*, vol. 6, no. 1, p. 6293, 2015. DOI: 10.1038/ncomms7293.

[70] M. Amani, D.-H. Lien, D. Kiriya, J. Xiao, A. Azcatl, J. Noh, S. R. Madhvapathy, R. Addou, S. KC, M. Dubey, K. Cho, R. M. Wallace, S.-C. Lee, J.-H. He, J. W. Ager, X. Zhang, E. Yablonovitch, and A. Javey, "Near-unity photoluminescence quantum yield in MoS_2," *Science*, vol. 350, no. 6264, pp. 1065–1068, 2015. DOI: 10.1126/science.aad2114.

[71] H. Liu, L. Jiao, F. Yang, Y. Cai, X. Wu, W. Ho, C. Gao, J. Jia, N. Wang, H. Fan, W. Yao, and M. Xie, "Dense network of one-dimensional midgap metallic modes in monolayer $MoSe_2$ and their spatial undulations," *Physical Review Letters*, vol. 113, no. 6, p. 066 105, 2014. DOI: 10.1103/physrevlett.113.066105.

[72] O. Lehtinen, H.-P. Komsa, A. Pulkin, M. B. Whitwick, M.-W. Chen, T. Lehnert, M. J. Mohn, O. V. Yazyev, A. Kis, U. Kaiser, and A. V. Krasheninnikov, "Atomic Scale Microstructure and Properties of Se-Deficient Two-Dimensional $MoSe_2$," *ACS Nano*, vol. 9, no. 3, pp. 3274–3283, 2015. DOI: 10.1021/acsnano.5b00410.

[73] X. Zou, Y. Liu, and B. I. Yakobson, "Predicting Dislocations and Grain Boundaries in Two-Dimensional Metal-Disulfides from the First Principles," *Nano Letters*, vol. 13, no. 1, pp. 253–258, 2013. DOI: 10.1021/nl3040042.

[74] M. Ghorbani-Asl, A. N. Enyashin, A. Kuc, G. Seifert, and T. Heine, "Defect-induced conductivity anisotropy in MoS_2 monolayers," *Physical Review B*, vol. 88, no. 24, p. 245 440, 2013. DOI: 10.1103/physrevb.88.245440.

[75] A. Pulkin and O. V. Yazyev, "Spin- and valley-polarized transport across line defects in monolayer MoS_2," *Physical Review B*, vol. 93, no. 4, p. 041 419, 2016. DOI: 10.1103/physrevb.93.041419.

[76] G. E. Moore, "Cramming more components onto integrated circuits," *Electronics*, vol. 38, no. 8, p. 114, 1965.

[77] *International Technology Roadmap for Semiconductors*, http://www.itrs2.net/. [Online]. Available: http://www.itrs2.net/.

[78] *International Roadmap for Devices and Systems*, https://irds.ieee.org. [Online]. Available: https://irds.ieee.org.

[79] A. Lherbier, M. P. Persson, Y.-M. Niquet, F. Triozon, and S. Roche, "Quantum transport length scales in silicon-based semiconducting nanowires: Surface roughness effects," *Physical Review B*, vol. 77, no. 8, p. 085 301, 2008. DOI: 10.1103/physrevb.77.085301.

[80] A. Cresti, M. G. Pala, S. Poli, M. Mouis, and G. Ghibaudo, "A comparative study of surface-roughness-induced variability in silicon nanowire and double-gate FETs," *IEEE Transactions on Electron Devices*, vol. 58, no. 8, p. 2274, 2011. DOI: 10.1109/ted.2011.2147318.

[81] Y. Chen, P. Cui, X. Ren, C. Zhang, C. Jin, Z. Zhang, and C.-K. Shih, "Fabrication of $MoSe_2$ nanoribbons via an unusual morphological phase transition," *Nature Communications*, vol. 8, p. 15 135, 2017. DOI: 10.1038/ncomms15135.

[82] L. Liu, Y. Lu, and J. Guo, "On Monolayer MoS_2 Field-Effect Transistors at the Scaling Limit," *IEEE Transactions on Electron Devices*, vol. 60, no. 12, pp. 4133–4139, 2013. DOI: 10.1109/ted.2013.2284591.

[83] M. Yagmurcukardes, F. M. Peeters, R. T. Senger, and H. Sahin, "Nanoribbons: From fundamentals to state-of-the-art applications," *Applied Physics Reviews*, vol. 3, no. 4, p. 041 302, 2016. DOI: 10.1063/1.4966963.

[84] Q. Li, E. C. Walter, W. E. van der Veer, B. J. Murray, J. T. Newberg, E. W. Bohannan, J. A. Switzer, J. C. Hemminger, and R. M. Penner, "Molybdenum Disulfide Nanowires and Nanoribbons by Electrochemical/Chemical Synthesis," *The Journal of Physical Chemistry B*, vol. 109, no. 8, pp. 3169–3182, 2005. DOI: 10.1021/jp045032d.

[85] X. Liu, T. Xu, X. Wu, Z. Zhang, J. Yu, H. Qiu, J.-H. Hong, C.-H. Jin, J.-X. Li, X.-R. Wang, L.-T. Sun, and W. Guo, "Top–down fabrication of sub-nanometre semiconducting nanoribbons derived from molybdenum disulfide sheets," *Nature Communications*, vol. 4, p. 1776, 2013. DOI: 10.1038/ncomms2803.

[86] Z. Wang, H. Li, Z. Liu, Z. Shi, J. Lu, K. Suenaga, S.-K. Joung, T. Okazaki, Z. Gu, J. Zhou, Z. Gao, G. Li, S. Sanvito, E. Wang, and S. Iijima, "Mixed Low-Dimensional Nanomaterial: 2D Ultranarrow MoS_2 Inorganic Nanoribbons Encapsulated in Quasi-1D Carbon Nanotubes," *Journal of the American Chemical Society*, vol. 132, no. 39, pp. 13 840–13 847, 2010. DOI: 10.1021/ja1058026.

[87] H. Liu, J. Gu, and P. D. Ye, "MoS_2 nanoribbon transistors: Transition from depletion mode to enhancement mode by channel-width trimming," *IEEE Electron Device Letters*, vol. 33, no. 9, pp. 1273–1275, 2012. DOI: 10.1109/led.2012.2202630.

[88] M. V. Bollinger, J. V. Lauritsen, K. W. Jacobsen, J. K. Nørskov, S. Helveg, and F. Besenbacher, "One-Dimensional Metallic Edge States in MoS_2," *Physical Review Letters*, vol. 87, no. 19, p. 196 803, 2001. DOI: 10.1103/physrevlett.87.196803.

[89] S. Pavlović and F. M. Peeters, "Electronic properties of triangular and hexagonal MoS_2 quantum dots," *Physical Review B*, vol. 91, no. 15, p. 155 410, 2015. DOI: 10.1103/physrevb.91.155410.

[90] H. Rostami, R. Asgari, and F. Guinea, "Edge modes in zigzag and armchair ribbons of monolayer MoS_2," *Journal of Physics: Condensed Matter*, vol. 28, no. 49, p. 495 001, 2016. DOI: 10.1088/0953-8984/28/49/495001.

[91] S. Helveg, J. V. Lauritsen, E. Lægsgaard, I. Stensgaard, J. K. Nørskov, B. S. Clausen, H. Topsøe, and F. Besenbacher, "Atomic-Scale Structure of Single-Layer MoS2 Nanoclusters," *Physical Review Letters*, vol. 84, pp. 951–954, 2000. DOI: 10.1103/PhysRevLett.84.951.

[92] D. Wu, X. Li, L. Luan, X. Wu, W. Li, M. N. Yogeesh, R. Ghosh, Z. Chu, D. Akinwande, Q. Niu, and K. Lai, "Uncovering edge states and electrical inhomogeneity in MoS_2 field-effect transistors," *Proceedings of the National Academy of Sciences*, vol. 113, no. 31, pp. 8583–8588, 2016. DOI: 10.1073/pnas.1605982113.

[93] A. Cresti and S. Roche, "Edge-disorder-dependent transport length scales in graphene nanoribbons: From Klein defects to the superlattice limit," *Physical Review B*, vol. 79, no. 23, p. 233 404, 2009. DOI: 10.1103/physrevb.79.233404.

[94] S. Bertolazzi, P. Bondavalli, S. Roche, T. San, S.-Y. Choi, L. Colombo, F. Bonaccorso, and P. Samorì, "Nonvolatile memories based on graphene and related 2d materials," *Advanced Materials*, vol. 31, no. 10, p. 1 806 663, 2019. DOI: 10.1002/adma.201806663.

[95] A. Pospischil and T. Mueller, "Optoelectronic devices based on atomically thin transition metal dichalcogenides," *Applied Sciences*, vol. 6, no. 3, p. 78, 2016. DOI: 10.3390/app6030078.

[96] T. Mueller and E. Malic, "Exciton physics and device application of two-dimensional transition metal dichalcogenide semiconductors," *npj 2D Materials and Applications*, vol. 2, no. 1, p. 29, 2018. DOI: 10.1038/s41699-018-0074-2.

[97] A. Avsar, H. Ochoa, F. Guinea, B. Özyilmaz, B. J. van Wees, and I. J. Vera-Marun, "Colloquium: Spintronics in graphene and other two-dimensional materials," *arXiv:1909.09188v2*, 2019.

[98] J. R. Schaibley, H. Yu, G. Clark, P. Rivera, J. S. Ross, K. L. Seyler, W. Yao, and X. Xu, "Valleytronics in 2d materials," *Nature Reviews Materials*, vol. 1, no. 11, p. 16 055, 2016. DOI: 10.1038/natrevmats.2016.55.

[99] R. Ponnusamy and C. S. Rout, "Transition metal dichalcogenides in sensors," in *Two Dimensional Transition Metal Dichalcogenides*, Springer Singapore, 2019, pp. 293–329. DOI: 10.1007/978-981-13-9045-6_9.

[100] V. Podzorov, M. E. Gershenson, C. Kloc, R. Zeis, and E. Bucher, "High-mobility field-effect transistors based on transition metal dichalcogenides," *Applied Physics Letters*, vol. 84, no. 17, pp. 3301–3303, 2004. DOI: 10.1063/1.1723695.

[101] H. Fang, S. Chuang, T. C. Chang, K. Takei, T. Takahashi, and A. Javey, "High-performance single layered WSe_2 p-FETs with chemically doped contacts," *Nano Letters*, vol. 12, no. 7, pp. 3788–3792, 2012. DOI: 10.1021/nl301702r.

[102] G.-H. Lee, Y.-J. Yu, X. Cui, N. Petrone, C.-H. Lee, M. S. Choi, D.-Y. Lee, C. Lee, W. J. Yoo, K. Watanabe, T. Taniguchi, C. Nuckolls, P. Kim, and J. Hone, "Flexible and transparent MoS_2 field-effect transistors on hexagonal boron nitride-graphene heterostructures," *ACS Nano*, vol. 7, no. 9, pp. 7931–7936, 2013. DOI: 10.1021/nn402954e.

[103] D. Sarkar, X. Xie, W. Liu, W. Cao, J. Kang, Y. Gong, S. Kraemer, P. M. Ajayan, and K. Banerjee, "A subthermionic tunnel field-effect transistor with an atomically thin channel," *Nature*, vol. 526, no. 7571, pp. 91–95, 2015. DOI: 10.1038/nature15387.

[104] D. Logoteta, M. G. Pala, J. Choukroun, P. Dollfus, and G. Iannaccone, "A Steep-Slope MoS_2-Nanoribbon MOSFET Based on an Intrinsic Cold-Contact Effect," *IEEE Electron Device Letters*, vol. 40, no. 9, pp. 1550–1553, 2019. DOI: 10.1109/led.2019.2928131.

[105] T. Georgiou, R. Jalil, B. D. Belle, L. Britnell, R. V. Gorbachev, S. V. Morozov, Y.-J. Kim, A. Gholinia, S. J. Haigh, O. Makarovsky, L. Eaves, L. A. Ponomarenko, A. K. Geim, K. S. Novoselov, and A. Mishchenko, "Vertical field-effect transistor based on graphene–WS_2 heterostructures for flexible and transparent electronics," *Nature Nanotechnology*, vol. 8, no. 2, pp. 100–103, 2012. DOI: 10.1038/nnano.2012.224.

[106] T. Roy, M. Tosun, M. Hettick, G. H. Ahn, C. Hu, and A. Javey, "2D-2D tunneling field-effect transistors using $WSe_2/SnSe_2$ heterostructures," *Applied Physics Letters*, vol. 108, no. 8, p. 083 111, 2016. DOI: 10.1063/1.4942647.

[107] S. Bertolazzi, D. Krasnozhon, and A. Kis, "Nonvolatile memory cells based on MoS_2/graphene heterostructures," *ACS Nano*, vol. 7, no. 4, pp. 3246–3252, 2013. DOI: 10.1021/nn3059136.

[108] G. H. Shin, C.-K. Kim, G. S. Bang, J. Y. Kim, B. C. Jang, B. J. Koo, M. H. Woo, Y.-K. Choi, and S.-Y. Choi, "Multilevel resistive switching nonvolatile memory based on MoS 2 nanosheet-embedded graphene oxide," *2D Materials*, vol. 3, no. 3, p. 034 002, 2016. DOI: 10.1088/2053-1583/3/3/034002.

[109] K.-A. N. Duerloo, Y. Li, and E. J. Reed, "Structural phase transitions in two-dimensional mo- and w-dichalcogenide monolayers," *Nature Communications*, vol. 5, no. 1, p. 4214, 2014. DOI: 10.1038/ncomms5214.

[110] D. Rhodes, D. A. Chenet, B. E. Janicek, C. Nyby, Y. Lin, W. Jin, D. Edelberg, E. Mannebach, N. Finney, A. Antony, T. Schiros, T. Klarr, A. Mazzoni, M. Chin, Y.-c. Chiu, W. Zheng, Q. R. Zhang, F. Ernst, J. I. Dadap, X. Tong, J. Ma, R. Lou, S. Wang, T. Qian, H. Ding, R. M. Osgood, D. W. Paley, A. M. Lindenberg, P. Y. Huang, A. N. Pasupathy, M. Dubey, J. Hone, and L. Balicas, "Engineering the structural and electronic phases of $MoTe_2$ through w substitution," *Nano Letters*, vol. 17, no. 3, pp. 1616–1622, 2017. DOI: 10.1021/acs.nanolett.6b04814.

[111] Q. A. Vu, Y. S. Shin, Y. R. Kim, V. L. Nguyen, W. T. Kang, H. Kim, D. H. Luong, I. M. Lee, K. Lee, D.-S. Ko, J. Heo, S. Park, Y. H. Lee, and W. J. Yu, "Two-terminal floating-gate memory with van der waals heterostructures for ultrahigh on/off ratio," *Nature Communications*, vol. 7, no. 1, p. 12 725, 2016. DOI: 10.1038/ncomms12725.

[112] O. Lopez-Sanchez, D. Lembke, M. Kayci, A. Radenovic, and A. Kis, "Ultrasensitive photodetectors based on monolayer MoS_2," *Nature Nanotechnology*, vol. 8, no. 7, pp. 497–501, 2013. DOI: 10.1038/nnano.2013.100.

[113] H. S. Lee, S.-W. Min, Y.-G. Chang, M. K. Park, T. Nam, H. Kim, J. H. Kim, S. Ryu, and S. Im, "MoS_2 nanosheet phototransistors with thickness-modulated optical energy gap," *Nano Letters*, vol. 12, no. 7, pp. 3695–3700, 2012. DOI: 10.1021/nl301485q.

[114] A. Abderrahmane, P. J. Ko, T. V. Thu, S. Ishizawa, T. Takamura, and A. Sandhu, "High photosensitivity few-layered $MoSe_2$ back-gated field-effect phototransistors," *Nanotechnology*, vol. 25, no. 36, p. 365 202, 2014. DOI: 10.1088/0957-4484/25/36/365202.

[115] N. Huo, S. Yang, Z. Wei, S.-S. Li, J.-B. Xia, and J. Li, "Photoresponsive and gas sensing field-effect transistors based on multilayer WS_2 nanoflakes," *Scientific Reports*, vol. 4, no. 1, p. 5209, 2014. DOI: 10.1038/srep05209.

[116] W. Zhang, M.-H. Chiu, C.-H. Chen, W. Chen, L.-J. Li, and A. T. S. Wee, "Role of metal contacts in high-performance phototransistors based on WSe_2 monolayers," *ACS Nano*, vol. 8, no. 8, pp. 8653–8661, 2014. DOI: 10.1021/nn503521c.

[117] L. Britnell, R. M. Ribeiro, A. Eckmann, R. Jalil, B. D. Belle, A. Mishchenko, Y.-. J. Kim, R. V. Gorbachev, T. Georgiou, S. V. Morozov, A. N. Grigorenko, A. K. Geim, C. Casiraghi, A. H. C. Neto, and K. S. Novoselov, "Strong light-matter interactions in heterostructures of atomically thin films," *Science*, vol. 340, no. 6138, pp. 1311–1314, 2013. DOI: 10.1126/science.1235547.

[118] W. J. Yu, Q. A. Vu, H. Oh, H. G. Nam, H. Zhou, S. Cha, J.-Y. Kim, A. Carvalho, M. Jeong, H. Choi, A. H. C. Neto, Y. H. Lee, and X. Duan, "Unusually efficient photocurrent extraction in monolayer van der waals heterostructure by tunnelling through discretized barriers," *Nature Communications*, vol. 7, no. 1, p. 13 278, 2016. DOI: 10.1038/ncomms13278.

[119] C.-H. Lee, G.-H. Lee, A. M. van der Zande, W. Chen, Y. Li, M. Han, X. Cui, G. Arefe, C. Nuckolls, T. F. Heinz, J. Guo, J. Hone, and P. Kim, "Atomically thin p–n junctions with van der waals heterointerfaces," *Nature Nanotechnology*, vol. 9, no. 9, pp. 676–681, 2014. DOI: 10.1038/nnano.2014.150.

[120] F. Withers, O. D. Pozo-Zamudio, A. Mishchenko, A. P. Rooney, A. Gholinia, K. Watanabe, T. Taniguchi, S. J. Haigh, A. K. Geim, A. I. Tartakovskii, and K. S. Novoselov, "Light-emitting diodes by band-structure engineering in van der waals heterostructures," *Nature Materials*, vol. 14, no. 3, pp. 301–306, 2015. DOI: 10.1038/nmat4205.

[121] A. Pospischil, M. M. Furchi, and T. Mueller, "Solar-energy conversion and light emission in an atomic monolayer p–n diode," *Nature Nanotechnology*, vol. 9, no. 4, pp. 257–261, 2014. DOI: 10.1038/nnano.2014.14.

[122] X. Duan, C. Wang, A. Pan, R. Yu, and X. Duan, "Two-dimensional transition metal dichalcogenides as atomically thin semiconductors: Opportunities and challenges," *Chemical Society Reviews*, vol. 44, no. 24, pp. 8859–8876, 2015. DOI: 10.1039/c5cs00507h.

[123] S. Kang, D. Lee, J. Kim, A. Capasso, H. S. Kang, J.-W. Park, C.-H. Lee, and G.-H. Lee, "2d semiconducting materials for electronic and optoelectronic applications: Potential and challenge," *2D Materials*, vol. 7, no. 2, p. 022 003, 2020. DOI: 10.1088/2053-1583/ab6267.

[124] Y. Guo, Y. Han, J. Li, A. Xiang, X. Wei, S. Gao, and Q. Chen, "Study on the resistance distribution at the contact between molybdenum disulfide and metals," *ACS Nano*, vol. 8, no. 8, pp. 7771–7779, 2014. DOI: 10.1021/nn503152r.

[125] A. Allain, J. Kang, K. Banerjee, and A. Kis, "Electrical contacts to two-dimensional semiconductors," *Nature Materials*, vol. 14, no. 12, pp. 1195–1205, 2015. DOI: 10.1038/nmat4452.

[126] J. Xue, J. Sanchez-Yamagishi, D. Bulmash, P. Jacquod, A. Deshpande, K. Watanabe, T. Taniguchi, P. Jarillo-Herrero, and B. J. LeRoy, "Scanning tunnelling microscopy and spectroscopy of ultra-flat graphene on hexagonal boron nitride," *Nature Materials*, vol. 10, no. 4, pp. 282–285, 2011. DOI: 10.1038/nmat2968.

[127] A. Kormányos, G. Burkard, M. Gmitra, J. Fabian, V. Zólyomi, N. D. Drummond, and V. Fal'ko, "Corrigendum : K.p theory for two-dimensional transition metal dichalcogenide semiconductors," *2D Materials*, vol. 2, no. 4, p. 049 501, 2015. DOI: 10.1088/2053-1583/2/4/049501.

[128] F. Wu, F. Qu, and A. H. MacDonald, "Exciton band structure of monolayer MoS_2," *Physical Review B*, vol. 91, no. 7, p. 075 310, 2015. DOI: 10.1103/physrevb.91.075310.

[129] G.-B. Liu, W.-Y. Shan, Y. Yao, W. Yao, and D. Xiao, "Three-band tight-binding model for monolayers of group-VIB transition metal dichalcogenides," *Physical Review B*, vol. 89, no. 3, p. 039 901, 2014. DOI: 10.1103/physrevb.88.085433.

[130] S. Fang, R. K. Defo, S. N. Shirodkar, S. Lieu, G. A. Tritsaris, and E. Kaxiras, "Ab initiotight-binding hamiltonian for transition metal dichalcogenides," *Physical Review B*, vol. 92, no. 20, p. 205 108, 2015. DOI: 10.1103/physrevb.92.205108.

[131] R. Roldán, M. P. López-Sancho, F. Guinea, E. Cappelluti, J. A. Silva-Guillén, and P. Ordejón, "Momentum dependence of spin–orbit interaction effects in single-layer and multi-layer transition metal dichalcogenides," *2D Materials*, vol. 1, no. 3, p. 034 003, 2014. DOI: 10.1088/2053-1583/1/3/034003.

[132] E. Cappelluti, R. Roldán, J. A. Silva-Guillén, P. Ordejón, and F. Guinea, "Tight-binding model and direct-gap/indirect-gap transition in single-layer and multilayer MoS_2," *Physical Review B*, vol. 88, no. 7, p. 075 409, 2013. DOI: 10.1103/physrevb.88.075409.

[133] H. Rostami, R. Roldán, E. Cappelluti, R. Asgari, and F. Guinea, "Theory of Strain in Single-Layer Transition Metal Dichalcogenides," *Physical Review B*, vol. 92, no. 19, p. 195 402, 2015. DOI: 10.1103/PhysRevB.92.195402.

[134] F. Bloch, "Uber die quantenmechanik der elektronen in kristallgittern," *Zeitschrift fur Physik*, vol. 52, no. 7-8, pp. 555–600, 1929. DOI: 10.1007/bf01339455.

[135] J. C. Slater and G. F. Koster, "Simplified LCAO method for the periodic potential problem," *Physical Review*, vol. 94, no. 6, pp. 1498–1524, 1954. DOI: 10.1103/physrev.94.1498.

[136] D. A. Papaconstantopoulos and M. J. Mehl, "The Slater-Koster tight-binding method: A computationally efficient and accurate approach," *Journal of Physics: Condensed Matter*, vol. 15, no. 10, R413–R440, 2003. DOI: 10.1088/0953-8984/15/10/201.

[137] A. C. Dias, F. Qu, D. L. Azevedo, and J. Fu, "Band structure of monolayer transition-metal dichalcogenides and topological properties of their nanoribbons: Next-nearest-neighbor hopping," *Physical Review B*, vol. 98, no. 7, p. 075 202, 2018. DOI: 10.1103/physrevb.98.075202.

[138] E. Ridolfi, L. R. F. Lima, E. R. Mucciolo, and C. H. Lewenkopf, "Electronic transport in disordered MoS_2 nanoribbons," *Physical Review B*, vol. 95, no. 3, p. 035 430, 2017. DOI: 10.1103/physrevb.95.035430.

[139] K. Kośmider, J. W. González, and J. Fernández-Rossier, "Large spin splitting in the conduction band of transition metal dichalcogenide monolayers," *Physical Review B*, vol. 88, no. 24, p. 245 436, 2013. DOI: 10.1103/physrevb.88.245436.

[140] D. J. Griffiths and D. F. Schroeter, *Introduction to Quantum Mechanics*. Cambridge University Press, 2018. DOI: 10.1017/9781316995433.

[141] J. A. Miwa, S. Ulstrup, S. G. Sørensen, M. Dendzik, A. G. Čabo, M. Bianchi, J. V. Lauritsen, and P. Hofmann, "Electronic structure of epitaxial single-layer MoS_2," *Physical Review Letters*, vol. 114, no. 4, p. 046 802, 2015. DOI: 10.1103/physrevlett.114.046802.

[142] H. Wang, C. Zhang, W. Chan, C. Manolatou, S. Tiwari, and F. Rana, "Radiative lifetimes of excitons and trions in monolayers of the metal dichalcogenideMoS_2," *Physical Review B*, vol. 93, no. 4, p. 045 407, 2016. DOI: 10.1103/physrevb.93.045407.

[143] D. Mastrogiuseppe, N. Sandler, and S. E. Ulloa, "RKKY interaction and intervalley processes inp-doped transition-metal dichalcogenides," *Physical Review B*, vol. 90, no. 16, p. 161 403, 2014. DOI: 10.1103/physrevb.90.161403.

[144] H. Hatami, T. Kernreiter, and U. Zülicke, "Spin susceptibility of two-dimensional transition-metal dichalcogenides," *Physical Review B*, vol. 90, no. 4, p. 045 412, 2014. DOI: 10.1103/physrevb.90.045412.

[145] D. Xiao, G.-B. Liu, W. Feng, X. Xu, and W. Yao, "Coupled Spin and Valley Physics in Monolayers of MoS_2 and Other Group-VI Dichalcogenides," *Physical Review Letters*, vol. 108, no. 19, p. 196 802, 2012. DOI: 10.1103/physrevlett.108.196802.

[146] A. Kormányos, V. Zólyomi, N. D. Drummond, P. Rakyta, G. Burkard, and V. I. Fal'Ko, "Monolayer mos2: Trigonal warping, the Γ valley, and spin-orbit coupling effects," *Physical Review B*, vol. 88, no. 4, p. 045 416, 2013. DOI: 10.1103/PhysRevB.88.045416.

[147] A. Arora, M. Koperski, A. Slobodeniuk, K. Nogajewski, R. Schmidt, R. Schneider, M. R. Molas, S. M. de Vasconcellos, R. Bratschitsch, and M. Potemski, "Zeeman spectroscopy of excitons and hybridization of electronic states in few-layer WSe_2, $MoSe_2$ and $MoTe_2$," *2D Materials*, vol. 6, no. 1, p. 015 010, 2018. DOI: 10.1088/2053-1583/aae7e5.

[148] G. Wang, L. Bouet, M. M. Glazov, T. Amand, E. L. Ivchenko, E. Palleau, X. Marie, and B. Urbaszek, "Magneto-optics in transition metal diselenide monolayers," *2D Materials*, vol. 2, no. 3, p. 034 002, 2015. DOI: 10.1088/2053-1583/2/3/034002.

[149] S. Mekonnen and P. Singh, "Dopant introduced valley polarization, spin, and valley hall conductivity in doped monolayer MoS_2," *Advances in Condensed Matter Physics*, vol. 2018, p. 1 303 816, 2018. DOI: 10.1155/2018/1303816.

[150] S. Yuan, R. Roldán, M. I. Katsnelson, and F. Guinea, "Effect of point defects on the optical and transport properties of MoS_2 and WS_2," *Physical Review B*, vol. 90, no. 4, p. 041 402, 2014. DOI: 10.1103/physrevb.90.041402.

[151] J. L. Lado and J. Fernández-Rossier, "Landau levels in 2d materials using wannier hamiltonians obtained by first principles," *2D Materials*, vol. 3, no. 3, p. 035 023, 2016. DOI: 10.1088/2053-1583/3/3/035023.

[152] L. Bawden, S. P. Cooil, F. Mazzola, J. M. Riley, L. J. Collins-McIntyre, V. Sunko, K. W. B. Hunvik, M. Leandersson, C. M. Polley, T. Balasubramanian, T. K. Kim, M. Hoesch, J. W. Wells, G. Balakrishnan, M. S. Bahramy, and P. D. C. King, "Spin–valley locking in the normal state of a transition-metal dichalcogenide superconductor," *Nature Communications*, vol. 7, no. 1, p. 11 711, 2016. DOI: 10.1038/ncomms11711.

[153] G. H. Wannier, "The structure of electronic excitation levels in insulating crystals," *Physical Review*, vol. 52, no. 3, pp. 191–197, 1937. DOI: 10.1103/physrev.52.191.

[154] W. Kohn, "Analytic properties of bloch waves and wannier functions," *Physical Review*, vol. 115, no. 4, pp. 809–821, 1959. DOI: 10.1103/physrev.115.809.

[155] J. D. Cloizeaux, "Orthogonal orbitals and generalized wannier functions," *Physical Review*, vol. 129, no. 2, pp. 554–566, 1963. DOI: 10.1103/physrev.129.554.

[156] A. A. Mostofi, J. R. Yates, Y.-S. Lee, I. Souza, D. Vanderbilt, and N. Marzari, "Wannier90: A tool for obtaining maximally-localised wannier functions," *Computer Physics Communications*, vol. 178, no. 9, pp. 685–699, 2008. DOI: 10.1016/j.cpc.2007.11.016.

[157] N. Marzari, A. A. Mostofi, J. R. Yates, I. Souza, and D. Vanderbilt, "Maximally localized wannier functions: Theory and applications," *Reviews of Modern Physics*, vol. 84, no. 4, pp. 1419–1475, 2012. DOI: 10.1103/revmodphys.84.1419.

[158] A. A. Mostofi, J. R. Yates, G. Pizzi, Y.-S. Lee, I. Souza, D. Vanderbilt, and N. Marzari, "An updated version of wannier90: A tool for obtaining maximally-localised wannier functions," *Computer Physics Communications*, vol. 185, no. 8, pp. 2309–2310, 2014. DOI: 10.1016/j.cpc.2014.05.003.

[159] G. Pizzi, V. Vitale, R. Arita, S. Blügel, F. Freimuth, G. Géranton, M. Gibertini, D. Gresch, C. Johnson, T. Koretsune, J. Ibañez-Azpiroz, H. Lee, J.-M. Lihm, D. Marchand, A. Marrazzo, Y. Mokrousov, J. I. Mustafa, Y. Nohara, Y. Nomura, L. Paulatto, S. Poncé, T. Ponweiser, J. Qiao, F. Thöle, S. S. Tsirkin, M. Wierzbowska, N. Marzari, D. Vanderbilt, I. Souza, A. A. Mostofi, and J. R. Yates, "Wannier90 as a community code: New features and applications," *Journal of Physics: Condensed Matter*, vol. 32, no. 16, p. 165 902, 2020. DOI: 10.1088/1361-648x/ab51ff.

[160] R. D. King-Smith and D. Vanderbilt, "Theory of polarization of crystalline solids," *Physical Review B*, vol. 47, no. 3, pp. 1651–1654, 1993. DOI: 10.1103/physrevb.47.1651.

[161] A. Calzolari, N. Marzari, I. Souza, and M. B. Nardelli, "Ab initiotransport properties of nanostructures from maximally localized wannier functions," *Physical Review B*, vol. 69, no. 3, p. 035 108, 2004. DOI: 10.1103/physrevb.69.035108.

[162] W. Ku, H. Rosner, W. E. Pickett, and R. T. Scalettar, "Insulating ferromagnetism inLa4ba2cu2o10: AnAb InitioWannier function analysis," *Physical Review Letters*, vol. 89, no. 16, p. 167 204, 2002. DOI: 10.1103/physrevlett.89.167204.

[163] D. M. Whittaker and M. P. Croucher, "Maximally localized wannier functions for photonic lattices," *Physical Review B*, vol. 67, no. 8, p. 085 204, 2003. DOI: 10.1103/physrevb.67.085204.

[164] G. D. Mahan, *Many-Particle Physics*. Springer US, 2000. DOI: 10.1007/978-1-4757-5714-9.

[165] G. Stefanucci and R. van Leeuwen, *Nonequilibrium Many-Body Theory of Quantum Systems*. Cambridge University Press, 2009. DOI: 10.1017/cbo9781139023979.

[166] G. S. Canright and S. M. Girvin, "Fractional Statistics: Quantum Possibilities in Two Dimensions," *Science*, vol. 247, no. 4947, pp. 1197–1205, 1990. DOI: 10.1126/science.247.4947.1197.

[167] E. N. Economou, *Green's Functions in Quantum Physics*. Springer Berlin Heidelberg, 2006, ISBN: 3540288384. DOI: 10.1007/3-540-28841-4.

[168] M. Anantram, M. Lundstrom, and D. Nikonov, "Modeling of Nanoscale Devices," *Proceedings of the IEEE*, vol. 96, no. 9, pp. 1511–1550, 2008. DOI: 10.1109/jproc.2008.927355.

[169] H. Haug and A.-P. Jauho, *Quantum Kinetics in Transport and Optics of Semiconductors*. Springer Berlin Heidelberg, 2008. DOI: 10.1007/978-3-540-73564-9.

[170] M. Di Ventra, *Electrical Transport in Nanoscale Systems*. Cambridge University Press, 2008, ISBN: 9780521896344. DOI: 10.1017/cbo9780511755606.

[171] F. Triozon and P. Dollfus, *Simulation of Transport in Nanodevices*. ISTE and John Wiley & Sons, 2016, ISBN: 1848215665. DOI: 10.1002/9781118761793.

[172] A. Cresti, "Theoretical imaging of currents in nanostructures," PhD thesis, Università di Pisa, 2005.

[173] M. Wimmer, "Quantum transport in nanostructures : From computational concepts to spintronics in graphene and magnetic tunnel junctions," PhD thesis, Regensburg, 2009, ISBN: 9783868450255.

[174] M. P. L. Sancho, J. M. L. Sancho, J. M. L. Sancho, and J. Rubio, "Highly convergent schemes for the calculation of bulk and surface Green functions," *Journal of Physics F: Metal Physics*, vol. 15, no. 4, pp. 851–858, 1985. DOI: 10.1088/0305-4608/15/4/009.

[175] L. V. Keldysh, "Diagram technique for nonequilibrium processes," *Journal of Experimental and Theoretical Physics*, vol. 20, no. 4, pp. 1018–1026, 1965.

[176] M. Büttiker, Y. Imry, R. Landauer, and S. Pinhas, "Generalized many-channel conductance formula with application to small rings," *Physical Review B*, vol. 31, no. 10, pp. 6207–6215, 1985. DOI: 10.1103/physrevb.31.6207.

[177] H. van Houten, B. J. van Wees, and C. W. J. Beenakker, "Quantum and classical ballistic transport in constricted two-dimensional electron gases," in *Physics and Technology of Submicron Structures*, Springer Berlin Heidelberg, 1988, pp. 198–207. DOI: 10.1007/978-3-642-83431-8_18.

[178] P. W. Anderson, "Absence of diffusion in certain random lattices," *Physical Review*, vol. 109, no. 5, pp. 1492–1505, 1958. DOI: 10.1103/physrev.109.1492.

[179] R. Avriller, S. Roche, F. Triozon, X. Blase, and S. Latil, "Low-dimensional quantum transport properties of chemically-disordered carbon nanotubes: From weak to strong localization regimes," *Modern Physics Letters B*, vol. 21, no. 29, pp. 1955–1982, 2007. DOI: 10.1142/s0217984907014322.

[180] D. J. Thouless, "Maximum metallic resistance in thin wires," *Physical Review Letters*, vol. 39, no. 18, pp. 1167–1169, 1977. DOI: 10.1103/physrevlett.39.1167.

[181] J.-C. Charlier, X. Blase, and S. Roche, "Electronic and transport properties of nanotubes," *Reviews of Modern Physics*, vol. 79, no. 2, pp. 677–732, 2007. DOI: 10.1103/revmodphys.79.677.

[182] S. M. Goodnick, D. K. Ferry, C. W. Wilmsen, Z. Liliental, D. Fathy, and O. L. Krivanek, "Surface roughness at the Si(100)-SiO_2 interface," *Physical Review B*, vol. 32, no. 12, p. 8171, 1985. DOI: 10.1103/physrevb.32.8171.

[183] B. Biel, L. Donetti, E. R. Ortiz, A. Godoy, and F. Gámiz, "Tunability of effective masses on MoS_2 monolayers," *Microelectronic Engineering*, vol. 147, pp. 302–305, 2015. DOI: 10.1016/j.mee.2015.04.099.

[184] W. Jolie, C. Murray, P. S. Weiß, J. Hall, F. Portner, N. Atodiresei, A. V. Krasheninnikov, C. Busse, H.-P. Komsa, A. Rosch, and T. Michely, "Tomonaga-Luttinger Liquid in a Box: Electrons Confined within MoS_2 Mirror-Twin Boundaries," *Physical Review X*, vol. 9, no. 1, p. 011 055, 2019. DOI: 10.1103/physrevx.9.011055.

[185] S.-F. Chen and Y.-R. Wu, "Electronic properties of MoS_2 nanoribbon with strain using tight-binding method," *Physica Status Solidi (b)*, vol. 254, no. 2, p. 1 600 565, 2017. DOI: 10.1002/pssb.201600565.

[186] G. Kresse and J. Furthmüller, "Efficient iterative schemes forab initiototal-energy calculations using a plane-wave basis set," *Physical Review B*, vol. 54, no. 16, pp. 11 169–11 186, 1996. DOI: 10.1103/physrevb.54.11169.

[187] J. P. Perdew, K. Burke, and M. Ernzerhof, "Generalized Gradient Approximation Made Simple," *Physical Review Letters*, vol. 77, no. 18, pp. 3865–3868, 1996. DOI: 10.1103/physrevlett.77.3865.

[188] H. Qiu, T. Xu, Z. Wang, W. Ren, H. Nan, Z. Ni, Q. Chen, S. Yuan, F. Miao, F. Song, G. Long, Y. Shi, L. Sun, J. Wang, and X. Wang, "Hopping transport through defect-induced localized states in molybdenum disulphide," *Nature Communications*, vol. 4, p. 2642, 2013. DOI: 10.1038/ncomms3642.

[189] S. Adam, S. Jung, N. N. Klimov, N. B. Zhitenev, J. A. Stroscio, and M. D. Stiles, "Mechanism for puddle formation in graphene," *Physical Review B*, vol. 84, no. 23, p. 235 421, 2011. DOI: 10.1103/physrevb.84.235421.

[190] D. V. Tuan, F. Ortmann, A. W. Cummings, D. Soriano, and S. Roche, "Spin dynamics and relaxation in graphene dictated by electron-hole puddles," *Scientific Reports*, vol. 6, p. 21 046, 2016. DOI: 10.1038/srep21046.

List of publications and conferences

Publications

1. **J. Park**, M. Mouis, F. Trizon, K. Xue and A. Cresti, "Electron transport properties of mirror twin grain boundaries in molybdenum disulfide: Impact of disorder", *Physical Review B*, **100** (23), 235403, 2019.

2. J. Cao, **J. Park**, F. Triozon, M. G. Pala and A. Cresti, "Simulation of 2D material-based tunnel field-effect transistors: planar vs. vertical architectures", *Nanoelectronic Devices - Tunnel FETs*, **1**, 2018.

3. **J. Park**, M. Mouis, F. Triozon and A. Cresti, "Impact of edge roughness on the electron transport properties of MoS_2 ribbons", *Journal of Applied Physics*, **124** (22), 224302, 2018.

International conferences

1. **J. Park**, M. Mouis, F. Triozon, K. Xue, and A. Cresti, "Grain boundaries in transition metal dichalcogenides : electron transport properties", Graphene & Co GDR-i 2019 Annual Meeting, Germany (2019), oral.

2. **J. Park**, M. Mouis, F. Triozon, K. Xue, and A. Cresti, "Electron transport along and through MoS_2 grain boundaries", Graphene 2019, Italy (2019), oral.

3. **J. Park**, M. Mouis, F. Triozon and A. Cresti, "Simulation of electron transport in rough MoS_2 ribbons", Graphene & Co GDR-i 2018 Annual Meeting, France (2018), oral.

Acknowledgements

Over the past three and a half years, it was a great pleasure to work at IMEP-LaHC and CEA-Leti under the supervision of the thesis director Dr. Mireille Mouis, and the two co-supervisors Dr. Alessandro Cresti and Dr. François Triozon. First of all, I'd like to thank Mireille for her guidance toward better direction on the thesis and her sincere and warm advices to come up to this moment. And I will be forever grateful to Alessandro who has welcomed me at any time for discussions, and even for some trivial questions. I appreciate him for bringing inspirations during the entire period of my PhD and helping me to move forward both professionally and personally. Also, I'd like to thank François, who gave me novel ideas and honest advices for better research. The experiences I have had with my supervisors was one of the most valuable gifts in my life, and I'm sure that it will give me great strength in my future career as a researcher.

Besides my supervisors, I would like to thank Prof. Kanhao Xue for providing DFT calculations, which lead to the in-depth interpretation on my research. Also, I would like to address my deepest gratitude to Dr. Francis Balestra and Dr. Pascal Pochet, who attended all the CSI meetings. Their in-depth questions on my research and practical advices were very helpful for me to plan for the next step.

I'm also grateful to my colleagues, Dr. Corentin Grillet and Dr. Jiang Cao, whom I spent precious time with at the beginning of my Ph.D. They gave me the helping hand and shared me brilliant ideas of the thesis work. Likewise, I appreciate all the members of IMEP-LaHC and CEA-Leti for offering me their energy, knowledge, and big smiles.

Lastly, words cannot express my gratitude I feel to my family who has supported and encouraged me all the time. I'd like to say thank you to Dagyo for wonderful and unforgettable days in Grenoble, for standing by my side to cheer me on during my darkest hour.